Dynamik von Stufen auf Au (1 1 *n*) Elektroden in elektrochemischer Umgebung

Inaugural – Dissertation

zur
Erlangung des Doktorgrades der
Mathematisch – Naturwissenschaftlichen Fakultät
der Heinrich – Heine – Universität Düsseldorf

vorlegt von

Mohammad Al-Shakran

aus Al-Ramtha (JORDANIEN)

Jülich,Februar 2011

Dynamics of Steps on Au(1 1 *n*) Electrodes in Electrochemical Environment

A dissertation in Candidacy for a Doctoral Degree in Natural Sciences
submitted to the Faculty of Mathematics and Natural Sciences of the Heinrich – Heine – University Düsseldorf

By

M.Sc. of Physics

Mohammad Al-Shakran

From Al-Ramtha, Jordan

Jülich,February 2011

Abstract

This thesis deals with the study of the dynamics of surface defects on stepped Au(100) surface in electrochemical environment using electrochemical scanning tunneling microscope. The first aim of this thesis is to study the evolution of step bunches with time as a function of electrode potential. In previous studies, the evolution of step bunches with time has been performed for surfaces under vacuum conditions, however it was rarely studied in electrochemistry. The aim of this thesis is to fill this gap. The focus lies on the analysis of vicinal Au(1 1 *n*) electrodes, *n*=7, 9, 11, 17, in halide containing electrolyte. It is shown that Au(1 1 *n*) surfaces are unstable against step bunching. The surfaces arrange into alternating stripes of reconstructed areas (almost free of steps) and steep, unreconstructed step bunches. Although the step bunches are stable in time, individual steps within the bunch are yet very mobile, indicating that the step bunches formed after flame annealing are in equilibrium even at high electrode potentials. The step-step distance distribution shows that Au(1 1 *n*) reveals a wide distribution of local orientations.

The reconstruction periodicity on stepped Au(1 1 *n*) surfaces has been studied, and it is found that the reconstruction on these surfaces differs from that on flat Au(100) leading to a complex peaks structure in cyclic voltammograms indicative of different types of reconstruction unit cells established on these surfaces.

Furthermore, equilibrium fluctuations of monatomic high steps on Au(1 1 17) and Au(1 1 29) in chloride and bromide containing electrolyte were studied. The correlation function obeys a power law in time with exponent 1/2 at low potentials and- surprisingly- with an exponent close to 3/4 at high potentials. Further, the time correlation function depends on the step-step distance with an exponent close to 3/2 at high potentials not explained by theory yet.

By analyzing the spatial correlation function for both surfaces the kink energies as well as the diffusivities can be estimated. A linear relation between the kink energy ε and the electrode potential is found. Since the formation of a kink is associated with a dipole moment, the kink

dipole moment μ was determined for the first time from the linear relation between the kink energy ε and the electric charge density σ.

Kurzfassung

Diese Arbeit beschreibt die Untersuchung der Dynamik von Defekten auf gestuften Au(100)-Flächen im Elektrolyten mittels elektrochemischer Rastertunnelmikroskopie. Defekte auf Oberflächen wie Stufen oder Nanostrukturen haben z.B. große Bedeutung für katalytische Reaktionen oder Korrosionsprozesse. In dieser Arbeit werden zunächst Defekte betrachtet, die sich aus vielen Einzeldefekten zusammensetzen: Sogenannte Stufenbündel (step bunches), die sich durch Zusammenlegung von monoatomaren Stufen bilden. Untersuchungen an Stufenbündeln wurden bisher nur an Flächen im Vakuum durchgeführt, in elektrolytischer Umgebung aber noch nicht. Ziel dieser Arbeit ist es, diese Lücke zu schließen.

Der Schwerpunkt der Arbeit liegt in den Untersuchung von vizinalen Au(1 1 *n*)-Flächen, mit *n*=7, 9, 11, 17, in halogenid-haltigen Elektrolyten. (1 1 *n*)-Flächen von fcc Materialien besitzen im geometrisch idealen Fall parallele Stufen mit einem definierten mittleren Abstand. Au(1 1 *n*)-Flächen sind jedoch instabil und es bilden sich Stufenbündel. Die Oberflächen bestehen daher einerseits aus nahezu stufenfreien Flächen und andererseits aus steilen Stufenbündeln. In dieser Arbeit werden zuerst Studien zur zeitlichen Entwicklung von Stufenbündeln in Abhängigkeit vom Elektrodenpotential präsentiert: Die Oberflächenstruktur ist stabil, einzelne Stufen innerhalb der Bündel sind jedoch beweglich. Dies deutet darauf hin, dass die Stufenbündel nach dem Tempern auch bei hohen Elektrodenpotentialen im Gleichgewicht sind. Die Analyse der Stufenabstandsverteilung zeigt, dass die Stufenbündel eine breite Verteilung von lokalen Orientierungen besitzen.

Von der glatten Au(100)-Fläche ist bekannt, dass die Oberfläche nach dem Tempern auch in Elektrolyten bei bestimmten Potentialen rekonstruiert. In dieser Arbeit wurde untersucht, wie sich die Bildung der Stufenbündel auf Au(1 1 *n*) auf die Oberflächenrekonstruktion auswirkt. Die Stufenbündel sind unrekonstruiert, während große Terrassen eine Rekonstruktion aufweisen. Es wird gezeigt, dass sich die Rekonstruktion auf den Terrassen von der Rekonstruktion auf glatten Au(100)-Oberflächen unterscheidet, was auch zu einer komplexen Struktur der Voltammogramme von Au (1 1 *n*) führt.

Durch die quantitative Analyse der Fluktuationen von Stufen auf Au (1 1 *n*)–Oberflächen in chlorid- und bromidhaltigen Elektrolyt können die auf der Oberfläche dominierenden Diffusionsprozesse ermittelt werden. Die Auswertung der Zeitkorrelationsfunktion zeigt, dass die Fluktuationen bei niedrigen Potentialen einem Potenzgesetz in der Zeit mit Exponent 1/2 folgen und bei hohen Potentialen einen Zeitexponenten 3/4 besitzen. Ferner hängt die Zeitkorrelationsfunktion vom Stufenabstand ab: Bei hohen Potentialen gehorchen sie einem $L^{3/2}$–Gesetz. Ein Zeitexponent 3/4 bzw. ein $L^{3/2}$-Gesetz wurden in dieser Arbeit erstmalig nachgewiesen.

Durch die Analyse der räumlichen Korrelationsfunktion wurde die Bildungsenergie von Kinken an Stufen bestimmt. Aus dem Vergleich der gefundenen Kinkenenergien bei verschiedenen Potentialen mit der jeweiligen aus Kapazitätsmessungen erhaltenen Oberflächenladung, konnte erstmalig ein Wert für das Dipolmoment von Kinken in halegonid-haltigen Elektrolyten gemessen werden.

Contents

Figures and tables

Chapter 1

Introduction

Many of the characteristic properties of solid matter are related to the boundary of the crystal to the surrounding gas or liquid phase – the crystal surface. Many scientifically interesting and technological important processes depend on surface phenomena. The study of the structure and dynamics of surfaces is hence a basic question in surface science. A variety of experimental techniques have been applied to study the structure and dynamics of surfaces. With the invention of the scanning tunneling microscope (STM), e.g., it is possible to determine the arrangement and the properties of atoms in the first monolayer of a solid in real space. This provides the basis for exciting advances in surface science. Increasing understanding of surface properties led to technological advances in particular in nanostructure fabrication, due to the unique physical and chemical properties of matter introduced by the existence of a surface. For instance, in computer science, the computational efficiency has improved by nearly four orders of magnitudes in 40 years, considering energy consumption per operation as a measure [1,3]. In addition, the size of modern device structures is approaching the nm-scale and the future goal seems to be the application of devices based on molecular and atomic nanostructures [4]. Nanostructure wires with diameters of a few nanometers are very promising and may be used for the next generation of high performance computing devices. Further advances will require the reduction of electronic devices in size to the scale of molecules which requires a further deep understanding of the surface atomic arrangements and decorations, surface stability and atomic processes that can occur on surfaces. With the development of the STM, the direct observation of nanostructures on a large variety of surfaces became possible. This powerful technique not only enables to observe and analyze crystal surfaces, but may also be used to create and manipulate surface nanostructures [1,2]. Not only achievements in experimental techniques but also the creation of designed solid substrates are necessary for future developments in technical applications. Vicinal surfaces, e.g., are very promising candidates for designed nanostructured surfaces. Vicinal surfaces are slightly misoriented with respect to a low index crystal plane (chapter 2). They have attracted a wide interest in many areas, such as

catalysis and epitaxial growth, since the lower coordination of step atoms serve as effective sites for many chemical reactions due to the enhanced bonding energy at these sites [13]. The surface morphology of vicinal surfaces is similar to a staircase of monatomic high steps and they may serve as a template for one-dimensional nanostructures [5]. In the view of technical applications, the stability of nanostructured substrates is of great importance. Therefore, scientists are interested in the stability of vicinal surfaces and related mass transport phenomena [12]. Here, the study of equilibrium fluctuations of single steps on vicinal surfaces offers a powerful method to extract important energy parameters, such as the kink and step energy, and the dominant mass transport on the surface as well as the energy barriers associated with these processes [30].

Recently, scientific interest has also been focused on the study of the metal surfaces in contact with an electrolyte, (i.e. the metal-electrolyte interface). The aim is to understand mass transport processes at the solid-electrolyte interface within the framework of concepts developed for solid surfaces in vacuum [10]. Furthermore, electrochemical methods offer additional possibilities for the generation or modification of nanostructures compared to systems in vacuum. The study of atomic transport processes on metal electrodes helps to understand electroplating, corrosion, electrochemical fabrication of nanomaterials or nanostructured surfaces, as well as catalysis [6].

This thesis is related to the study of the properties and the stability of Au(1 1 *n*) vicinal surfaces in electrolyte. The studies are divided into two main topics: First, the study of step bunching instability phenomena on Au(1 1 *n*) in electrolyte and its dependence on time and electrode potential. Second, studies of equilibrium step fluctuations on Au(1 1 *n*) in electrolyte. Here, the thesis focuses in particular on the influence of specifically adsorbing electrolyte anions on surface mobility.

The thesis is organized as follows: After the introduction, chapter 2 will provide the description of some fundamental concepts which includes the structure of low index surface planes, defects on metal surfaces and vicinal surfaces. Furthermore, some of the required electrochemical concepts involving the electrochemical cell and the electrochemical STM are explained. In addition, a brief theoretical description of the thermodynamics of fluctuating steps is provided. Chapter 2 is followed by a description of the experimental details in chapter 3. In chapter 4 and 5, experimental results are presented. The thesis continues with a discussion of the experimental data on step bunching on Au(1 1 *n*) in electrolyte as well on and the step fluctuation results.

Finally, a brief summary and a future perspective is presented .

Chapter 2

Fundamental Concepts

This chapter presents the fundamental concepts relevant to this work and introduces the corresponding nomenclature.

2.1. The structure of single crystal metal surfaces

2.1.1. Bulk structure of crystals

Atoms are the fundamental building blocks of solid matter, and when they chemically bond to one another they have well-defined equilibrium separations that are determined by the condition of total energy minimization [7]. Bulk atoms may be arranged in a crystalline form, i.e. they have a long-ranged three dimensional periodic arrangement. A fully periodical crystalline structure can be described by means of a unit cell, which is the smallest unit of spatial arrangement of atoms of the crystal. The unit cell is fully determined by three lattice vectors $\vec{a}_x$, $\vec{a}_y$, $\vec{a}_z$ and three angles α, β, γ (figure 2-1, left).

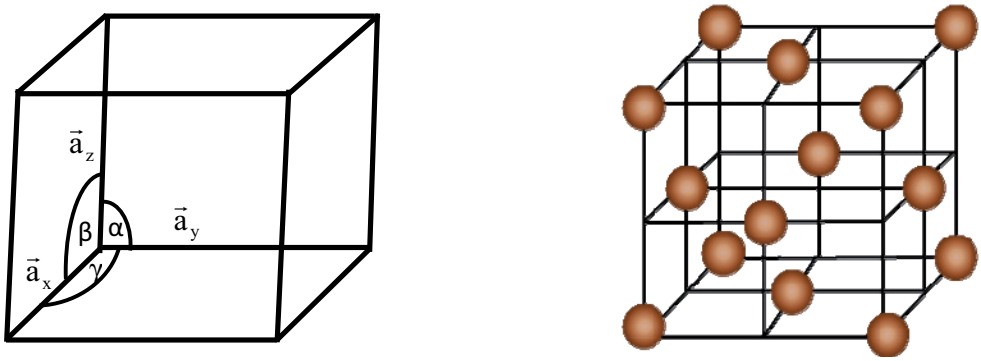

Fig.(2-1): Left: Cubic unit cell with lattice vectors; Right: Non-primitive unit cell of a face-centered cubic (fcc) crystal.(redrawn from [11]).

The entire single crystal can be generated by a simple translation $\vec{T}$ of the unit cell such as:

$$\vec{T} = J\vec{a}_x + H\vec{a}_y + I\vec{a}_z \qquad \text{J, H, I: integers} \qquad (2.1)$$

The element Au which is considered in this work crystallizes in a face-centered cubic structure (fcc)(figure 2.1, right) as many elements such as Ag, Pd, Pt, Ir. In fcc structure, the atoms are densely packed ($\vec{a}_x = \vec{a}_y = \vec{a}_z$, $\alpha = \beta = \gamma = 90°$).

The face of a single crystal structure is described by Miller indices (hkl). The indices h,k,l are the reciprocal mutually prime numbers of the intercepts of the crystal plane with the x-,y- and z-axes. Hence, parallel planes have identical indices. In the three low-index planes (111), (100) and (110) of the fcc structure atoms are arranged in hexagonal, square and rectangular order, respectively. There are of particular importance in the fcc lattice since they pass through the atoms (marked by dark brown color in figure 2-2) and therefore have well defined atomically flat surfaces.

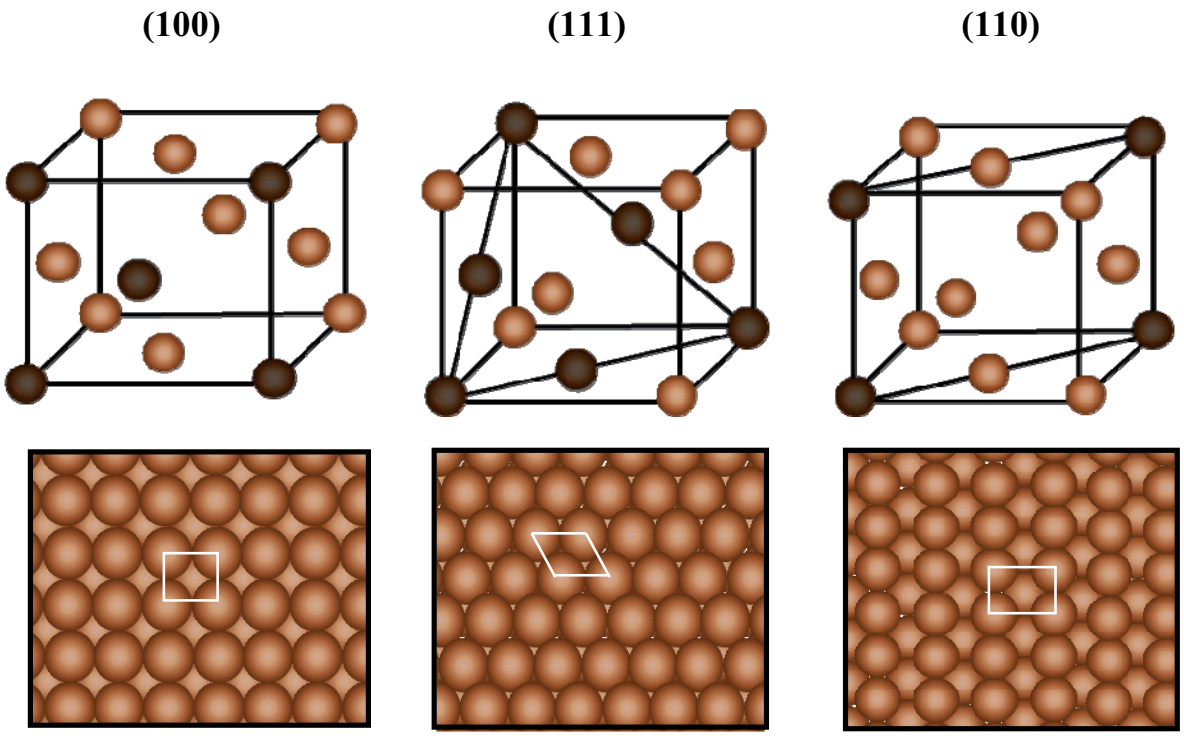

Fig.(2-2): Ball model of the fcc unit cells associated with the section planes of low index (100), (111) and (110) faces (redrawn from [11]). The surface unit cell is marked for each face.

The surface atom density is the highest for (111), followed by the (100) and (110) surfaces [10,11] i.e. (111) is the lowest energy surface.

Surface atoms exhibit imbalance of binding forces at surfaces. Since they do not have the maximum amount of binding partners, surface atoms tend to adopt a particular geometry in order to minimize the total energy of the system [12]. Such a re-arrangement of surface atoms is called surface reconstruction. A particular form of surface reconstruction on the Au(100) surface will be discussed in more detail in chapter 4.

Surfaces with small Miller indices are widely used in electrochemical STM experiments, since the usage of such substrates allows to control surface structures on atomic level [11]. So far ideal low-index surfaces have been discussed. Real crystals have defects in their bulk as well as in their surface structure. Surface defects such as dislocations, steps, kinks and islands play a significant role for the physical and chemical properties of surfaces [14].

2.1.2. Vicinal surfaces

The focus of this thesis lies on one particular defect, surface steps. In particular the thesis deals with vicinal surfaces that reveal an array of parallel steps. Surface steps on vicinal surfaces are generated by inclination of the surface with respect to a low index surface with small angle [10]. Vicinal surfaces are widely used in technical applications due to the regular arrangement of steps on a mesoscopic scale [13]. This work focuses on fcc gold vicinal surfaces, Au(1 1 *n*), which have a small miscut angle (θ) with respect to the low-index orientation (001). Figure (2-3) shows a model of (1 1 *n*) vicinal surfaces. The ideal (1 1 *n*) vicinal consists of a train of regular, equally spaced and parallel steps with (001)-oriented terraces in between. These surfaces have steps of the (111)-type, i.e. the microfacet at the step edge has {111}-orientation. From the scalar product of the surface normal vectors [11*n*] and [001] one obtains the miscut angle θ [14].

$$\tan\theta = \frac{\sqrt{2}}{n} \tag{2.2}$$

The average terrace width is:

$$L = \frac{n}{2} a_{\perp} \tag{2.3}$$

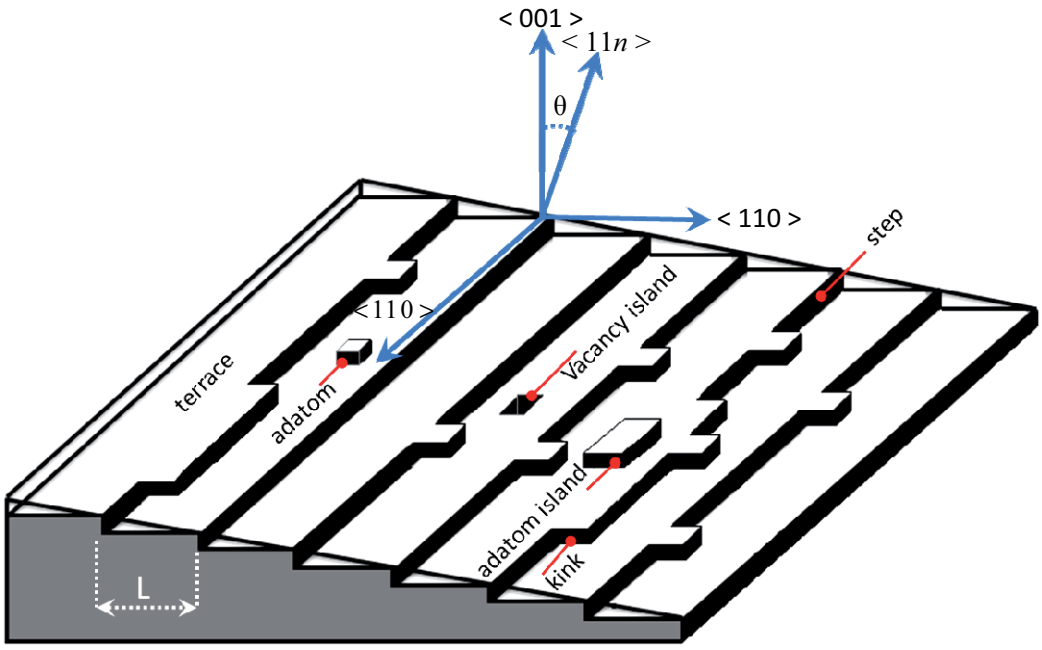

Fig.(2-3): Model of a vicinal surface with respect to the low index (001) plane with monatomic high steps, kinks at steps, adatoms on terraces and at steps, vacancies and islands formed by an ensemble of adatoms.

Here $a_{\perp}$ is the distance between densely packed atomic rows. Besides steps, vicinal surfaces (as any other surface) may have additional defects such as islands, vacancies and vacancy islands (figure (2-3)). Adatom and vacancy islands are thermally generated close to the roughening temperature of a surface [15]. Surface deposition or removal of surface material leads to the creation of adatoms and vacancy islands at low temperatures [14,15]. Figure (2.4) shows an STM image of Au(1 1 29) in electrolyte (the experimental details will be discussed in chapter 4). The steps are of monatomic height, and are separated by (001) terraces. The parallel lines on the terraces indicate that the terraces are reconstructed (see chapter 4).

Defects on metal surfaces carry a positive dipole moment pointing away from the surface. The origin of this positive dipole moment is the charge redistribution at a metal defect. Electron charge is accumulated at the bottom of the defect and reduced at the top of the defect. The charge redistribution is due to the fact that the electrons cannot perfectly follow the sharp structural contour at a defect (figure 2-5) [10].

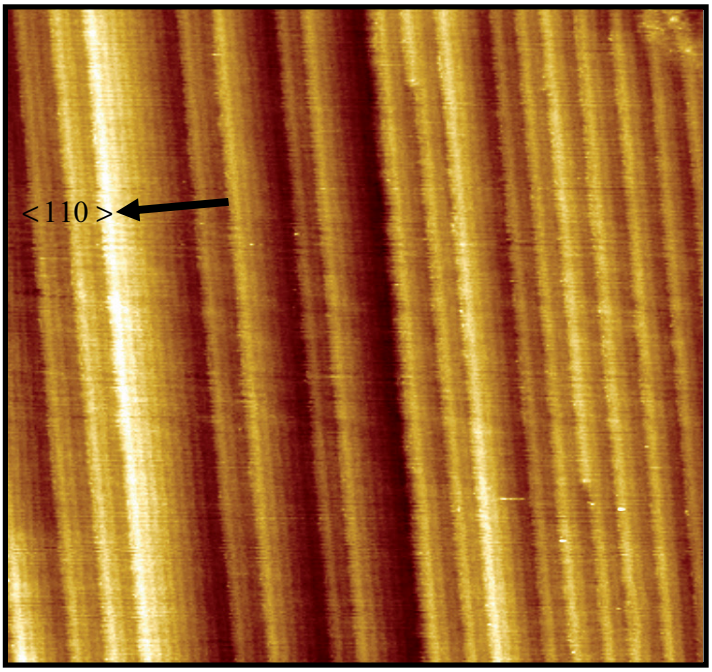

Fig.(2.4): STM image of Au(1 1 29) in 100 mM $HClO_4$ + 1 mM HCl at electrode potential ϕ = -170 mV vs. SCE. Displayed area 110x110 nm^2 (see text for discussion).

The dipole moment associated with a defect reduces the work function of a metal. This reduction is called “Smoluchowski” effect. The dipole moment associated with the surface defect plays an essential role also for energetic step-step interactions on metal surfaces both in vacuum and in electrolyte environment [16]. Energetic interactions may be attractive or repulsive depending on the orientation of the dipole moment.

A second origin of energetic interactions may be elastic interactions, caused by the displacement of step atoms from their lattice positions, leading to an elastic stress field around steps. Elastic interactions are always repulsive.

Repulsive interactions are responsible for the stability of vicinal surfaces against step bunching in ultrahigh vacuum [17,18]. When no explicit energetic interactions exist, steps might interact via entropic interactions. Entropic interactions arise from the condition that crossing of steps is forbidden, since step crossing would lead to overhangs, which costs energy [16].

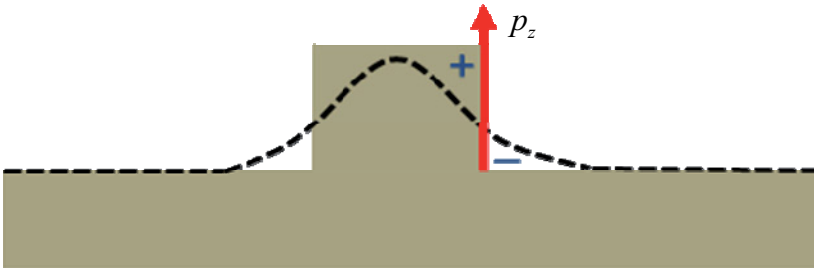

Fig.(2.5): Illustration of the Smoluchowski-effect at a single adatom (or two steps with opposite signs) on a metal surface. The density of electrons (dashed line) cannot follow the sharp structural contour of the surface defect, the result is a positive dipole moment (red arrow) pointing away from the surface.

2.2. Electrochemistry of metal-electrolyte interface

2.2.1. The electrochemical cell

In electrochemistry, the scientific focus lies on structural and dynamical phenomena at the interface between an electronic conductor (the electrode) and an ionic conductor (the electrolyte) [19]. Electrodes may be solid metals such as Pt or Au. The electrolyte is a substance dissociated in the presence of a solvent such as water.

Experimentally, one deals with an electrochemical cell which is a combination of two half-cells; one with a working electrode (WE) at which the reaction takes place, the other with a reference electrode (RE) which is at constant potential. The RE is in equilibrium with the electrolyte, i.e. that no current should flow between electrolyte and RE. The current load on the working electrode is picked up by a third electrode, the counter electrode (CE) [10]. In this configuration, the potential (ϕ) of the WE is controlled with respect to RE, in other words, the energy of the electrons within the working electrode is controlled. In electrochemical measurements, all data is collected with respect to the potential difference between the metal electrode and the reference electrode.

In the potential range between hydrogen evolution and oxidation of the metal electrode, processes like ion desorption or adsorption can occur at the metal-electrolyte interface and may change the structure of the interface. These kinds of processes are called non-faradaic processes, since no charge transfer is associated with these processes across the interface. Then, the electrode is ideally polarized. In the case of an ideally polarized electrode, the metal-electrolyte interface behaves like a capacitor. When a potential is applied across the capacitor, charge (q^M) will accumulate on the metal electrode, which is balanced by a counter charge of equal magnitude and opposite sign in the solution (q^S) such as [19,20]:

$$q^M = - q^S \tag{2.4}$$

The corresponding surface charge density is then given by

$$\sigma = q^M / A \tag{2.5}$$

where A is the electrode area. In the experiments presented in this thesis work, the metal electrodes can be assumed to be ideally polarized, i.e. exclusively non-faradaic processes occur.

2.2.2. Structure of the metal-electrolyte interface

The layer of surface charges at the electrode and its counter part, the layer of oriented water dipoles in the solution is called electric double layer. Figure (2-6) shows a model of the metal-electrolyte interface. The interfacial region can be divided into three parts, the metal electrode (circumscribed by a solid line), a layer of strong metal-electrolyte interactions called Stern layer- or compact, Helmholtz layer (circumscribed by a dashed lines), and the electrolyte. Ions in the electrolyte are surrounded by a solvation shell of polarized solvent molecules (e.g. water molecules), which screen the electric field originating from the ions. The solvated ions carry a net charge, which moves in the electric field of the potential drop across the double layer.

The Stern layer consists of those solvated ions (drawn in red and green colors), ions in a chemisorbed state, called specifically adsorbed ions (drawn in violet color) and water molecules.

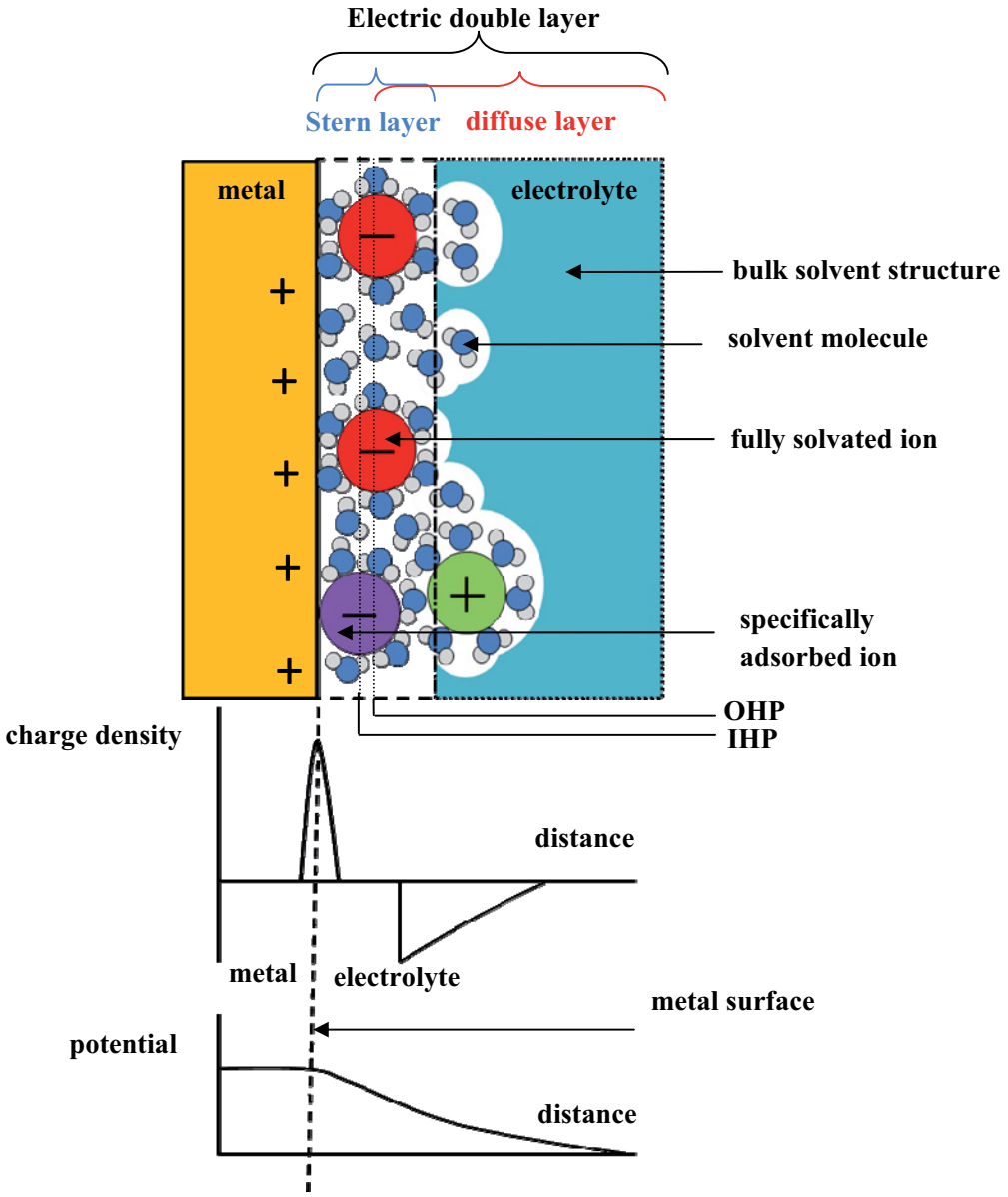

Fig.(2-6): Top: Model of the structure of the metal-electrolyte interface (the electric double layer). Bottom: Schematic illustration of the distribution of charge and potential at the metal-electrolyte interface (see text for discussion). Redrawn from [10,21].

Usually anions are less strongly solvated than cations; therefore their solvation shells are less stable, and they are more often specifically adsorbed, particularly on positively charged metal surfaces. The adsorption of ions at the metal electrode is due to pure electrostatic forces [10,19,20]. The location of the electrical centers of the specifically adsorbed ions is called inner Helmholtz plane (IHP) and the location of centers of the nearest solvated ions is called outer

Helmholtz plane (OHP) (top part of figure (2-6)). The charge distribution and potential for the case in which the metal carries a positive excess charge and the solution a negative one is shown in the bottom part of figure (2-6).

Nonspecifically adsorbed ions are distributed in a three- dimensional region called the diffuse layer, which ranges from the OHP into the bulk of the electrolyte. Stern demonstrated that the electric double layer could be considered as an equivalent of two capacitors connected in series. Their capacitances correspond to the compact layer (inner layer) C_c and the diffuse layer C_d (also called Gouy-Chapman capacitance). The total capacitance is [19]:

$$\frac{1}{C} = \frac{1}{C_c} + \frac{1}{C_d} \tag{2.6}$$

2.2.3. Electrochemical STM

Scanning tunneling microscopy (STM) was originally designed for surface studies in air or in vacuum. Figure (2-7) shows a schematic diagram of the working principle of the STM: A fine metal tip is brought close to a surface by means of piezoelectric actuators which can move the tip independently in x, y, z-direction. The surface has to be an electronic conductor or semi-conductor. When the tip has a small distance from the surface (~ few angstroms), a small number of electrons tunnel between tip and surface. As a consequence a small tunneling current (~ pA-nA) is measured at the tip [48]. The magnitude of the tunneling current depends on the electron density of the states of sample and tip as well as on the gap distance [48,49]. In the constant current mode, the metal tip is scanned across the surface and the tunnel current is kept constant which is controlled by a feed-back loop. The movement of the z-actuator is translated into a gray scale image. Typically, the gray scale information is due to surface topography. However, a strong variation in the density of states of the surface or the tip may lead to dominant gray scale features in the STM images not related to topography [22,103].

The electrochemical version of the scanning tunneling microscopy (EC-STM) became a unique tool for observing electrode surfaces in solution at the atomic and molecular level. The most important difference between the STM operated in air or in vacuum and the electrochemical STM is that in the latter case the metal tip is immersed in an electrolyte and hence, acts as an additional electrode in the electrochemical cell [50].

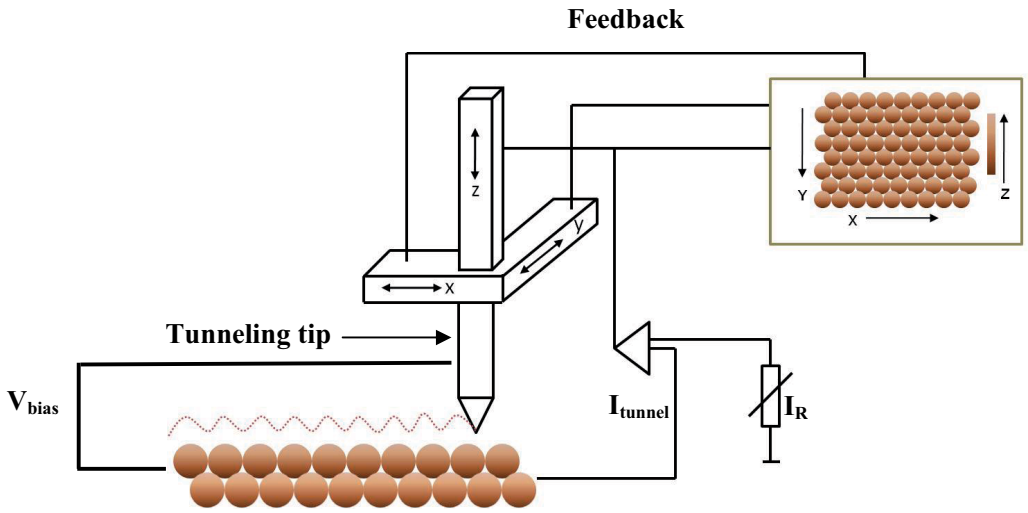

Fig.(2.7): Schematic illustration showing the general working principle of STM.

Electrochemical reactions occur at the tip as well as at the metal electrode. The resulting electrochemical current (faradaic current) is of the order of μA and exceeds the tunneling current by far. Hence, the feedback control becomes impossible. Therefore, precautions have to be taken to reduce the electrochemical current at the tip to a value that can be safely separated from the tunnel current. For this purpose, the tip surface area which is in contact with the electrolyte must be reduced. This can be achieved by covering the tip with isolating material leaving the top most part of the tip uncoated [51] (this technique will be discussed in detail in chapter 3). In addition to a careful coating of the tip, the potential of the tip must be chosen such that no unwanted electrochemical reactions occur at the tip. This requires the use of a bipotentiostat which controls the potential of the working electrode WE and that of the tip simultaneously. Both potentials are measured with respect to a reference electrode RE (i.e., with respect to the potential in the electrolyte) that can be controlled independently. Figure (2-8) shows a schematic diagram of the electric circuit of the four-electrode configuration of an electrochemical STM.

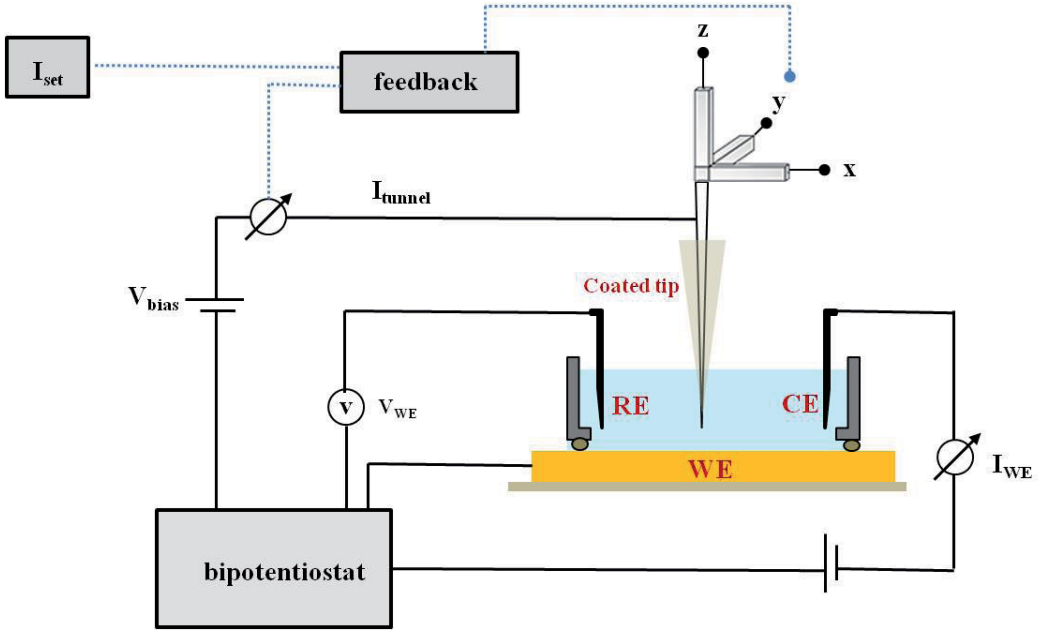

Fig.(2-8): Schematic diagram of the electrochemical STM. The diagram shows the four-electrode configuration: Working electrode (WE), Reference electrode (RE), Counter electrode (CE) and STM (coated) tip.

2.3. Thermodynamics of vicinal surfaces in electrolyte

2.3.1. Surface tension of vicinal surfaces

The surface tension of a surface in contact with an electrolyte can be defined as the work required to create a surface per unit area and it can be written as [29]:

$$\gamma(\phi) = \gamma_{pzc} - \frac{1}{2} C_{pzc} (\phi - \phi_{pzc})^2 + \ldots \qquad (2\text{-}7)$$

Here, C_{pzc} is the interfacial capacitance at the potential of zero charge (pzc). At pzc, no surface charge is accumulated at the metal-electrolyte interface [19]. γ_{pzc} and ϕ_{pzc} are the surface tension and the electrode potential at pzc, respectively. The surface tension of a defect-free surface in contact

with an electrolyte can be expressed as:

$$\gamma = \gamma_{pzc} - \frac{1}{2} C\left(\phi - \phi_{pzc}\right)^2 \tag{2-8}$$

As mentioned in section (2.1.2) defects such as steps carry a dipole moment. For vicinal surfaces in electrolyte, the dipole moment per step atom p_z is proportional to the difference in pzc between the stepped (1 1 *n*) surface and the nominally flat (001) surface without steps [27,28].

$$\phi_{pzc}^{11n} - \phi_{pzc}^{001} = \Delta\phi_{pzc} = -\frac{p_z}{a_{\|}\varepsilon_{\circ}L} \tag{2-9}$$

Where ϕ_{pzc}^{11n} is the pzc of the (1 1 *n*) plane, ϕ_{pzc}^{001} that of the (001) plane, $\varepsilon_{\circ}$ is the absolute permeability and $a_{\|}$ is the nearest-neighbor distance parallel to the step edge. For a stepped surface with inclination angle θ, an additional term $\frac{\beta_{pzc}}{h}\tan\theta$ contributes to equation (2-8). For small angles θ, one obtains [29]:

$$\gamma(\theta,\phi) = \gamma_{pzc} + \frac{\beta_{pzc}}{h}\tan\theta - \frac{1}{2}C(\phi - \phi_{pzc} - \Delta\phi_{pzc})^2 \tag{2-10}$$

where β_{pzc} is the step line tension at pzc, and *h* the step height.

2.3.2. Equilibrium fluctuations of steps

2.3.2.1. Energy of a fluctuating step

In equilibrium, a thermodynamic system fluctuates around the state of minimum (Helmholtz) free energy *F=U-TS*, where *U* is the internal energy of the system, *T* is the temperature and *S* the entropy. At finite temperatures, entropy is increased due to the presence of defects and their motion across the surface. On surfaces, the fluctuations of steps can be viewed as a form of Brownian motion (i.e. random motion of a larger entity due to thermal fluctuations of small sub-unit particles). Step fluctuations are caused by diffusion of atoms and kinks on the surface and mass transport between defects like steps and islands [14,30]. By definition, the net flux of

surface species between two arbitrary points vanishes in equilibrium on the time average since the chemical potential of the surface is constant. Equilibrium step fluctuations are governed by the step line tension β, which is the specific free energy of the step per unit length. For a step with local orientation θ_s, β is related to the step stiffness $\tilde{\beta}$ [10,12,14] via

$$\tilde{\beta} = \left(\beta + \frac{\partial^2 \beta}{\partial \theta_s^2} \right) \tag{2-11}$$

$\tilde{\beta}$ is directly related to the step fluctuation amplitude via the diffusivity b^2:

$$\tilde{\beta} = \frac{k_B T}{b^2} a_{\parallel} \tag{2-12}$$

For low temperatures, respectively large kink formation energies ε, i.e. $\varepsilon \gg k_B T$, b^2 can be expressed in terms of the kink concentration P_k:

$$\frac{b^2}{a_\perp^2} \approx P_k = 2e^{-\varepsilon / k_B T} \tag{2-13}$$

In the limit $\varepsilon \sim k_B T$, assuming nearest-neighbor interactions , a different formula applies:

$$b^2 = \frac{2a_\perp^2}{2 + e^{-\varepsilon / k_B T} + e^{\varepsilon / k_B T}} \tag{2-14}$$

2.3.2.2. Step correlation function

A measure for the step fluctuations is step correlation function *G(y,t)*

$$G(y,t) = \left\langle (x(y,t) - x(y_0, t_0))^2 \right\rangle \tag{2-15}$$

The correlation function *G(y,t)* represents the probability to find the step edge at position *x(y)* at time *t* when it has been located initially at a position $x(y_0)$ at a starting time t_0 [16]. *x* and *y* denote the axis parallel to the mean orientation of the step and the axis perpendicular to the direction, respectively. In the following, two cases of equation (2-15) are discussed, pure spatial

($G(y,t=0)$) and pure time ($G(y=0, t)$) fluctuations of infinite steps. In experiment (see chapter 5),

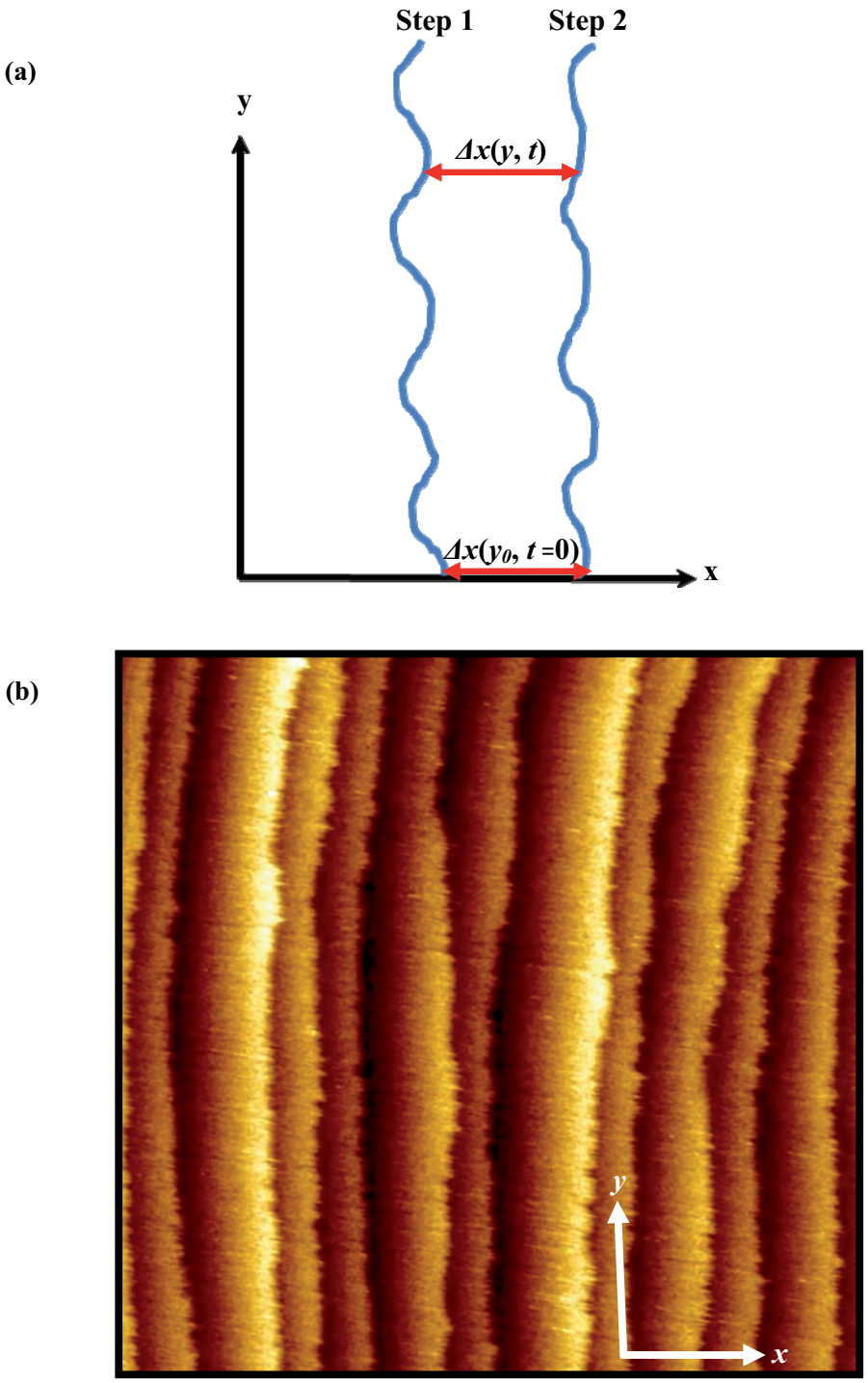

Fig.(2-9): (a) Sketch of step pair contour to define the spatial correlation function. (b) Normal STM image of Au(1 1 29) surface (vicinal to (001)-plane) in 100 mM $HClO_4$ + 1 mM KBr at -250 mV vs. SCE. **x** and **y** axes represent the step position and the spatial coordinate respectively. Displayed area along the steps (75.5 x 75.5 nm^2). (see text for discussion)

step fluctuations are measured as the mean square deviation of the difference Δx between the position of two adjacent steps (figure 2-9). This method allows to compensate for the thermal drift of the STM [37,38]. Then, the appropriate correlation function is:

$$G(y,t) = \frac{1}{2}\left\langle (\Delta x(y,t) - \Delta x(y_0,t_0))^2 \right\rangle \tag{2-16}$$

Case A: Spatial correlation function G(y, t=0)

In this case, the step structure is analyzed for constant time (*t=0*), i.e. surface diffusion is slow compared to the scan speed of the STM. The spatial correlation function *G*(*y*) is analyzed from normal STM images. For metal electrodes in electrolyte, the kink concentration and the kink mobility depend not only on temperature, but rather also on electrode potential. Hence, spatial step fluctuations in electrolyte may be analyzed not only at low temperatures ($\varepsilon \gg k_B T$) but also at low potentials where the surface diffusion is still negligible on the time scale on an STM image. The spatial correlation function is a linear function of the distance *y* along the step edge

$$2G(y) = \left\langle ((\Delta x(y) - \Delta x(0))^2 \right\rangle = \frac{b^2}{a_{\parallel}} |y| \tag{2-17}$$

Here, the initial distance along the step $y_0 = 0$.

Case B: Time correlation function G(y=0, t)

In the case of high kink mobility, the contribution of time information in the STM image becomes dominant compared to spatial information. Then, the correlation function has the form:

$$G(t) = \frac{1}{2}\left\langle (\Delta x(t) - \Delta x(0))^2 \right\rangle \tag{2.18}$$

Here, the initial time is set to $t_0 = 0$. The time correlation function can be directly determined from special STM images called “time images”: There, the tip scans a single line repetitively and

displays all lines in a pseudo image where the axis along the step edges is a time axis, and the axis perpindicular to the mean orientation of steps represents the step position coordinate [14] (figure (2-10)). The “step edges” in figure (2-10) are not real step contours, rather they are the representation of the variation of the positions of the steps over time in the respective scan line. Assuming that no drift alter the scanned surface area during the scanning process, a time image contains no spatial surface information along the “step edges”.

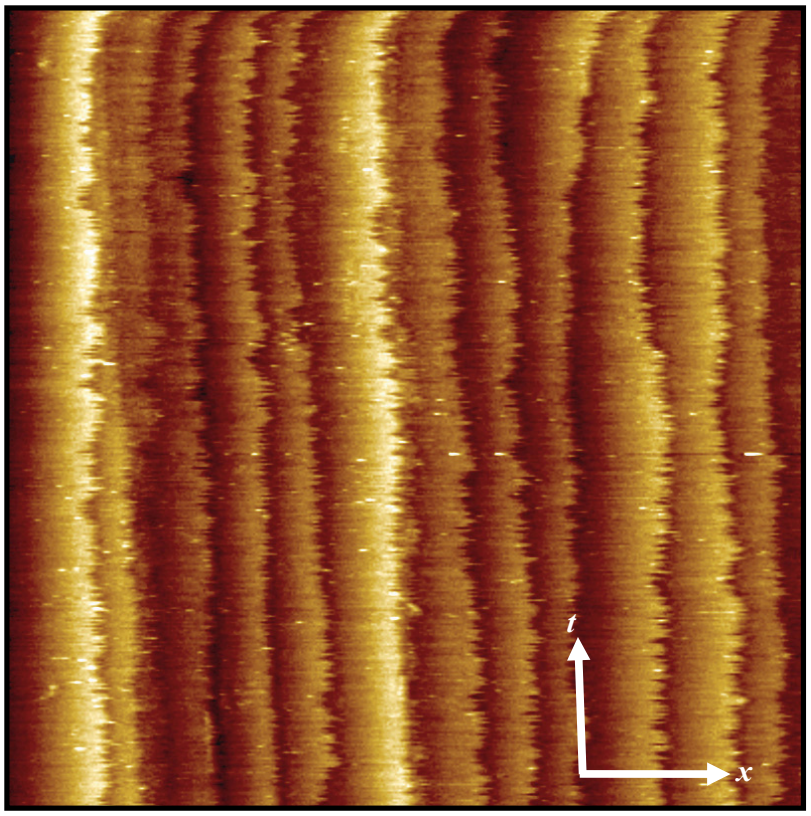

Fig.(2-10): Time STM image of Au (1 1 29) (vicinal to (001)-plane) in 100 mM $HClO_4$ + 1 mM HCl at +460 mV. vs. SCE. **x** and **t** axes represent the step position and the time coordinate respectively. Scanning time is 31.6 sec. Scan width is 62.1 nm.

As already described above, the relaxation of the system toward equilibrium is mediated by different mass transport mechanisms on the surface. The change in the step position with time as a result of the relaxation of the system toward equilibrium can be described by a Langevin equation. Here the steps are considered as one-dimensional fluctuating objects [63,14]. The

solution of the Langevin equation depends on the mass transport involved in the fluctuation of the steps. The theoretical solutions for different mass transport mechanisms have been presented by Pimpinelly [59], Khare and Einstein [64], Blagojevic and Duxbury [65]. According to the theoretical work, the time correlation function $G(t)$ obeys different time laws, depending on the mechanism of the mass transport processess involved in the fluctuations :

$$\frac{2G(t)}{a_{\perp}^{2}} = c(T,\phi)L^{\delta}t^{\alpha} \tag{2.19}$$

Here $c(T,\phi)$ is a temperature and electrode potential dependent pre-factor and L is the average distance between fluctuating steps. The exponents α and δ depend on the dominant mass transport process. Below, the different mass transport processes entering the theoretical solutions will be discussed.

(i) Equilibrium with vapor/electrolyte phase

In this case, atoms are emitted from the step edges to the adjacent terrace. After a mean diffusion time on the terrace, they are eventually exchanged with the vapor or electrolyte phase. Two limits must be distinguished: First, if the mean diffusion length l_s on the terrace before desorption is much smaller than the mean distance between the steps L and second, l_s is of the order of L or even larger. In the first case, only the vapor/electrolyte can serve as a source for atoms desorbing from the surface and vice versa (left panel in figure (2-11)). Then, the time correlation function has the form

$$\frac{2G(t)}{a_{\perp}^{2}} = (P_K\ c_s)^{1/2}\left(\frac{D_s}{\tau_{sv}}\right)^{1/4} t^{1/2} \tag{2.20}$$

Here, c_s is the adatom concentration on the terrace, D_s the diffusion constant for adatoms on the terrace, τ_{sv} is the mean diffusion time of an atom on the terrace before it desorbs into the vapor

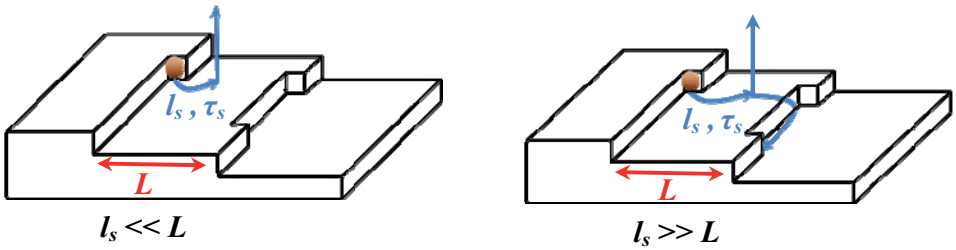

Fig.(2-11): Schematic illustration of the mass transport process which involves the exchange of atoms with the vapor/electrolyte phase. **Left:** No exchange between adjacent steps, time correlation function independent of *L*. **Right:** Atoms exchange between steps, time correlation function depends on *L*.

/electrolyte phase. In the second case (right panel in figure (2-11)), the neighboring steps serve also as sinks or sources for atoms. Then, the time correlation function depends on the mean step-step distance *L*

$$\frac{2G(t)}{a_{\perp}^2} = \left(P_K \frac{c_s}{\tau_{sv}} \right)^{1/2} L^{1/2}\, t^{1/2} \qquad (2.21)$$

Generally, this case does not apply in vacuum where atom desorption is negligible. It is, however, assumed to be an important process for metal electrodes in contact with an electrolyte [44].

(ii) Rapid exchange of atoms between steps

In this case, the diffusion of atoms on the terrace is fast, and the sink for the atoms are the neighboring steps (figure (2-12)). Then, the time correlation function becomes

$$\frac{2G(t)}{a_{\perp}^2} = (c_t\, D_t\, P_K)^{1/2}\, L^{-1/2}\, t^{1/2} \qquad (2.22)$$

This kind of mass transport process is described by a time exponent 1/2 similar to equation (2-21), however, with the inverse power dependence on the mean distance between steps *L*. The inverse

power dependence on L enables to distinguish between the two different mass transport situations.

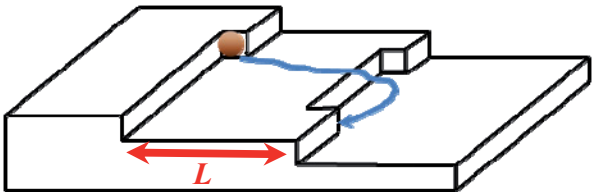

Fig.(2-12): Schematic illustration of the mechanism of rapid exchange of atoms between steps.

(iii) Exchange of atoms with terraces and terrace diffusion

(a) *Fast terrace diffusion*

In this case, the atoms are emitted from a step, and they fastly diffuse across the terrace. The atoms are then captured by the same step at different position (left panel in figure (2-13)). The time correlation function becomes

$$\frac{2G(t)}{a_{\perp}^{2}} = \left(\frac{P_K}{\tau_a}\right)^{1/2} t^{1/2} \qquad (2.23)$$

with τ_a the average time between two detachment/attachment processes of atoms from a step site to the terrace [39,40]. This kind of mass transport applies when the attachment/detachment process of atoms from step sites to the terrace is slow compared to terrace diffusion [14] .

(b) *Slow terrace diffusion*

For the case of slow terrace diffusion compared to the attachment/detachment process, $G(t)$ obeys a $t^{1/3}$- law (right panel in figure (2-13)) [41].

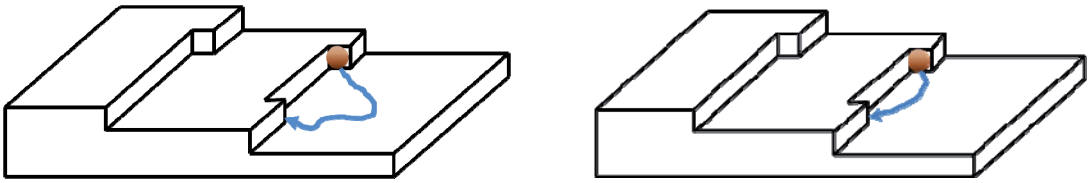

Fig.(2-13): Schematic illustration of the exchange of atoms with the terrace in case of fast (left) terrace diffusion and slow (right) terrace diffusion .

(iv) Rapid exchange of atoms with the terrace in the presence of a large Ehrlich-Schwoebel barrier

This case is similar to that in (ii), except that the step itself is the sink for the atoms. The atom is emitted from the step, diffuses on the neighboring terrace and attaches to the same step at a different site. Atom attachment to neighboring steps is suppressed due to an extra energy barrier that has to be overcome when the atoms approach the neighboring step [42,43]. This extra energy barrier is called Ehrlich-Schwoebel barrier ($\boldsymbol{E_s}$) (see the right panel in figure (2-14)).

In the case of terrace diffusion in presence of an Ehrlich-Schwoebel barrier, the time correlation function *G(t)* becomes:

$$\frac{2G(t)}{a_{\perp}^{2}} = P_{k}^{3/4}\left(c_{t}\, D_{t}\right)^{1/4} L^{1/4}\, t^{1/4} \qquad (2.24)$$

The Ehrlich-Schwoebel barrier gives rise to an L dependence of the time correlation function with exponent 1/4. Due to this L-dependence, this case is easily distinguished from the case of step edge diffusion discussed next.

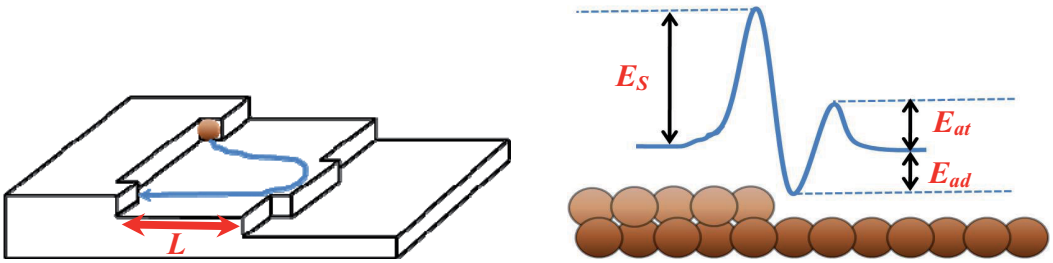

Fig.(2-14): Left: Schematic illustration of the rapid exchange of atoms with the terrace in the presence of a large Ehrlich-Schwoebel barrier. **Right**: Sketch of the relevant energy barriers when an atom approaches the step from the upper terrace (Schwoebel barrier E_s). E_{at} is the attachment barrier from the lower terrace which might exist additionally to the Schwoebel barrier. The energy barrier E_{ad} corresponds to the formation energy of an atom on the terrace from the step side.

(v) Step-edge diffusion

Here, the step itself serves as a source and a sink of atoms. The exchange of atoms with the neighboring terrace is negligible (figure (2-15)), and the time correlation function does not depend on L :

$$\frac{2G(t)}{a_{\perp}^{2}} = P_k^{3/4} \left(c_{st} D_{st}\right)^{1/4} t^{1/4} \qquad (2.25)$$

Here, c_{st} and D_{st} are the adatom concentration and the step-edge diffusion constant for atoms moving along the steps, respectively.

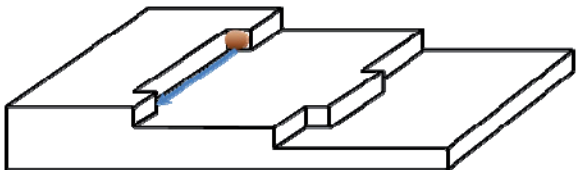

Fig.(2-15): Schematic illustration of the step-edge diffusion process.

Chapter 3

Experimental Details

3.1. Au(11*n*) surfaces

3.1.1. Preparation of Au(11*n*) surfaces

Au(1 1 *n*) surfaces were cut from gold single crystal rods (99.999% Mateck). Crystal plates were cut from the rod using spark erosion. The crystal plates were 12 mm in diameter and had a thickness of 2 mm. Diffractometry was used to monitor the orientation of the crystals. The crystal plates were then mechanically polished to obtain atomically smooth surfaces and to get the desired surface orientation. The accuracy of the surface orientation is within 0.1°. This accuracy is limited by the mosaic structure of a high-quality single crystal [17,45,46]. After preparation, the crystals were carefully stored in a box with Kleenex tissue material on top of the polished face.

Au(1 1 *n*) surfaces as used in this work have Miller indices *n*=7,9,11,17 and 29 corresponding to miscut angles between 2.79° and 11.42° relative to the (001) plane (see 2.1.2). Figure (3-1) shows a ball model of the Au(1 1 9) vicinal surface. Ideally, this surface consists of parallel monatomic high {111}-type steps, separated by (001) terraces. The surface is inclined with respect to the Au(001) surface by θ =8.93°, the average terrace width is $L = 4.5\,a_{\perp}$ (in Au(11*n*) vicinal surfaces, $a_{\perp} = a_{\parallel} = 0.288$ nm). Table (3-1) shows the inclination angle θ and the average terrace width *L* for Au(11*n*) surfaces used in this work .

Table(3-1): The inclination angle θ and the corresponding average terrace width *L* of Au(11*n*), *n*=7,9,11,17and 29.

	Au(1 1 7)	**Au(1 1 9)**	**Au(1 1 11)**	**Au(1 1 17)**	**Au(1 1 29)**
θ/°	11.42	8.93	7.33	4.76	2.79
***L*/nm**	1.01	1.30	1.58	2.45	4.18

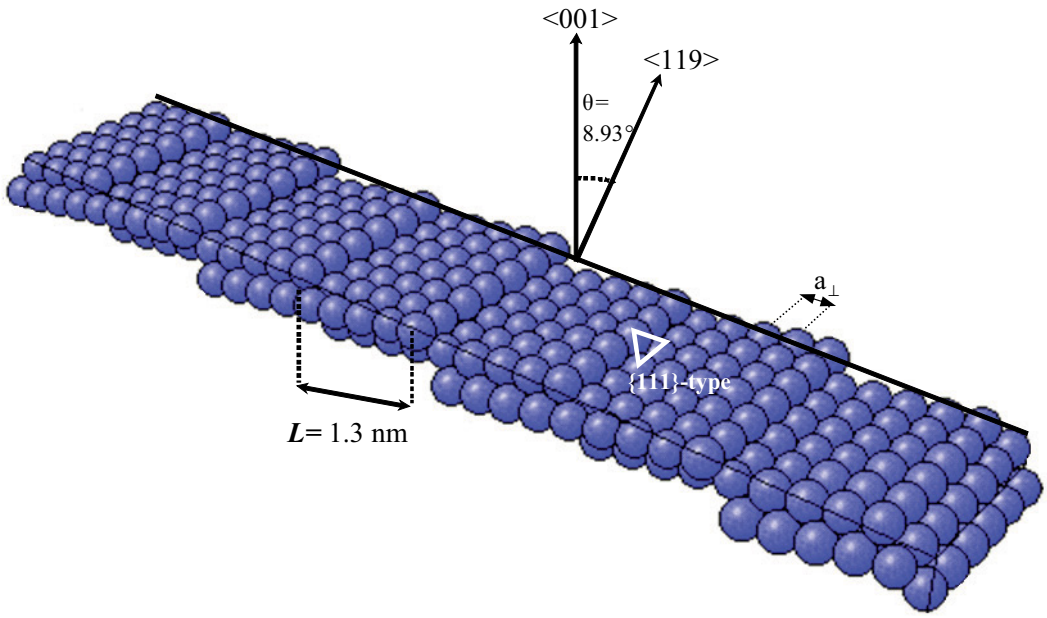

Fig.(3-1): Ball model of the Au(119) vicinal surface [9].

3.1.2. Flame annealing

Prior to use in an electrochemical STM, the single crystals were further more prepared as described in the following: The freshly polished surfaces still contain for instance contaminations. For electrochemical measurements, the common method to clean metal surfaces like Au and Pt is flame annealing [11]. Organic contaminations are desorbed form the surface and residual defects are healed due to the increased mobility of surface atoms. In the following, the annealing procedure used in this thesis is described in detail: Throughout the entire procedure, the Au single crystal is handled carefully using a non-metallic tweezer (e.g. ceramic tweezer) to avoid damage of the crystal edges. Firstly, the crystal is washed carefully with Milli-Q water (Millipore, 18.2 MΩ cm^{-1}, organic compounds < 5 ppm (part per million)). A very gentle flow of N_2 gas is then used to dry the crystal surface. Subsequently, the crystal is placed on a ceramic plate. The latter serves as a support for the crystal during flame annealing. A butane flame (85% butane, 15% propane) is used for flame annealing, performed in a darkened room.

The total annealing time is around 12 minutes, divided into 3 periods: First, the sample is indirectly heated by annealing the ceramic support carefully. Second, the sample is slowly moved towards the flame which is then moved over the sample in a zigzag manner. Careful annealing of the sample is absolutely necessary to avoid destruction of the sample by exposing the flame directly to the sample surface. The color of the sample is used to estimate its temperature. The temperature should be high enough such that the mobility of surface atoms is high enough to heal out bulk and surface defects. It should however not exceed the melting temperature of the crystal. The desired temperature is reached when the sample appears in red color; the estimated sample temperature is then between 750 C° and 850 °C. The sample turned out to be overheated when its color was yellow or bright-red. After reaching the desired temperature of 750-850 C° (approximately after 3-4 minutes), the flame is slowly moved away from the sample in order to cool down the sample within 4 minutes. Then the sample is carefully covered with glass and cooled down to room temperature within 10 minutes.

3.2. STM experiment

3.2.1. Topometrix TMX 2010 Discoverer STM

In this thesis, the measurements were performed with the electrochemical version of the **Topometrix TMX 2010 Discoverer** scanning tunneling microscope (STM) (Figure (3-2)). The basic principle of the electrochemical STM was described in section (2.2.3). All data was obtained at room temperature and in the constant-current mode. The STM instrument is placed on a vibration isolated table (Newport). The **Topometrix STM** is equipped with a video camera placed in the STM head to monitor the tip approach toward the sample. The camera is very useful to control the distance of the tip above the sample in order to avoid a tip-sample crash during tip approach. Figure (3-3) shows the tunneling unit of the STM. The STM head shown in the figure consists of an integrated STM tube scanner and a piezo tube which has a response of 5 nm/V [47]. The tip is mounted to the end of the piezo tube and located directly above the electrochemical cell. The micrometer screws are used to roughly adjust the vertical position of the tip above the electrochemical cell manually. The rough approach is monitored using the integrated video camera. The software-controlled fine adjustment screw shown in the figure are

used to approach the tip toward the cell by a stepper motor until the system is in the tunneling (feed-back) regime. The electrochemical cell is moved electronically in x and y direction in order to scan different areas of the sample. The maximum scan area for the particular scanner used in the experiments is 1µm x 1µm.

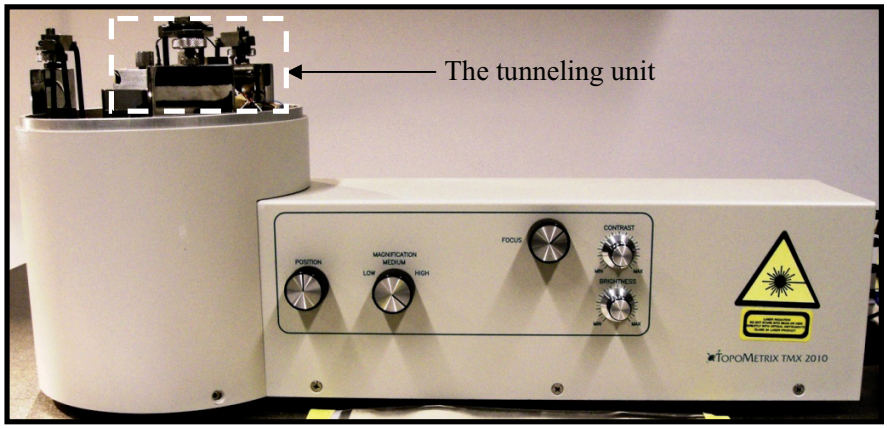

Fig.(3-2): The electrochemical version of the **Topometrix TMX 2010 Discoverer** scanning tunneling microscope (STM).

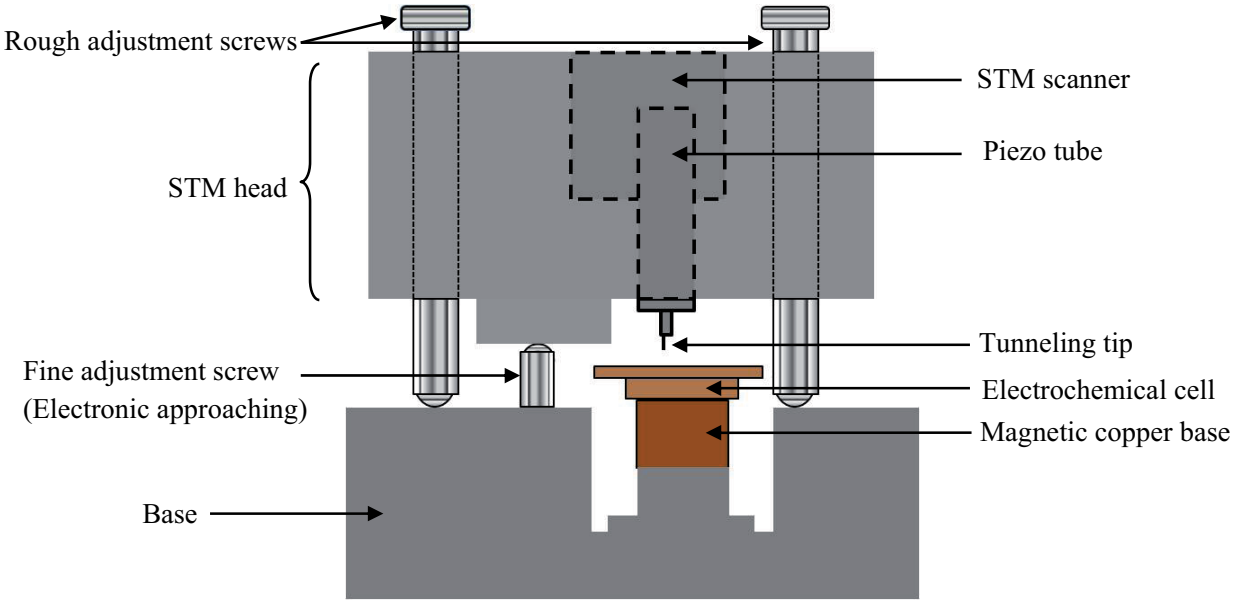

Fig.(3-3): Illustration of the tunneling unit of the **Topometrix TMX 2010** electrochemical STM

The electrochemical cell is placed on a magnetic copper base. The magnetic copper base is not the original as delivered with the **Topometrix STM**. Rather it is a home-made temperature stage designed in our institute [60]. The temperature stage was, however, not used in this thesis.

The electrochemical cell as used in this thesis is shown in figure (3-4). It consists of the Au sample placed in the cell-base made from nickel, which is designed particularly for the electrochemical STM measurements. An O-ring (Kalrez Spectrum) is used to prevent leakage of solution into the nickel cell-base. A lid made from Teflon is used to cover the cell, fix the crystal tightly and hold counter and reference electrodes (left of figure (3-4)). Counter and reference electrodes are made from Pt wires (99.999% purity, Goodfellow, Diameter Ø = 0.5 mm).

The potentials of the Au sample (working electrode) and of the W tip are measured with respect to the Pt reference electrode. However, all data presented in this thesis are given with respect to the saturated calomel electrode (SCE). The SCE electrode is a standard electrode which has a half-cell composition consisting of $Hg/Hg_2Cl_2/KCl$ saturated in water [20].

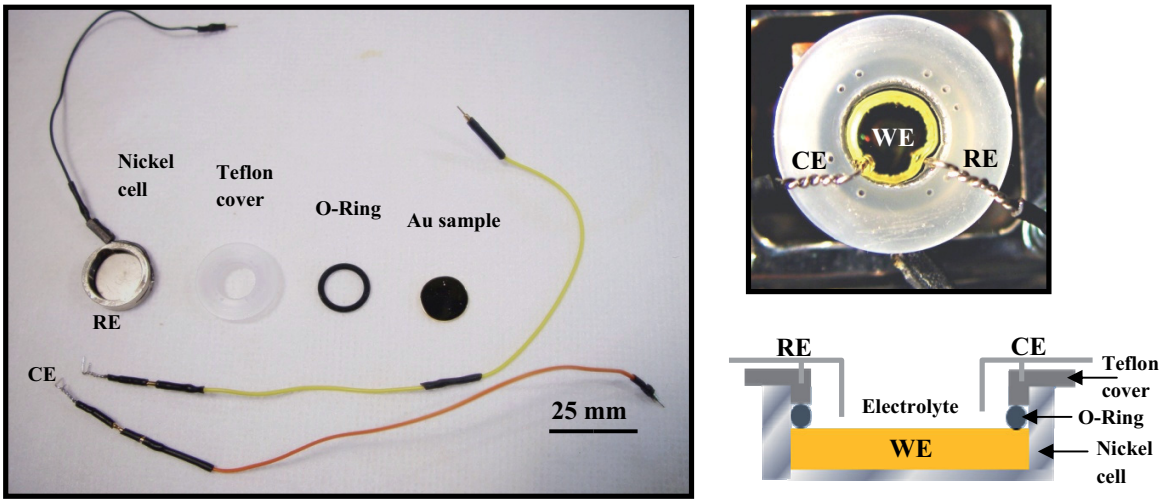

Fig.(3-4): Left: The components of the electrochemical cell used in the STM measurements. **Right-up**: Top view of the assembled electrochemical cell. **Right-bottom**: Schematic drawing of the cross section of the electrochemical cell.

3.2.2. STM tips

(i) Etching tungsten tips

It is well known that high resolution STM images are obtained when clean and sharp tips are used which can be generated using electrochemical etching. The electrochemical etching is considered as the easiest and cheapest tip preparation method. In the experiments presented here, tungsten (W) tips were used as STM probes. The experimental setup used for the electrochemical etching is shown in figure (3-5).

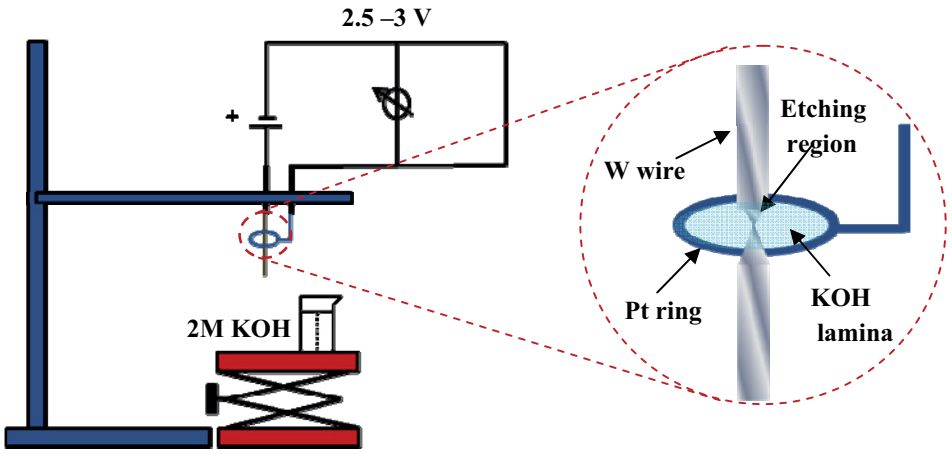

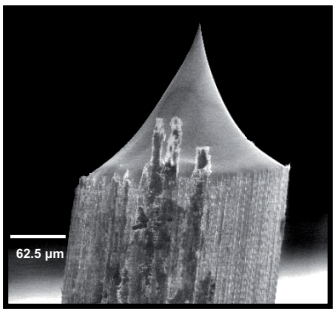

Fig.(3-5): Top: Illustration of the setup for DC electrochemical etching. **Bottom**: SEM image of the upper part of an etched tungsten tip.

The following procedure is adopted for etching W tips: Poly-crystalline W wires (99.98% purity. Diameter Ø = 0.25 mm) were straightened using a metallic tweezer. A circular Pt wire serves as ring electrode during etching. Prior to its usage, it is cleaned with Milli-Q water and annealed using a butane flame. The straightened W wire is mounted vertically approximately in the centre of the Pt ring. The lower part of the W wire and the Pt ring are immersed into a beaker containing a solution of 2M KOH (Suprapure, Merck). After carefully removing the beaker, a thin film (lamina) of KOH solution is formed in the Pt ring (figure (3-5)). Before starting the

etching process, a Teflon block is positioned below the W wire. The Teflon block carries a hole of diameter Ø~5 mm in which the W wire fits. Etching starts with applying a DC voltage of 2.5-3 V between the W wire and the Pt ring that serve as anode and cathode, respectively. The flowing current in the electrochemical cell is monitored using a multimeter (VOLTCRAFT) and it is in the order of 1-8 mA. During the etching process the immersed part of the W wire is oxidized and dissolved as WO_4^{2-} anions in solution. Due to the oxidation, the wire becomes thinner in the etching region. The hydrogen evolution takes place on the Pt ring and it is observed as bubbles .The current decreases as the contact area decreases and the diameter of the W wire in the etching region shrinks. As the contact area decreases with time, the wire eventually breaks and the lower part falls down to the hole in the Teflon block below the W wire. As soon as the W wire falls down the electric circuit is switched off automatically. The upper part of the W wire is still mounted to the etching setup. The upper part of the etched W wire is mostly used in the experiment described in this thesis, since it is sharper and shorter than the lower part. Hence, the upper W tip is more stable during the STM experiments. The prepared tip is then carefully handled with a tweezer and washed gently in Milli-Q water and dried in an Ar flow. The lower part of figure (3-5) shows the SEM image of an STM tip prepared the way described before.

(ii) Coating W tips

The W tips used in STM are coated with clean Polyethylene (PE) (Meister-Werkzeuge) insulator to decrease the tip area exposed to the electrolyte and reduce the faradaic contribution to the tunneling current (see section 2.2.3). Figure (3-6) shows schematically the method used for tip coating: The tip is inserted to a hole in a heating plate (image (a)). Then a small piece of clean PE is placed besides the tip. The PE piece is melted, and the tip is lowered such that it is completely covered with PE (image (b)). The PE solidifies upon cooling. Then, the tip is slowly moved upwards (image (c)) until the desired total length of coating is achieved. This process is monitored using a telescope. The coated tip is then removed from the holder using a metallic tweezer. To avoid further contaminations the tips were kept in a closed box until they were used for the STM experiment. In the experiments presented here typical residual faradaic current contributions are of the order of 5-6 pA. This value is much lower than the tunneling current of about 2 nA as used in the experiments. Hence, no interference between faradaic contribution and

tunneling current is expected. The STM tips were usually prepared one day ahead of an experiment.

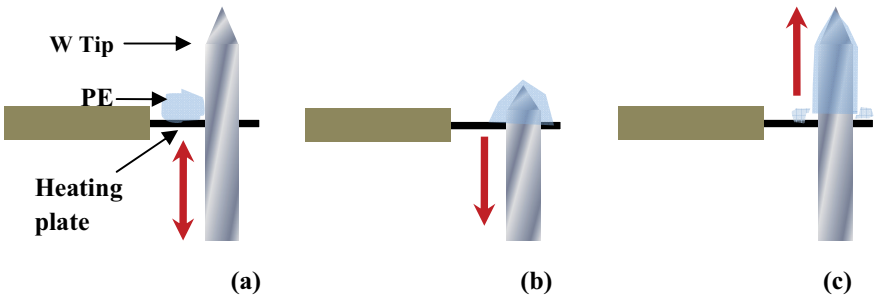

Fig.(3-6): Drawing illustration shows the setup and for coating W tips with PE. (see text for the discussion).

3.2.3. Additional preparations prior to STM experiment

The entire glassware used for electrolyte preparation is soaked overnight in Piranha solution in order to clean the glassware from organic residues. The Piranha solution is prepared from H_2SO_4 (96%, Merck) and H_2O_2 with a ratio 3:1. The plastic tweezers used for handling the electrochemical cell components are kept overnight in pure H_2SO_4 solution. On the day ahead of the STM experiment, all glassware, two O-rings, two Teflon lids as well as the plastic tweezers are removed from the Piranha solution and washed several times with Milli-Q water. Everything is then cooked for 10 minutes in Milli-Q water and washed once more in Milli-Q water. This procedure is repeated 5 times. In the final cycle, the electrolyte is prepared. In this thesis, the experiments were performed in three different electrolytes: 10 mM H_2SO_4 (96%, Suprapure, Merck) for the studies of the step bunching instability (chapte4), and 1mM HCl (30%, Suprapure, Merck) +100 mM $HClO_4$ (70%, Suprapure, Merck) , 1mM KBr (99.999%, Suprapure, Merck) + 100 mM $HClO_4$ for the studies of the equilibrium step fluctuations (chapter 5). Then, the Au samples are prepared as described in section (3.1.2), and the electrochemical cell is assembled according to figure (3-4). Prior to mounting the Teflon lid, the Pt wires are annealed using a butane flame. It is essential not to touch the sample surface during the cell assembly.

Otherwise the sample surfaces could be contaminated or scratched. The STM instrument is switched on at least 2 hours prior to experiment to guarantee stable tunneling conditions. The coated W tip is then mounted to the STM, and the electrochemical cell is placed on to the copper base in the STM (figure (3-3)). A total volume of about 250 µl electrolyte is then added carefully to the cell. The filling of the cell with the electrolyte is very critical, since the first drops of the electrolyte should first touch the reference electrode rather than the sample. Otherwise, the potential control between the sample and reference electrode is lost. The Au sample potential is monitored by a bipotentiostat (**Topometrix Bipotentiostat** (figure (3-7)). The potential is determined with an accuracy of about ±50 mV. The error is due to the use of Pt quasi-reference electrodes which are not as stable as e.g. SCE. In most of the STM experiments, the maximum time available for measurements is about 2 hours. This is due to the fact that an open STM cell is used where the electrolyte is in contact with the surrounding laboratory atmosphere. After typically 2 hours, contamination of the surface in the electrolyte becomes visible in the STM images.

Fig.(3-7): The **Topometrix bipotentiostat** used in the EC-STM experiments.

Chapter 4

Step bunching instability on Au(11*n*) in electrolyte

4.1. Introduction

As mentioned in the previous chapter, the ideal vicinal surface consists of a regular array of equally spaced steps, separated by flat terraces. This morphology is stabilized by elastic repulsive interactions between the steps. The regular step array, however, might not always be the energetically favorable surface configuration. In such a case, the surface may rather undergo a phase separation into areas with high step density (*step bunches*), and flat areas almost free of steps. In this case the surface is unstable against step bunching. Both, the bunched and flat areas have different surface orientations compared to the nominal surface, however due to mass conservation, the net surface orientation is conserved. Figure (4-1) shows schematically the surface morphology of a vicinal surface with (a) equally spaced steps and (b) a surface with the same nominal orientation as in (a), however, with a large step bunch. The nominal (1 1 *n*) orientation breaks up into new orientations (1 1 n_1) and (1 1 n_2), representing the step bunch and the almost flat area, respectively.

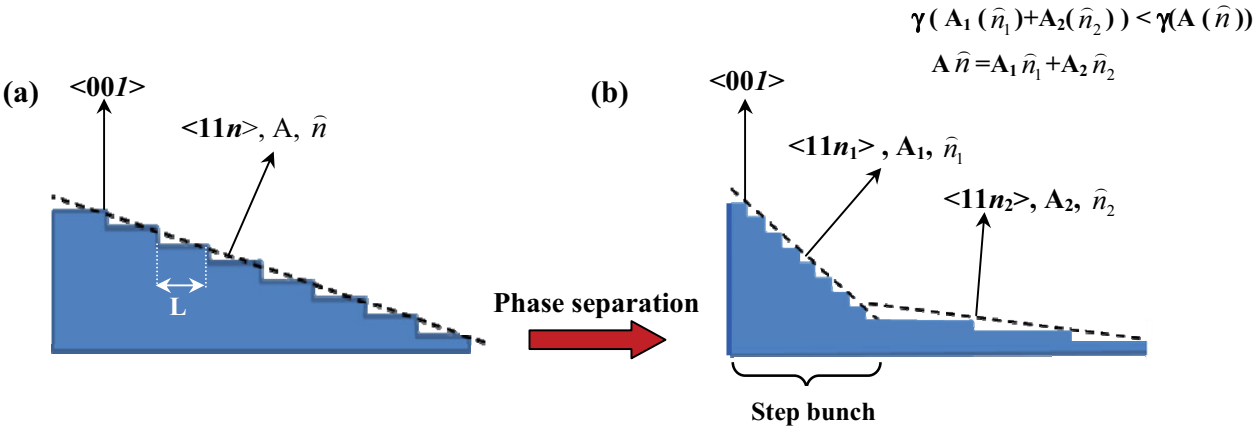

Fig.(4-1): Sketch of a vicinal surface (11*n*) with (a) equally spaced steps and (b) with an area (11n_1) with high step density (step bunch) and an area (11n_2) almost free of steps. $\hat{n}$ = <11*n*>, $\hat{n}_1$ = <11n_1> and $\hat{n}_2$ = <11n_2>, are the unit surface normals to the planes with areas A, A_1 and A_2 respectively.

The specific surface tension γ (i.e. work per area) of a vicinal surface is a function of the surface orientation tan θ (equation (2-10)). Hence, in case of a phase separation, the new surface configuration has a lower total surface tension and is energetically more favorable [52].
Step bunching instabilities have been studied extensively in ultra high vacuum under non-equilibrium conditions such as crystal growth, electromigration and sublimation [53,54,55] as well as theoretically [56,57,58,59] for surfaces like Si. Only little research has been performed for surfaces in contact with an electrolyte. Quantitative studies on step bunching phenomena in electrolyte have entirely neglected. This thesis tries to fill this gap.

In the following chapter, quantitative experimental studies on step bunching on vicinal Au(11n) surfaces in electrolyte will be presented.

4.2. Step bunching on Au(1 1 *n*) surfaces in electrolyte

4.2.1. STM images and height profile analysis on Au(1 1 7), Au(1 1 9) and Au(1 1 11)

The electrode surfaces were prepared according to section (3.1) and immersed into electrolyte under electrode potential control. The STM images were recorded with 400x400 pixel resolution in the constant current mode. Figures (4-2), (4-3) and (4-4) show representative STM images of the Au(1 1 7), Au(1 1 9) and Au(1 1 11) in 10 mM H_2SO_4 at an electrode potential ϕ = -170 mV vs. SCE. In the STM images, a plane is subtracted in order to enhance the contrast. The lower part of the figures shows the height profile of the marked area in the STM images. The height profile represents an average over all line scans within the white rectangle. From obviously (100)-oriented terraces, a 0°-reference was determined. Then, a linear function has been subtracted from the height profile in (b) in order to display the (100)-regions as horizontal lines (red arrow in figures (4-2), (4-3) and (4-4)). According to table (3-1), the ideal nominal Au(1 1 7), Au(1 1 9) and Au(1 1 11) surfaces are inclined with respect to the (100) plane by 11.42°, 8.93° and 7.33° respectively. The height profile as shown in figure (4-2) reveals locally differently oriented phases. The local orientations correspond to regions with steep (i.e. step bunch regions) and small slopes (i.e. almost step-free regions). The steeper regions correspond to (1 1 11), (1 1 7), and (1 1 9) orientations, and the flatter to (1 1 59) or (1 1 37). Examples of the flat (100) face and the step bunch region are indicated by arrows in the STM image.

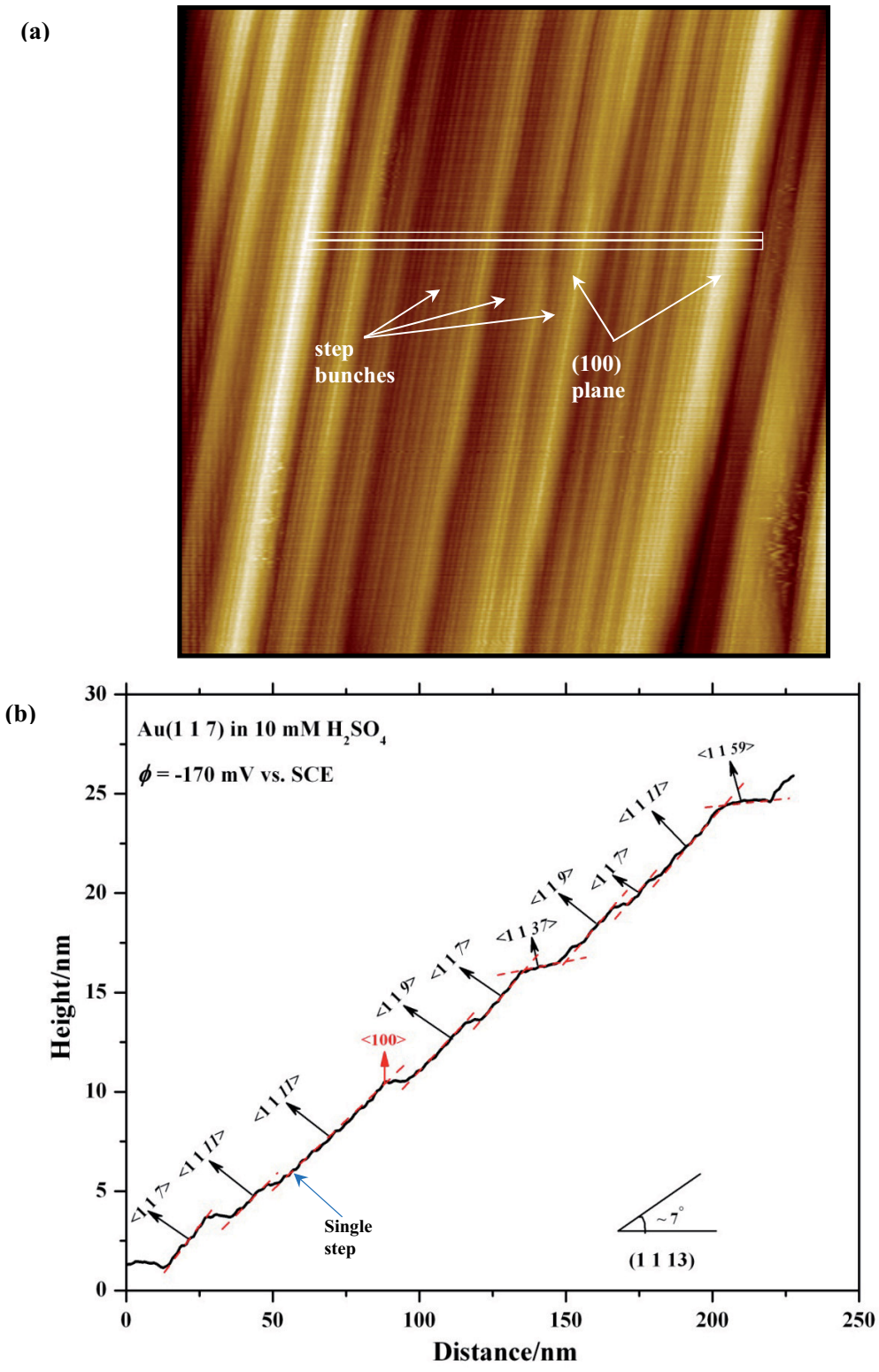

Fig.(4-2): (a) STM image of the Au(1 1 7) electrode after flame annealing and immersion into 10 mM H_2SO_4 at room temperature and ϕ = -170 mV vs. SCE. The displayed area is 316x316 nm^2. Step bunch regions and flat (100) planes are indicated by arrows. (b) The average height profile of the area marked by three scan lines in (a). The inspected area has (1 1 13) orientation. An example of a single monatomic high step is indicated by the blue arrow in (b).

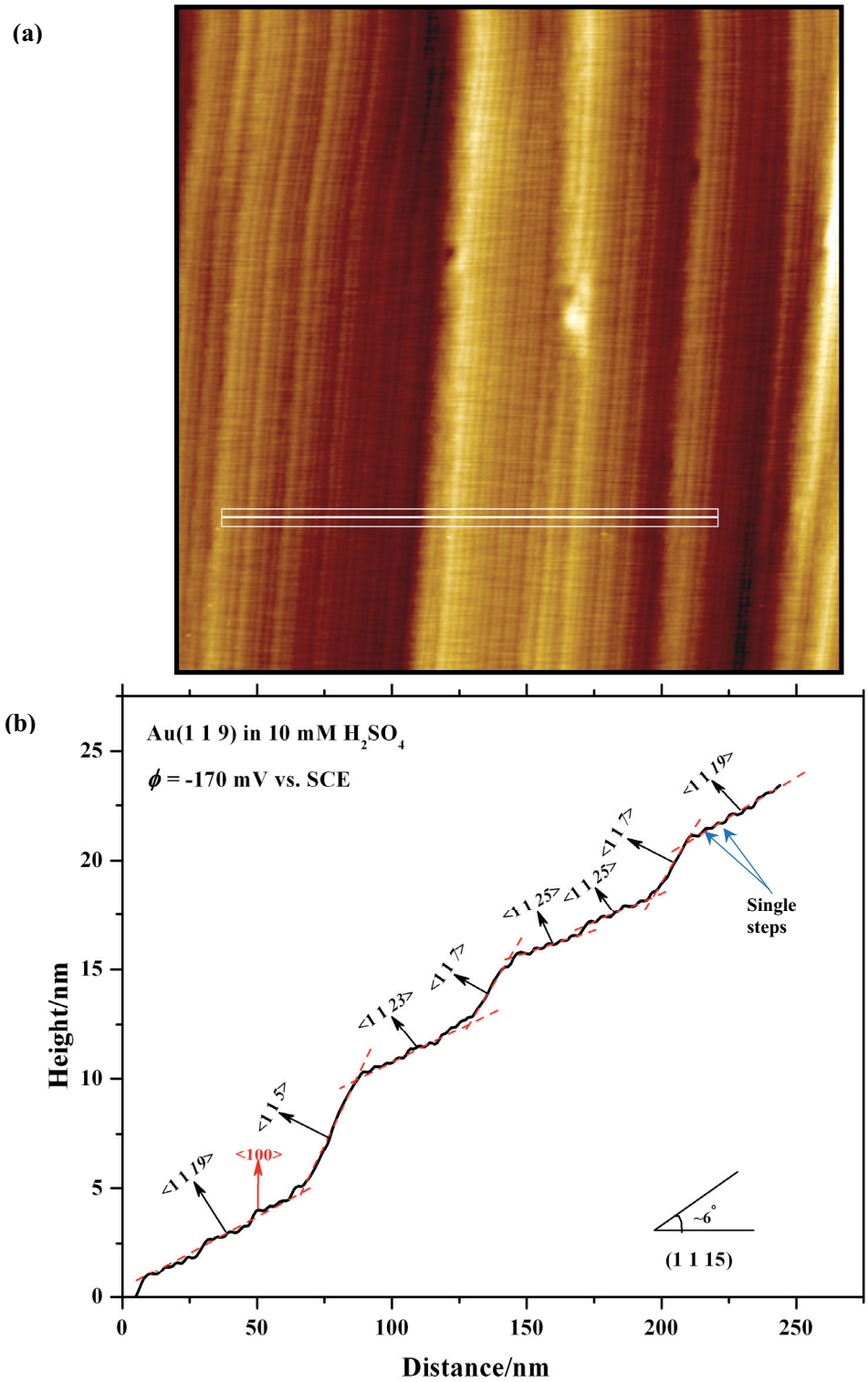

Fig.(4-3): (a) STM image of the Au(1 1 9) electrode after flame annealing and immersion into 10 mM H_2SO_4 at room temperature and ϕ = -170 mV vs. SCE. The displayed area is 352x352 nm^2. (b) The average height profile of the area marked by three scan lines in (a). Examples of observed single steps are indicated by blue arrows in (b).

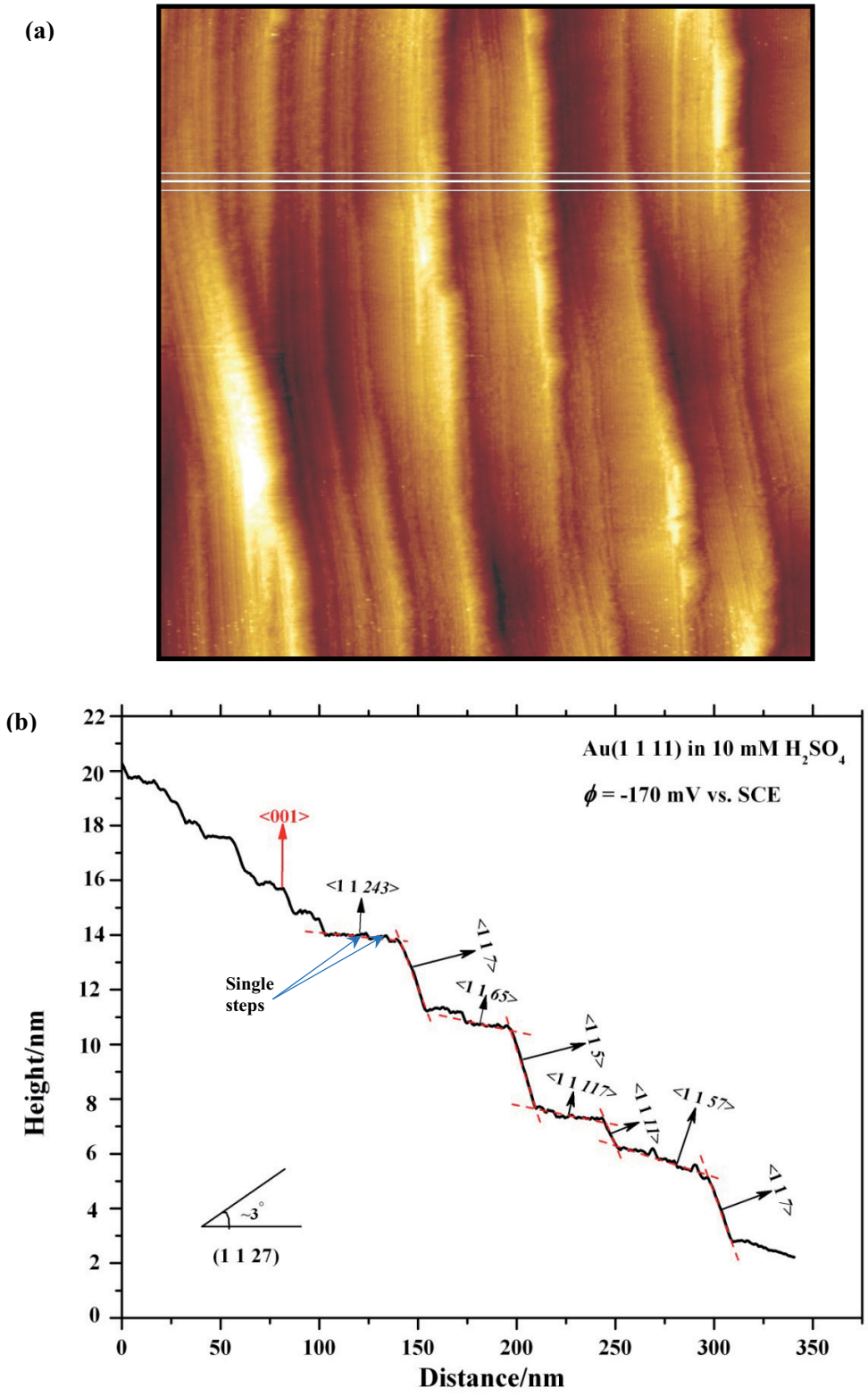

Fig.(4-4): (a) STM image of Au(1 1 11) electrode after flame annealing and immersion in 10 mM H_2SO_4 at room temperature and ϕ = -170 mV vs. SCE. Displayed area is 340x340 nm^2. (b) The average height profile of the area marked by three scan lines in (a). Examples of observed single steps are indicated by blue arrows in (b).

The inspected area in figure (4-2) is inclined by ~7° with respect to the (100) plane, which corresponds to a (1 1 13) orientation. This plane has a broader terrace width than the nominal (1 1 17) surface. Examples of monatomic high steps are marked by blue arrows in the height profile. In fact, most of the stripes observed in the STM images are small step bunches rather than single steps.

Figure (4-3) shows another example, now for Au(1 1 9) in 10 mM H_2SO_4 at ϕ = -170 mV vs. SCE. The surface reveals a phase separation into steep regions with (1 1 7) and (1 1 5) orientations and flatter regions corresponding to (1 1 25), (1 1 23) and (1 1 19). As shown in the height profile, the single steps are clearly visible within the flatter regions (see e.g. marked blue arrows for the (1 1 19) face). The net orientation of the entire surface area displayed in the STM image is (1 1 15) surface; i.e. it corresponds to a surface with wider terraces than nominal (1 1 9).

As shown in figure (4-4), Au(1 1 11) in 10 mM H_2SO_4 at ϕ = -170 mV vs. SCE restructures into (1 1 7), (1 1 5) and (1 1 11) and flatter regions (1 1 243), (1 1 65) and (1 1 117). The latter planes have very small inclination angles to (100) (0.33°, 1.25°, 0.69°, respectively).

As can be seen from the STM images and the height profiles above, the inspected surfaces show local phase separations corresponding to regions with large angles θ with respect to the (100) plane (θ ~ 14°-16°) and regions with small angles (θ ~ 2.8°- 8.5°). In order to determine the probability to find a particular orientation with respect to the (100) plane, the distribution of slopes averaged over a large surface region was measured. For a representative mean distribution, the height profile analysis was performed for 33-40 different STM images taken at different positions on the surface. In addition, this analysis was repeated for three different electrode potentials. To analyze the STM images quantitatively, an algorithm was employed which detects single steps and step bunches containing two or three steps. Surface sections that consist of a sequence of two or three steps separated by small (100) terraces were interpreted as an area with a common mean orientation.

Figure (4-5) shows the probabilities to find a particular local orientation on Au(1 1 9) in 10 mM H_2SO_4 at ϕ = -150 mV, +50 mV, and + 150 mV vs. SCE. At ϕ = -150 mV, the mean slope of the inspected total surface area is 0.115 which corresponds to n=12.3. For ϕ = +50 mV and +150 mV vs. SCE, the mean orientation corresponds to θ=4.7° and 4.2° (n =17.3 and n =19.3), respectively. Hence, the mean orientation of the inspected total area does not correspond to the

mean orientation of the nominal (1 1 9) (i.e. θ =8.93°) for each histogram. This may be due to the fact that areas with very steep slopes on the crystal surface have been systematically neglected in experiment. The reason may be that the STM resolution improves on less steep surface areas which increases the probability to successfully record STM data from surface areas with less steep slopes. This is also corroborated by the fact that we rarely observed surface sections with local orientations corresponding to (1 1 3) faces. They nevertheless exist as shown in figure(4-6). There, an example of an extended surface section with an orientation close to (1 1 3) is presented. The steep slopes in figure (4-6) have a mean orientation tan $\theta \sim 0.5$ (i.e. $\theta \sim 26.5°$) corresponding to $n \sim 3$.

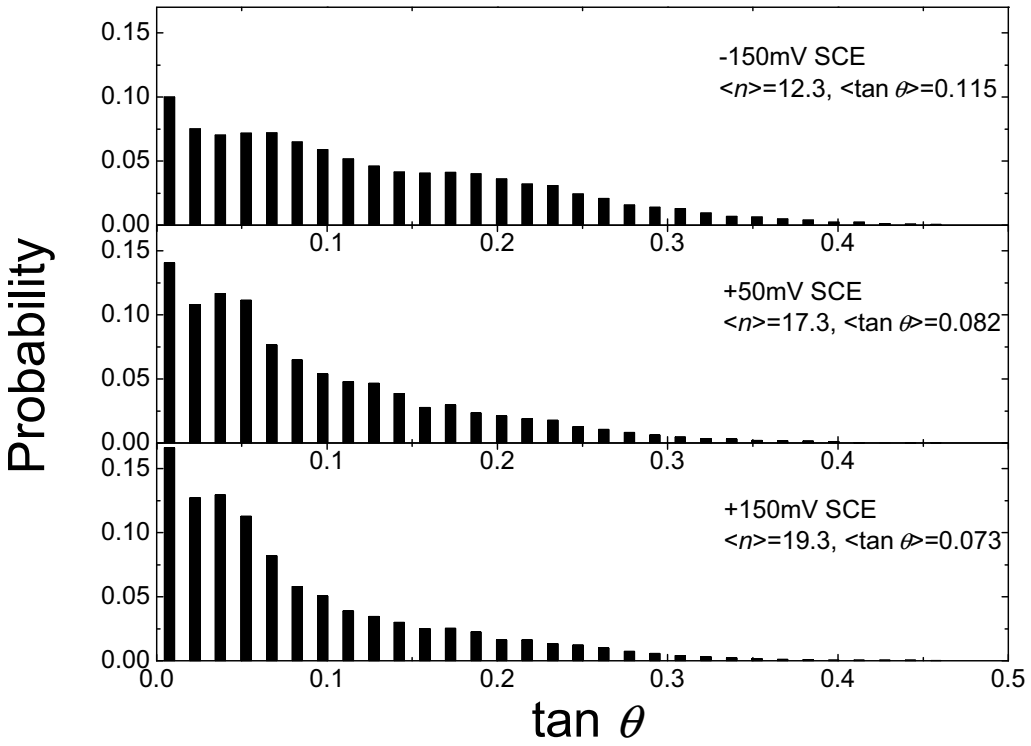

Fig.(4-5): Probability distributions to find a particular local slope (tan θ) on Au(1 1 9) for three different electrode potentials. The distributions are obtained from line profiles similar to that shown in figure (4-3). The data was obtained from averaging over 44 (+50 mV), 44 (+50 mV) and 32 (+150 mV) images taken from different areas on the surface.

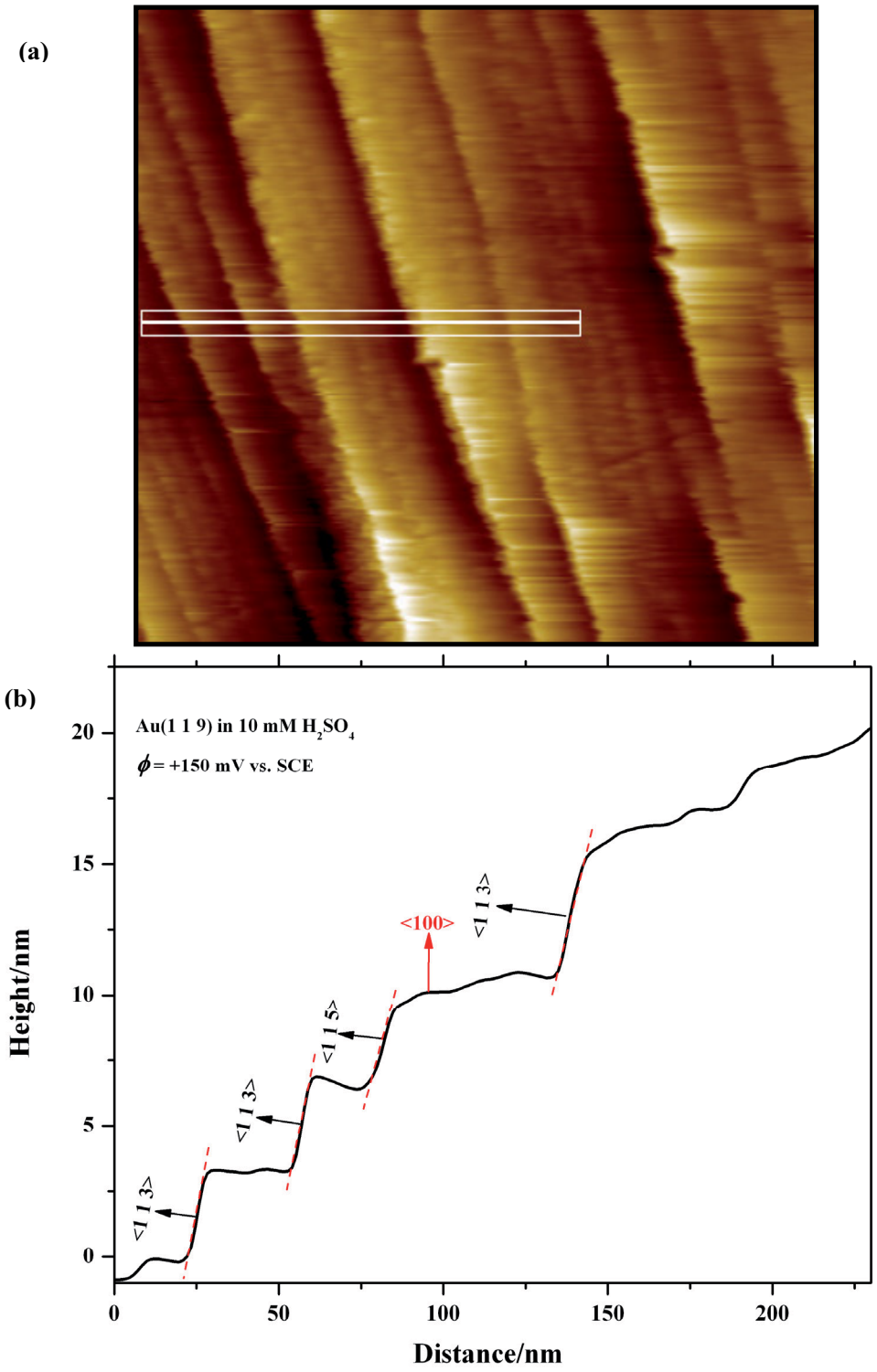

Fig.(4-6): (a) STM image of the Au(1 1 9) electrode in 10 mM H_2SO_4 at room temperature and ϕ = +150 mV vs. SCE. The area is 334x334 nm^2. (b) The average height profile of the area marked by three scan lines in (a).

Comparing the three histograms at the three different potentials, one sees that the probability to find flat areas ($\tan\theta \approx 0$) slightly increases with increasing potential.

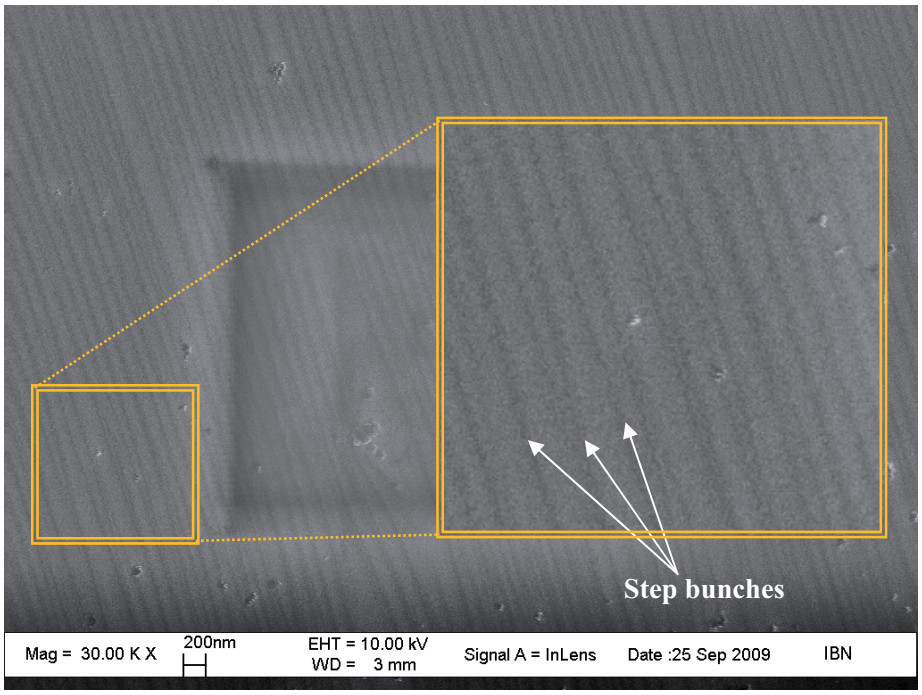

Fig.(4-7): Scanning electron microscope (SEM) image of Au(1 1 9) after flame annealing. The image was recorded under vacuum conditions (2.5 x 10^{-3} mbar). The agglomerations on the surface are contaminations, which might aggregate on the surface during flame annealing or during the transfer of the sample into the vacuum chamber.

Since the STM data seemes not to represent the surface average, a large crystal area was analyzed employing electron microscopy. For this purpose, the Au samples were prepared by flame annealing as before, however, without immersing them into electrolyte. Then the samples were put into the electron microscope (**Zeiss- DSM 962 Electron Microscope**). An example of a SEM image is shown in figure (4-7). The sample surface reveals an almost regular array of steep and flat areas. The enlarged image shown in the figure inset reveals broad parallel stripes which correspond to the step bunches. From this observation, it can be concluded that first, the step bunches are formed mainly during flame annealing and secondly, the entire electrode surface is restructured into phases of steep and flat surface sections.

4.2.2. Evolution of step bunches with time

In addition to the structural study of the Au(1 1 *n*) surfaces in electrolyte, we have studied the orientation of the individual steep regions as a function of time while the electrode potential was kept constant. The experiments have been performed on Au(1 1 9), Au(1 11) and (1 1 7) in 10 mM H_2SO_4. A surface region was chosen that contained several steep step bunches. To analyze the time evolution of step bunches, the height profile of the surface region was recorded over approximately 17 minutes and the slope of the step bunches was plotted versus time. Due to thermal drift, the total observation time was restricted to a maximum of 20 minutes. The experiments were performed at two electrode potentials: At low potentials where the atom mobility on the surface is low, and at high potential where the surface mobility is high (see chapter 5). Figure (4-8) shows an example of the evolution of step bunches with time on Au(1 1 9) in 10 mM H_2SO_4 at -70 mV vs. SCE: (a) displays the corresponding STM image. The marked area is the area where the height profile was monitored, (b) shows the slope of the respective surface area marked in (a) versus time. The surface slope is constant within ~15 minutes, and the measured orientation is close to a (1 1 7) plane.
Figure (4-9) shows two results for +650 mV vs. SCE. There, the inspected surface regions are denoted as A and B. The corresponding surface slopes are plotted over a time range of ~ 20 minutes as squares and circles, respectively. In A as well as in B the surface slopes remain constant over time and the slopes correspond to (1 1 11) and (1 1 13) orientations.

In total we have studied the stability of a large number of surface areas with step bunches on Au(1 1 7) and (1 1 11) electrodes over time at constant electrode potential. In all the data the slopes of the step bunches remain constant within the experimental observation time. The preferred slopes correspond to (1 1 5) and (1 1 7) orientations. One should emphasize though that the orientation of the bunch fluctuates with time (figure (4-8) and figure (4-9)). A further example for these fluctuations is shown in figure (4-10). Here, a series of six consequent STM images on Au(1 1 9) in 10 mM H_2SO_4 at +30 mV vs. SCE is displayed. Two adjacent step bunches separated by a terrace are marked by A, B, and T respectively. An individual, slightly separated monatomic high step is indicated by a red arrow in image (3). The monatomic high step demerges from the step bunch B and fluctuates rapidly (4, 5). In (6), the step has merged with the step bunch again. This observation clearly demonstrated that mass transport is massive

on the electrode surface on the experimental time scale, however, the slopes of the step bunches remain unchanged.

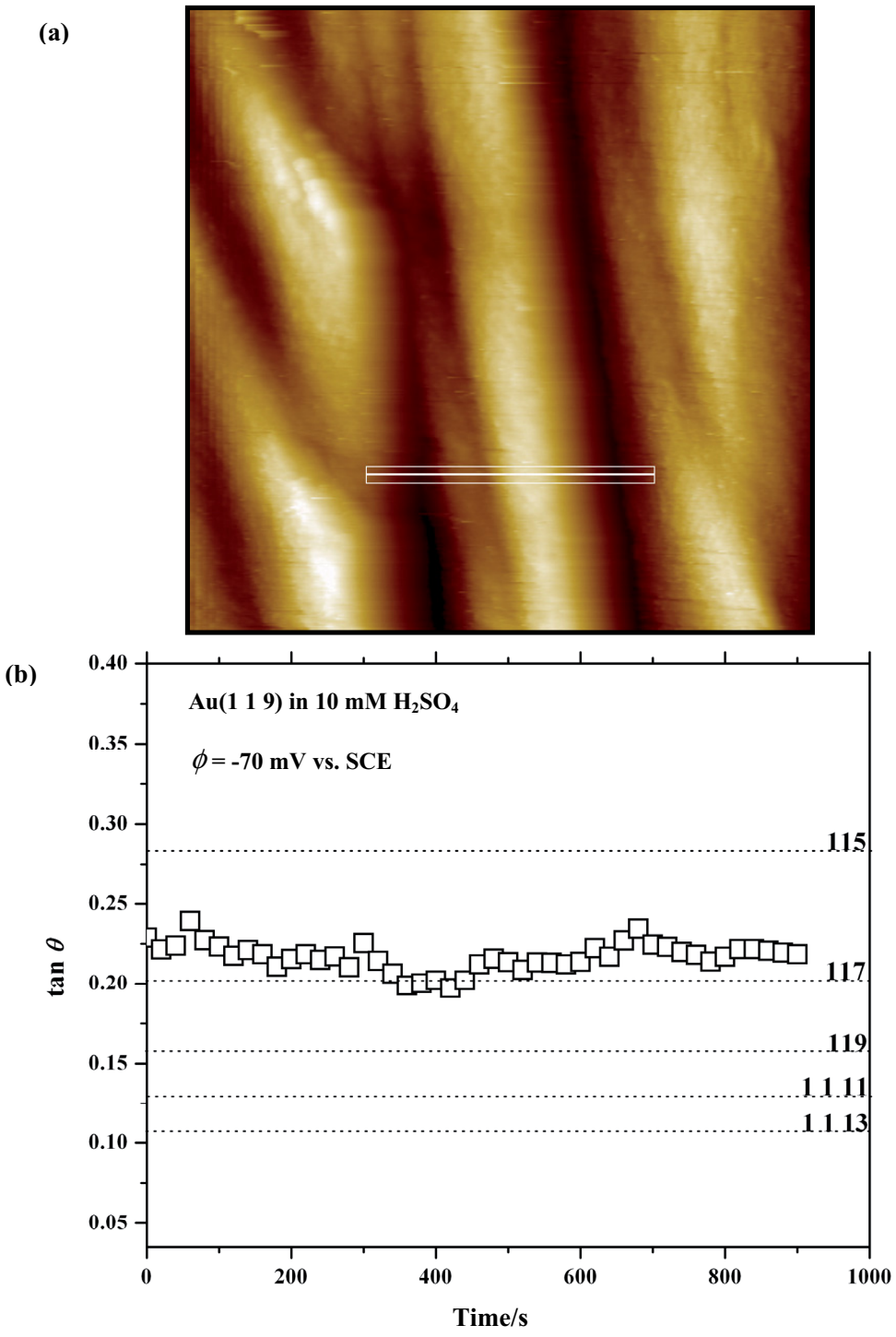

Fig.(4-8): (a) STM image of Au(1 1 9) in 10 mM H_2SO_4 at -70 mV vs. SCE and room temperature. The displayed area is 500x500 nm^2. (b) The slope of the surface area marked in (a) as a function of time

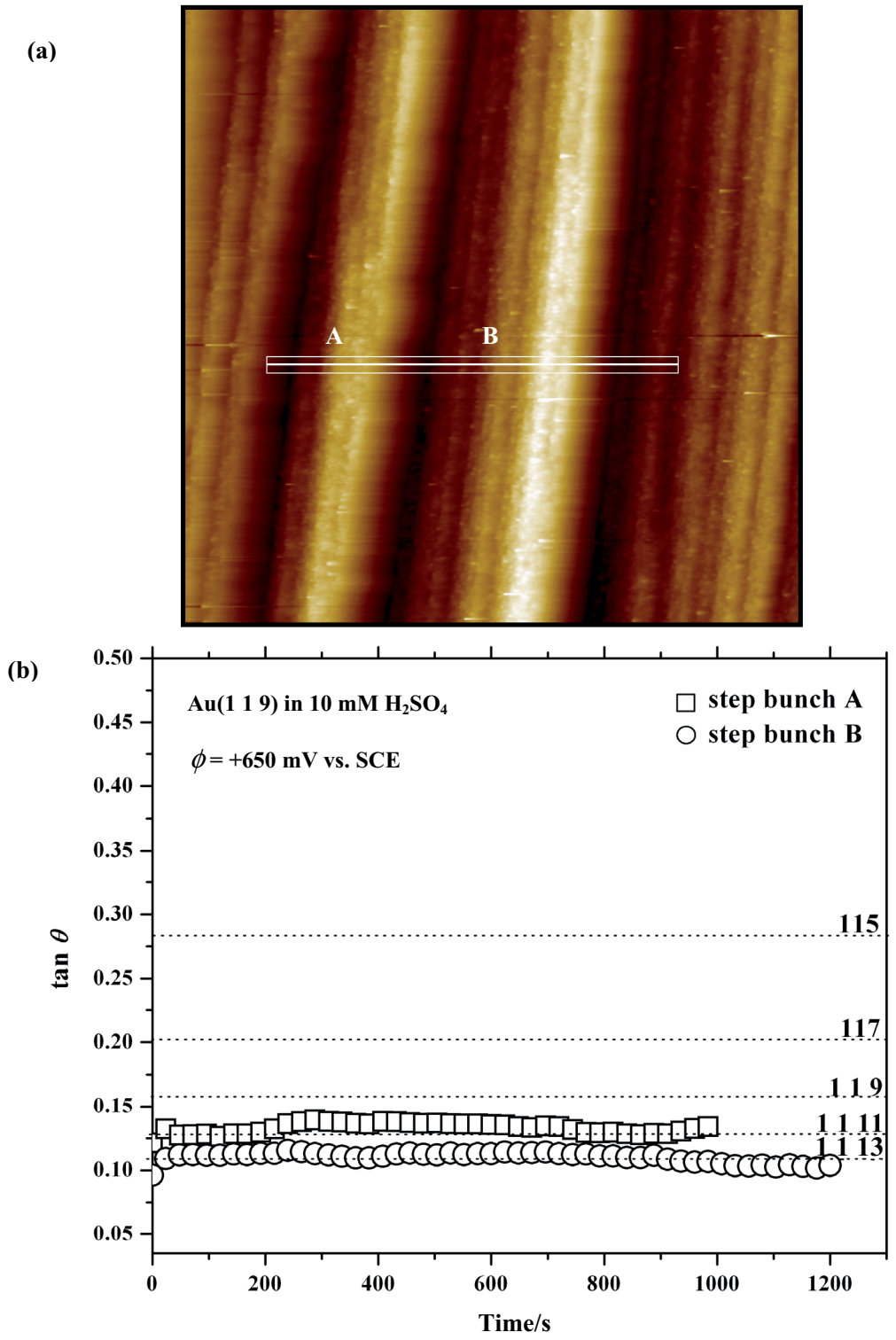

Fig(4-9): (a) STM image of Au(1 1 9) in 10 mM H_2SO_4 at +650 mV vs. SCE and room temperature. The displayed area is 294x294 nm^2. (b) Slopes of the steep regions A and B vs. time.

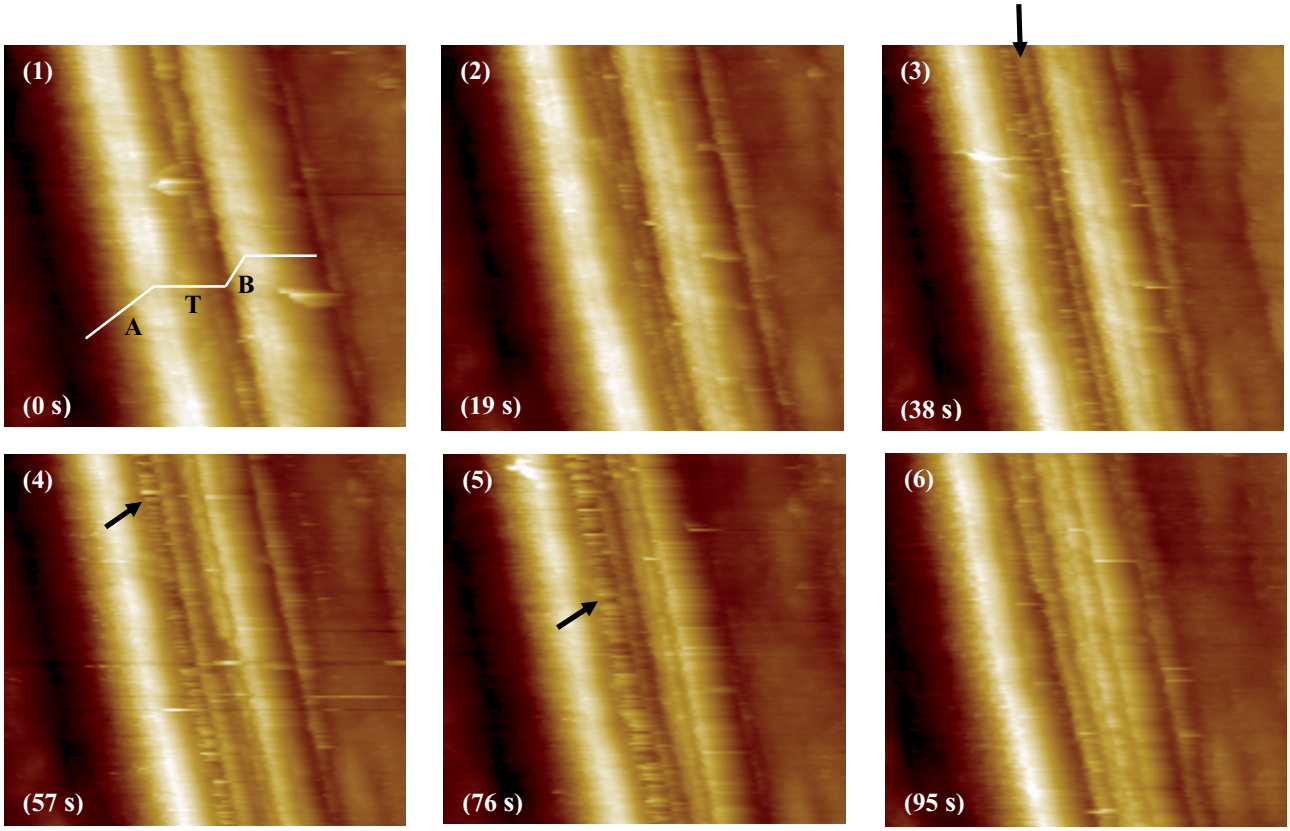

Fig.(4-10): Series of STM images of the same area on Au(1 1 9) in 10 mM H_2SO_4 at +30 mV vs. SCE at different times. The denoted times indicate the starting time of the image with respect to image (1). Displayed area is 177x177 nm^2.

4.2.3. Evolution of local area with potential

Since the surface orientation is conserved over time, we can now look at the influence of the electrode potential on the local surface morphology. For this purpose we changed the electrode potential and monitored simultaneously the surface evolution of one particular surface area.

Figure (4-11) shows STM images of a surface area on Au(1 1 9) in 10 mM H_2SO_4 at different electrode potentials +30, +130 and +230 mV vs. SCE. The height profile for each STM image is analyzed, and the corresponding Miller index *n* of the measured local surface plane (1 1 *n*) has been calculated from the average slope for each height profile. As we see from the STM images, the overall orientation changes with increasing electrode potential. The overall orientation of the local area in image (1) corresponds to (1 1 23) at +30 mV, and to (1 1 27) at +230 mV in image (3).

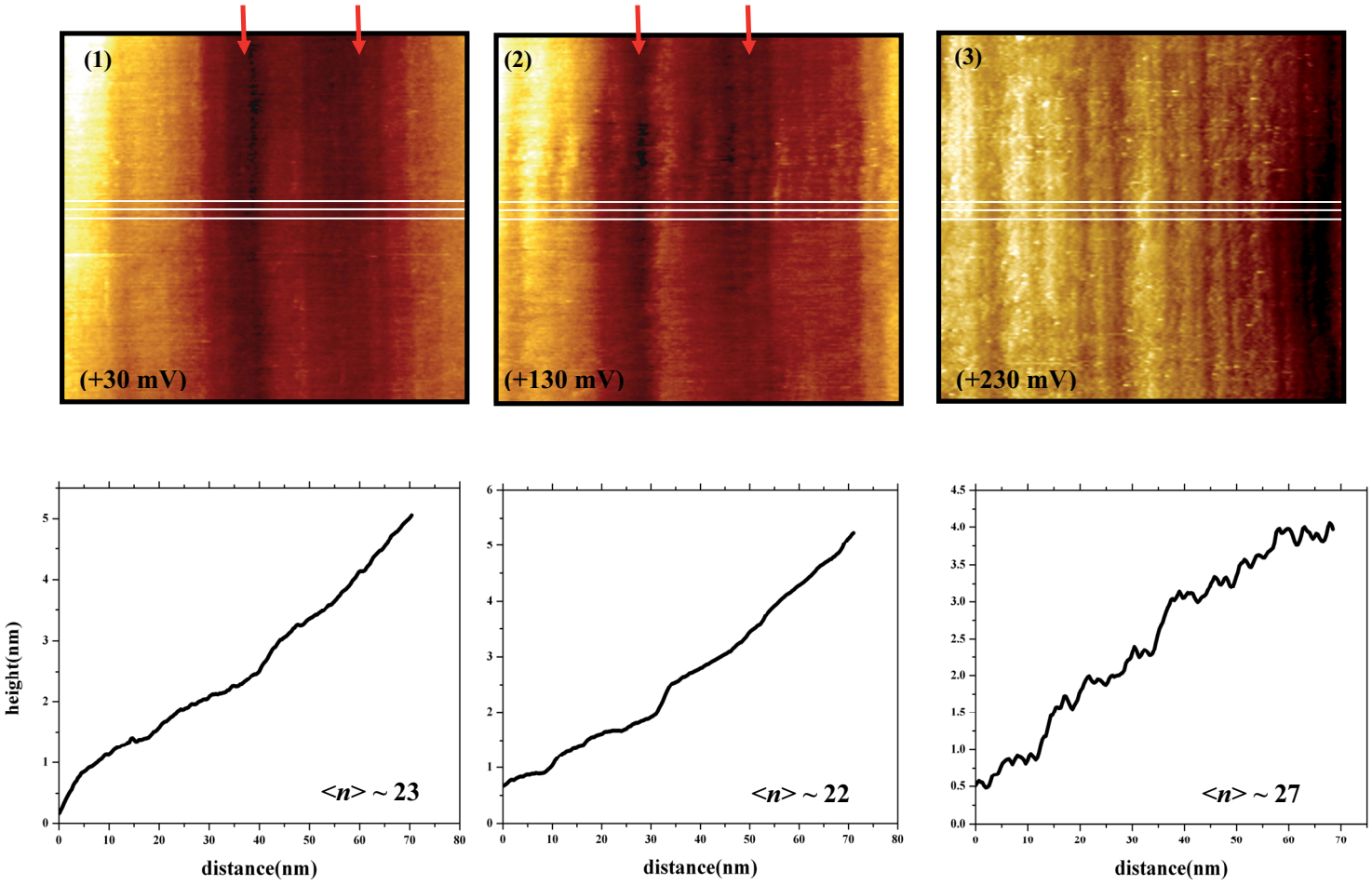

Fig.(4-11): Up: STM images of the same area on Au(1 1 9) in 10 mM H_2SO_4 at different electrode potentials. The black arrows in (1) and (2) indicate steep step bunches. The displayed area is 71x71 nm^2. **Bottom**: The average height profile of the area marked in (1),(2) and (3).

4.3. Reconstruction of Au(1 1 *n*) in electrolyte

As briefly mentioned in chapter 2, surface atoms are often located at lattice positions that differ from those in the bulk due to unsaturated bonds. The driving force for the surface atoms to assume new positions is the reduction of surface energy. Such a rearrangement of the surface atoms is called surface reconstruction. Surface reconstructions are well studied for the low-index faces of Au [66,67,68,69] under vacuum conditions as well as in electrolyte [70,71,72]. The Au(100) surface reconstructs into a quasi-hexagonal close packed (5x20)-structure when flame annealed. The uppermost reconstructed layer is slightly rotated by about 0.81° with respect to the underlying (100) plane, and the atom density is increased by 25% compared to the (1x1) (100) layer [17].

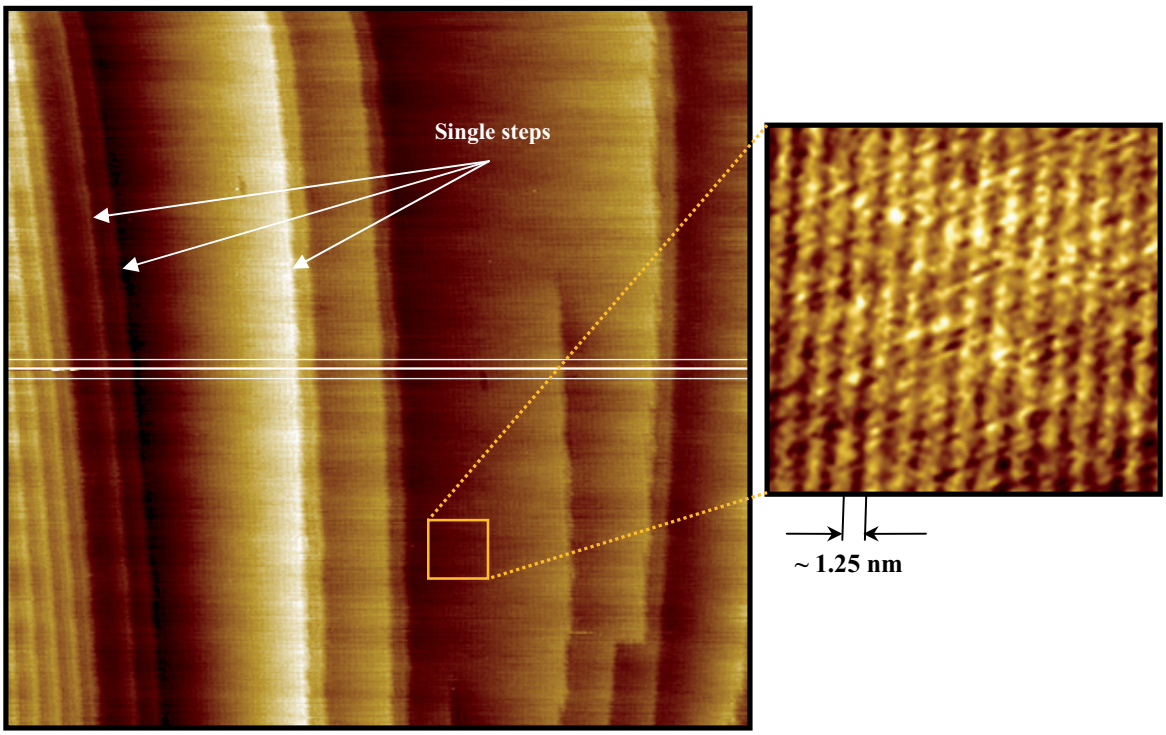

Fig.(4-12): STM image of Au(1 1 29) in 100 mM $HClO_4$ + 1 mM HCl at ϕ = -170 mV vs. SCE and room temperature. Displayed area is 166x166 nm^2. Examples of single steps are indicated by arrows. The enlarged area shows the reconstruction lines on the terrace.

Hence, the reconstructed surface appears slightly buckled with a certain corrugation length denoted as "reconstruction lines" [71,17]. Figure (4-12) shows a STM image of Au(1 1 29) in 100 mM $HClO_4$ + 1 mM HCl at ϕ = -170 mV vs. SCE. The enlarged area shows the reconstruction lines. The reconstruction lines are oriented parallel to the step edges, with a mean corrugation periodicity of 1.25 nm. In electrolyte, the reconstruction is lifted when the electrode potential is increased beyond the potential of zero charge [71]. When the reconstruction is lifted, the extra atoms are expelled from the reconstructed rows and nucleate as monatomic high islands on top of the unreconstructed surface layer. The kinetics of the lifting of the reconstruction depends on the width of the reconstructed (100) terraces. Surfaces prepared by electropolishing have larger terraces than surfaces prepared by flame annealing. Therefore, the lifting of the reconstruction is faster on flame annealed surfaces and takes less than a second [74]. The surface reconstruction leads to a sharp peak at about +100 mV vs. SCE in the cyclic voltammogram. In a voltammogram the potential of the working electrode is cycled with respect to the reference

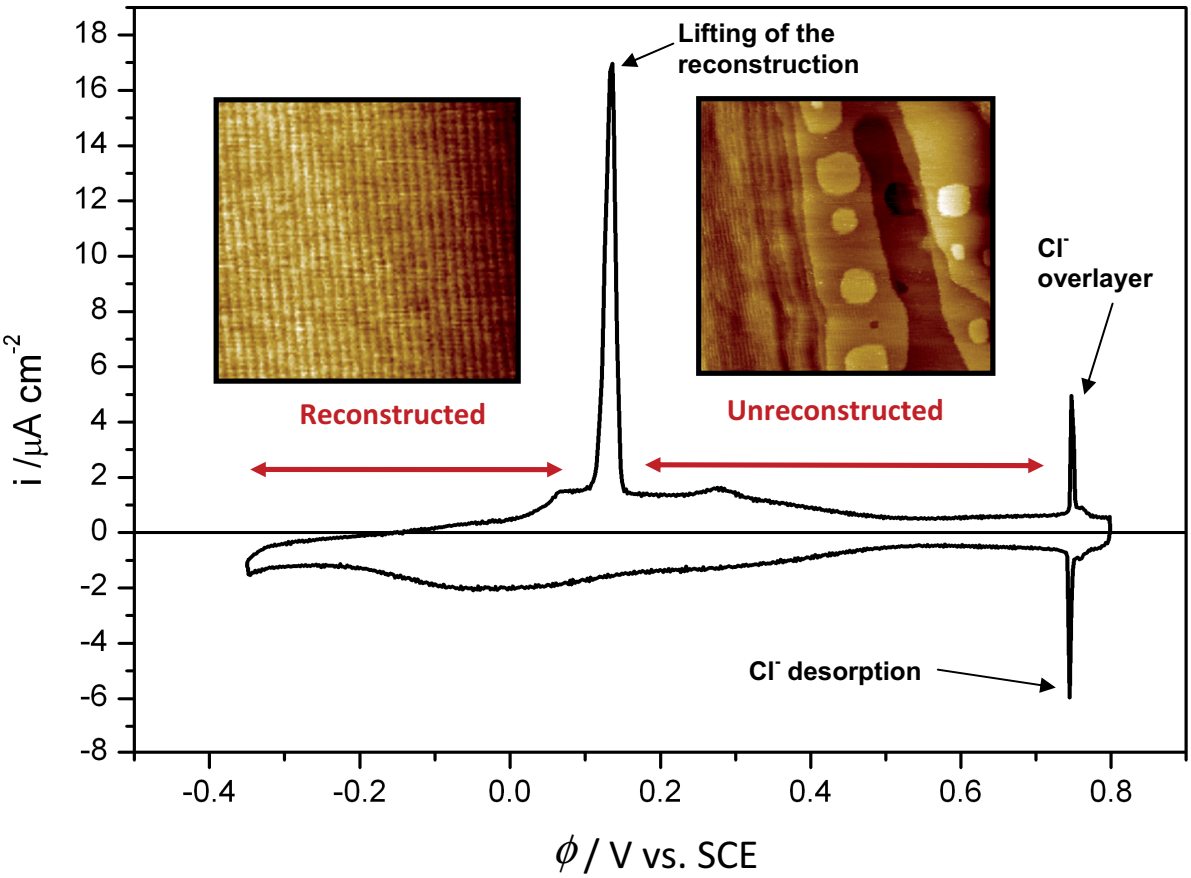

Fig.(4-13): Cyclic voltammogram of Au(100) in 9 mM $HClO_4$ +1 mM HCl. Scan rate 10 m V/s.(courtesy of G. Beltramo). The STM images show the surface morphology on Au(1 1 29) in 100 mM $HClO_4$ + 1 mM HCl in the reconstructed (displayed area 39x39 nm^2) and the unreconstructed (displayed area 167x167 nm^2) regimes. In fact, the general shape of the voltammogram of Au(100) in 9 mM $HClO_4$ +1 mM HCl is almost similar to the voltammogram of Au(1 1 29) in 100 mM $HClO_4$ + 1 mM HCl, the only difference is that in the latter case the lifting of the reconstruction peak is shifted by ~10 mV towards negative potentials.

electrode at constant rate between potentials corresponding to hydrogen evolution and oxidation. The recorded current is then plotted versus the potential [80]. Current density peaks may arise due to the charging and discharging of the electrode-liquid interface. Changes in the interface charge when ions adsorb or desorb at the surface at a specific electrode potential or if the surface is restricted as in surface reconstruction phenomena. The current density i can be expressed in terms of the interfacial capacity C (chapter 2) [10]

$$i = C\frac{\mathrm{d}\phi}{\mathrm{d}t} \tag{4-1}$$

Here, $\frac{d\phi}{dt}$ is the scan rate. Figure (4-13) shows a voltammogram of Au(100) in 9 mM $HClO_4$ + 1 mM HCl with the associated STM images of the reconstructed and unreconstructed phase. (The voltammograms in this thesis were measured by G. Beltramo). The peak around 0.13 V corresponds to the lifting of the reconstruction. When the potential is increased to more positive values, additional peaks appear indicating the adsorption of Cl^-.
Stepped electrode surfaces Au(1 1 7), Au(1 1 9) and Au(1 1 11) show a phase separation into steep regions (step bunches) and areas almost free of steps. Those vicinal surfaces are also reconstructed at ϕ= -170 mV vs. SCE. The reconstruction, however, occurs exclusively in surface areas where larger terraces prevail. Areas with step bunches are free of any surface reconstruction [46].

Figure (4-14)-(a) shows a STM image of the reconstructed Au(1 1 11) electrode in 10 mM H_2SO_4 at ϕ= -170 mV vs. SCE. Au(1 1 11) has parallel steps. Two examples are indicated by arrows in figure (4-14). The steps are separated by (100)-oriented, reconstructed terraces. The reconstruction lines are aligned along the step edges. Figure (4-14)-(b) shows the height profile of the area marked in (a). We find a mean distance between the reconstruction lines of *d*= of 1.9 ± 0.1 nm. This value differs significantly from the value 1.44 nm as found for flat Au(100) [66,73] and also from the value 1.25 nm as found for Au(1 1 29) (Figure (4-12)). A shift in the reconstruction periodicity for stepped Au surfaces should be observable in electrochemical measurements such as voltammetry and capacitance curves.

Figure (4-15)-(a) shows the voltammograms of Au(100) and Au(11*n*) (*n*=5,7,11,17) surfaces in 5 mM H_2SO_4. For Au(1 1 *n*) surfaces the reconstruction peak as found for Au(100) around +370 mV is replaced by a complex peak structure. For example, the sharp transition peak of Au(100) has a shoulder around +250 to +300 mV which develops into a pronounced peak around +280 mV for the Au(1 1 17) surface. In addition, the main peak of Au(100) is reduced to a small peak on (1 1 17). Au(1 1 7) and Au(1 1 11) have a pronounced peak around +210 mV and a shoulder around +300 mV where a peak is found for (1 1 17). The Au(1 1 5) surface has merely a relatively broad peak followed by a shoulder around +150 mV. Figure (4-15)-(b) shows the capacity curves of Au(100) and Au(11*n*) (*n*=5,7,11,17) surfaces in 5 mM $HClO_4$.

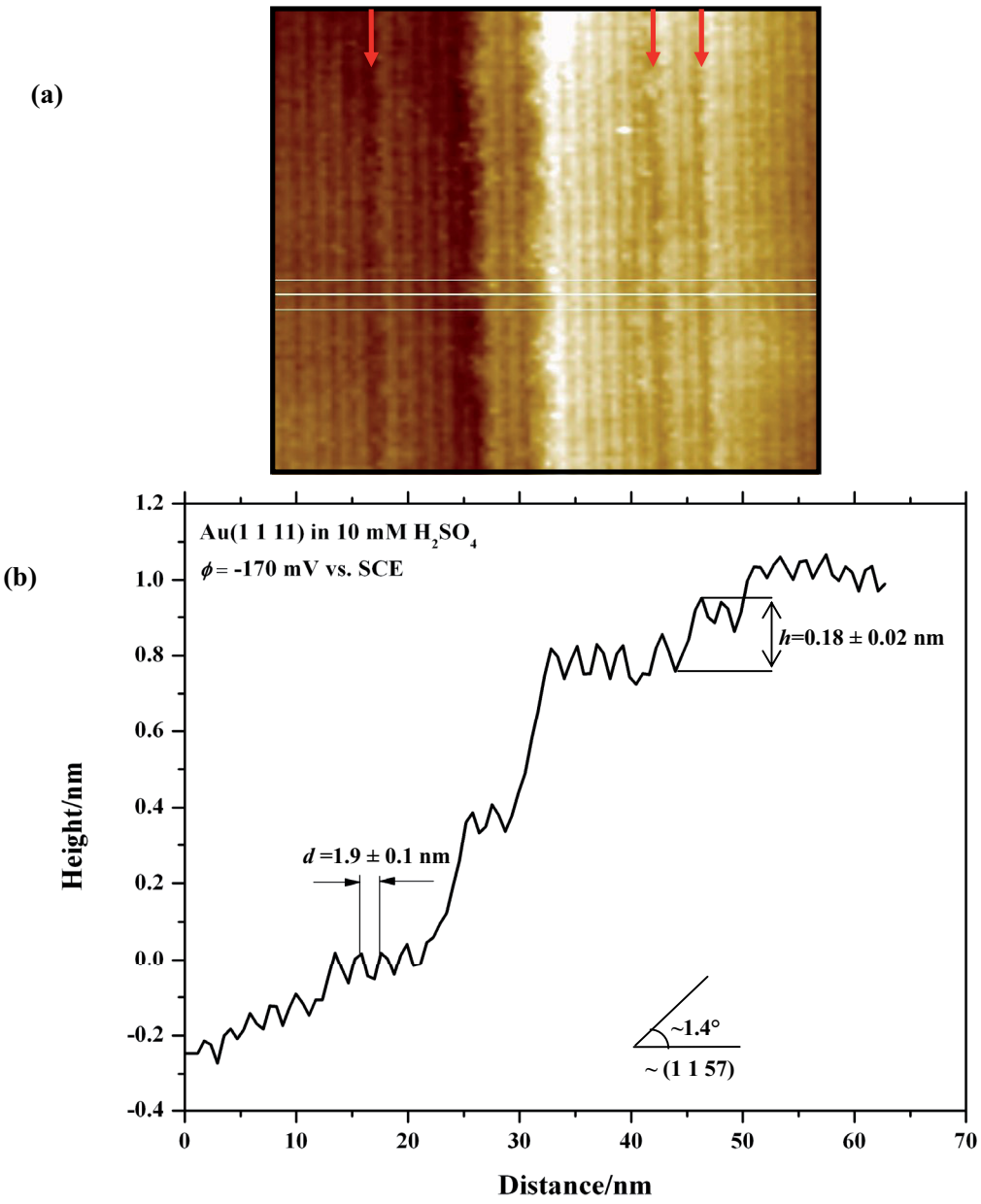

Fig.(4-14): (a) STM image of Au(1 1 11) in 10 mM H_2SO_4 at ϕ = -170 mV vs. SCE. The local terrace width as shown in the image is much broader than the nominal terrace width (8.23 nm rather than 1.6 nm). Displayed area is 67x67 nm^2. (b) The height profile of the area marked by the white lines in (a). The average distance *d* between the reconstruction lines and the average step height *h* are shown in (b).

(a)

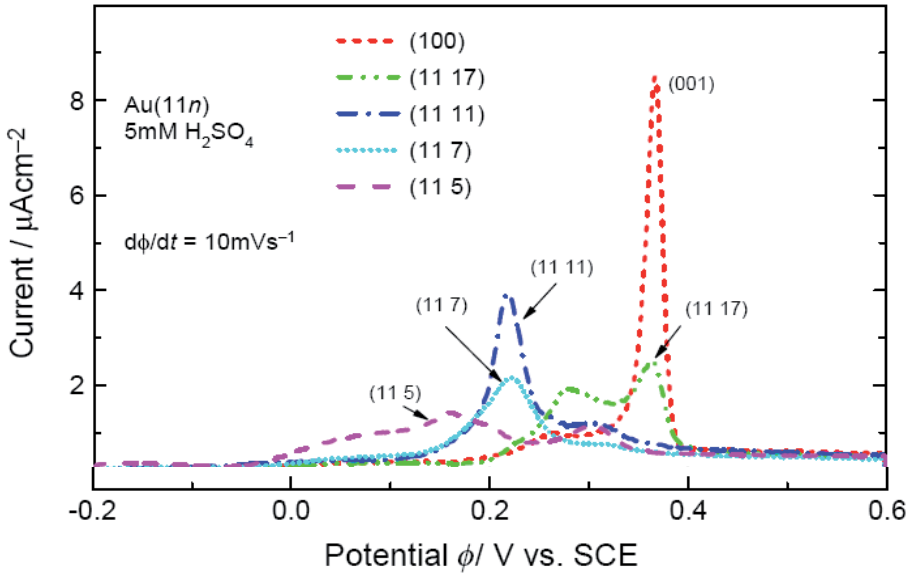

(b)

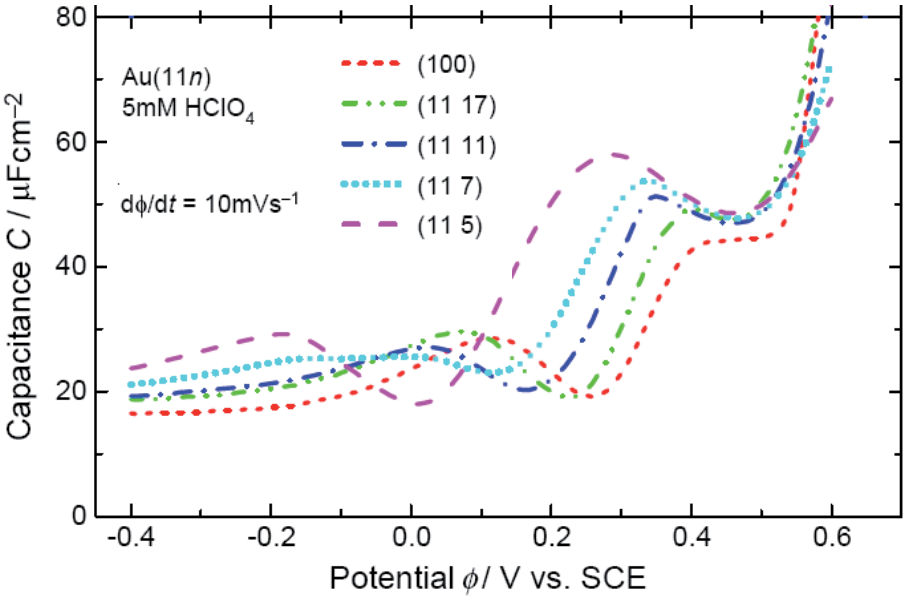

Fig.(4-15): Voltammograms of Au(100) and Au(11*n*) (*n* = 5,7,11 and 17) in 5 mM H_2SO_4 taken during a positive potential sweep starting from -0.35 V vs. SCE immediately after immersing the samples into the electrolyte at -0.35 V vs. SCE so that the surface is reconstructed. (b) Capacitance measured during the positive potential sweep of Au(100) and Au(11*n*) (*n* = 5,7,11 and 17) in 5mM $HClO_4$ starting from the immersion potential of -0.4 V [46] .

The capacitance curves are recorded during the positive potential sweep starting from the immersion potential of -400 mV [46]. For homogenous surfaces the minimum of the measured capacitance corresponds to the pzc. It has been reported that the pzc shifts towards negative potentials with increasing step density due to the dipole moment associated with steps [26]. In figure (4-15)-(b) a strong systematic shift of the minimum in the capacitance curve is found. From this shift we find the pzc for Au(1 1 5), (1 1 7), (1 1 11), (1 1 17) and (100) to be +9 mV, +115 mV, +164 mV, +226 mV and +257 mV vs. SCE, respectively [26,46].

4.4. Discussion

In our studies of the step bunching on stepped Au(1 1 *n*) surfaces, we never observed extended (111) facet (see figures (4-2), (4-3), (4-4)). This observation is consistent with an earlier study of our group on Ag(19 19 17) [60]. However, we cannot exclude small local (111) microfacets consisting of two or three steps. This may be due to limited tip resolution: The overall aperture of the tip end is larger than the average distance between the steps. For example, 1 nm is the average distance between the steps on (1 1 7), the typical radius of the tip aperture is ~ 25 nm [91]. The limited tip resolution might also cause the almost smooth appearance of the regions in the height profile.

The surface morphology of stepped Au(100) surfaces has been previously studied by Watson et al [61]. The authors studied Au surfaces inclined by ~ 1.7° with respect to the (100) plane between room temperature and bulk melting temperature. At 992 K they found a favorable plane orientation (magic vicinal) close to tan θ ~ 0.035, which corresponds to a (1 1 35) plane. The almost flat regions as observed in the analysis in this thesis have comparable orientation. We observe phase separation into (1 1 33) and (1 1 5) planes on Au(1 1 9) in electrolyte. Furthermore, Sotto and Boulliard [62] found that (1 1 11) and (1 1 3) faces are stable, and they observed that (1 1 9) and (1 1 7) surfaces in vacuum separate into (1 1 5) and (100) facets. In this thesis, a systematic study of the morphology on Au(1 1 9) is performed. As become obvious from figure (4-5), the surface morphology exhibits a wide distribution of local orientations rather than a distinct favorable local orientation such as proposed by Bartolini et al [75] and by Sotto and Boulliard [62]. We attribute the wide distribution of local surface orientations to the

presence of the surface reconstruction: The Au(1 1 *n*) surfaces tend to minimize the surface energy by forming a surface reconstruction. The reconstruction on the other hand requires a minimum terrace width. Phase separation into large terrace areas and step bunches supports the formation of a surface reconstruction in large areas with simultaneously conserving the net orientation of the vicinal plane. Therefore, the driving force for the step bunching instability on Au(1 1 *n*) surfaces may be the reduction of surface energy via formation of large areas of surface reconstruction. Thereby the total energy gained by a phase separation into step bunches and large, reconstructed terraces may also overcome the short-rage repulsive step-step interactions on vicinal Au(1 1 *n*) surfaces in electrolyte.

In this thesis we found that a reconstruction similar to that on Au(100) is established. The reconstruction periodicity however, is enlarged, as shown in figure (4-14). The enlargement in the reconstruction periodicity was also observed in the work of M. Moiseeva et al [17]. The authors found a mean distance between the reconstruction lines $d = 1.8 \pm 0.14$ nm for Au(1 1 17) in electrolyte, and $d = 1.96 \pm 0.14$ nm for Au(1 1 11) in vacuum. Furthermore, they found a reconstruction-free zone at the step edges which is consistent with previous study of Binnig et al [66]. Watson et al [61] have found an enlargement of the reconstruction periodicity by 12% (d =1.6 nm) on terraces with ~2° inclination angle. However, this enlargement is smaller compared to what is found in his thesis and by M. Moiseeva et al [17].
The enlargement in the reconstruction periodicity is also observed on Au(1 1 1) [92]. These authors have shown that the compressive strain enlarges the reconstruction unit cell. In our study, the reconstruction is observed on surface areas located between areas of high step density (step bunches). It is well known that the atoms at the steps are relaxed to new positions [75]. The displacements of the step atoms give rise to stress field near the steps. For an isolated step, the displacement vectors on each side of the step have opposite sign and have about the same value. Within a step bunch, the displacement vectors at each side of the individual steps in the bunch have also opposite sign and vectors of adjacent steps largely compensate each other, leaving the last displacement vector at the end of the step bunch uncompensated. Therefore, the stress field resulting from the displacement of the step atoms at the end of the step bunch is larger than that originated from the isolated step. Using a semi-theoretical approach it could be shown that the enlarged reconstruction unit cell might in fact originate from stress fields at the step bunches adjacent to a large, reconstructed terrace [17].

A surprising result of this study is that although a massive mass transport is present, the orientation of the step bunches at constant electrode potential remains stable. This is indicative that the phase separation into steep step bunches and areas almost free of steps is an equilibrium morphology of flame annealed stepped Au(100) electrodes. A similar result was found previously for Ag(19 19 17) in electrolyte [60]. Ag(19 19 17) is unstable against phase separation and double-steps and steps of multiple height are formed. From that one might conclude that in electrolyte an instability of stepped metal electrodes against step bunching might be a quite general phenomena.

In this thesis an influence of the electrode potential on the terrace width distribution is observed. This observation is consistent with a previous study by our group [16], where the terrace width distribution on Au(1 1 17) in 10 mM H_2SO_4 at different electrode potentials was analyzed. The authors found that around pzc the terrace width distribution is very narrow, whereas at potentials below and above pzc the distribution broadens. However, since this broadening was analyzed merely at one particular surface area, the authors could not directly deduce a general phenomenon typical for the entire surface. The observations in this thesis, however, seem to corroborate the influence of the electrode potential on the terrace width distribution. In reference [29], our group developed a theoretical approach to explain the potential dependence of the terrace width distribution. The approach is based on the calculation of the surface tension of stepped surfaces with elastic step-step repulsions included. Two cases are considered: Case I describes the ideal vicinal surface with a regular step array. Case II describes the surface with one large step bunch covering a fraction x of the surface, leaving a fraction 1-x free of steps (figure (4-16)). The difference $\Delta\gamma$ in the surface tensions (i.e. the energy gain in surface energy due to the phase separation) for the cases I and II to the lowest relevant order in tan θ is given by [29]

$$\Delta\gamma = \underbrace{-C\tan^2\theta\left(\frac{p_z^2}{2\varepsilon_\circ^2 a_\parallel^2 h^2}+\frac{1}{4}\left(\phi-\phi_{pzc}\right)^2\right)}_{\mathbf{C_1}}\left(\frac{1}{x}-1\right)+\underbrace{\frac{\pi^2 A\tan^3\theta}{3h^3}}_{\mathbf{C_2}}\left(\frac{1}{x^2}-1\right)+\ldots \qquad (4\text{-}2)$$

Here, A is the step-step interaction constant [14]. The first term C_1 in equation (4-2) is an effective attractive term which is always negative. It depends on the step dipole moment p_z and

The shift of the potential ϕ relative to pzc, ϕ_{pzc}. Since this term is always attractive, the shift in pzc of a vicinal surface (1 1 *n*) with respect to the low-index (100) plane and the associated step dipole moment may be enough to overcome the short-range repulsive step-step interactions. The second term C_2 covers the contribution of energetic or elastic step-step interactions and may be of repulsive or attractive nature.

Figure (4-17) shows the calculation of the difference between surface tensions of a Au(1 1 9) surface in 10 mM H_2SO_4 with a regular array of steps and a surface with step bunches according to equation (4-2) at different electrode potentials. For this calculation experimentally realistic data for the interfacial capacitance *C,* the pzc and the step dipole moment p_z were used [93].

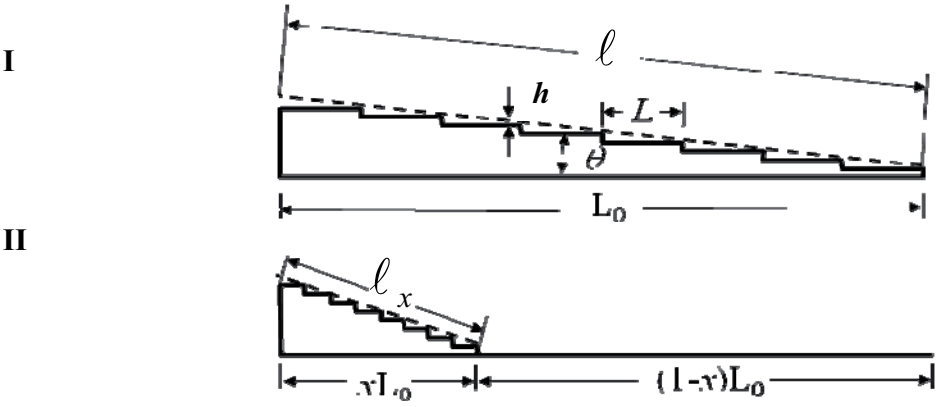

Fig.(4-16): Graphical illustration of the two limiting cases described in [29]: Case I- surface with regular array of steps. Case II- surface with a step bunch covering a fraction x of the surface.

No experimental data for the interaction constant *A* exists for Au(100) in electrolyte. Therefore, a value of 10 meVÅ comparable to experimental data for *A* on various metal surfaces in vacuum was used.

At pzc, $\Delta\gamma$ (equation (4-2)) is positive for all values of *x*. Increasing the deviation $\Delta = \left|\phi - \phi_{pzc}\right|$ of the potential from pzc, $\Delta\gamma$ becomes negative. The energy gain increases with increasing Δ and decreasing *x*. Until a minimum value of *x* is reached and $\Delta\gamma$ becomes positive again.

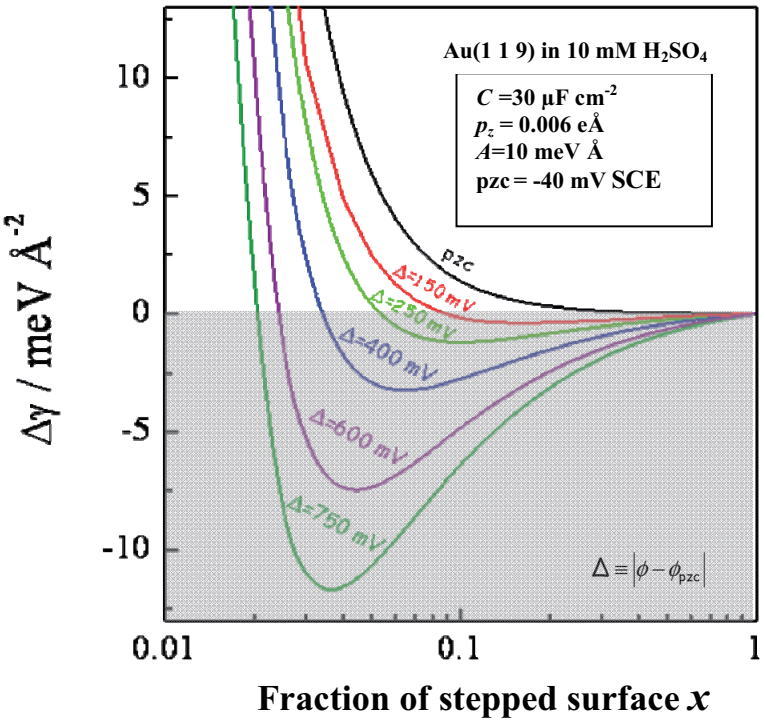

Fig.(4-17): The calculated gain in surface tension according to equation (4-2) for the Au(1 1 9) vicinal surface in 10 mM H_2SO_4 when the surface fraction x is covered by step bunches. (courtesy of M. Giesen) [16, 94].

Equation (4-2) describes a simple theoretical approach to understand the phase separation of stepped Au(100) surfaces. It does not consider, for instance, the energetic contribution of the surface reconstruction. The continuous shift of the pzc towards negative values as found in figure (4-15)-(b), and the peak structure in the voltammograms in figure (4-15)-(a), however, show that the surfaces Au(1 1 n) with n < 17 are at least partially reconstructed. The shift of the reconstruction peaks in the voltammograms in figure (4-15)-(a) indicate that the formation/lifting of the reconstruction is associated with an energy term different from that for nominal flat Au(100). The reconstruction peaks shift toward more negative values with increasing step density. That is, the energy gain forming the surface reconstruction on Au(1 1 n) is smaller than forming the reconstruction on Au(100), the energy gain for Au(1 1 n) decreases with decreasing Miller index n . The fact that the peak structure for the reconstruction peak for Au(1 1 n) is more complex than just a mere peak shift (e.g. the existence of double peaks for Au(1 1 17) and Au(1 1 11)) indicates that the unit cell of the reconstruction varies with the terrace width. This is corroborated by the observation of different distances d between

reconstruction lines. Table (4-1) shows a summary of the measured *d* for Au(100) and Au(1 1 *n*) surfaces as found in this thesis and in the literature.

Table (4-1): A summary of the measured *d* of Au (100) and Au(1 1 *n*) surfaces

	Au(100)	**Au(1 1 41)**	**Au(1 1 29)**	**Au(1 1 17)**	**Au(1 1 11)**	**Au(1 1 9)**
***d*/nm**	1.4 [73]	1.6 [61]	1.25 [this thesis]	1.8±0.14[17]	1.9±0.1 [this thesis] 1.96±0.14[17]	1.8±0.1 [17] 1.91±0.14 [this thesis]

A possible explanation for the different reconstruction unit cells for different Miller indices *n* could be that the unit cell is adjusted such that an integer number of unit cells fit into the mean terrace width. The phase separation observed on Au(1 1 *n*) in electrolyte leads then to the conclusion that different types of reconstruction unit cells must exist locally on the Au(1 1 *n*) surfaces, depending on the local surface orientation. In fact in a recent study by our group it is reported that three kinds of reconstruction exist on Au(1 1 *n*) : The first one can be identified as the reconstruction which is established on extended flat (100) terraces, with a reconstruction periodicity $d \sim 1.4$ nm. The second type is the reconstruction which is established on terraces between areas with high step density (step bunches), with a reconstruction periodicity $d \sim 1.9$ nm. The last type of reconstruction is associated with stepped areas where the step-step distance is too small (e.g. in the area within step bunch) to accommodate the known "quasi-hex" reconstruction [46].

Chapter 5

Step fluctuations on Au(1 1 17) and Au(1 1 29) in electrolyte

As demonstrated in chapter 4, steps on Au(1 1 *n*) surfaces undergo considerable step fluctuations that cause temporal merging and demerging of steps with/from step bunches. In this chapter, a quantitative analysis of the time and spatial dependence of step fluctuations on vicinal Au(100) surfaces in electrolyte is performed in order to detailly understand the mass transport processes involved in the fluctuations. The studies were performed on Au(1 1 17) in 100 mM $HClO_4$+ 1 mM HCl and on Au(1 1 29) in 100 mM $HClO_4$+1 mM KBr. Previous studies [14, 95] focused on metal electrodes in SO_4^{2-}- and Cl^- -containing electrolytes. In this thesis, the studies were performed in Cl^- and Br^- -containing electrolytes to compare different halide anions and their influence on surface mass transport on Au(100) vicinal surfaces.

5.1. Introduction to halide adlayers

Specifically adsorbed halides, e.g. Cl^- and Br^- anions on metal electrodes such as gold and copper were intensively studied using EC- STM [79,80,81]. In the case of chloride on Au(100), an uniaxially incommensurate superstructure of chloride at potentials positive of the peak of the lifting of the reconstruction was observed. The chloride adlayer has a quasi-hexagonal geometry $c(\sqrt{2}\times p)R45^\circ$ structure, where $2\sqrt{2} \geq p \geq 2.3$ [78]. As shown previously in chapter 4 in figure (4-13), the peak in the voltammogram around 0.75 V vs. SCE corresponds to the ordered Cl^- adlayer. In the potential range between 0.134 V vs. SCE and the formation of an ordered Cl^- adlayer, Cl^- is adsorbed, albeit no structured overlayer is formed. It is known though that adsorbed Cl^- may enhance the surface mass transport [38]. For Br^- on Au(100), two ordered quasi-hexagonal superstructures were found, a commensurate $c(2\sqrt{2}\times 2\sqrt{2})R45^\circ$ structure and

an incommensurate $c\left(2\sqrt{2}\times p\right)\mathrm{R45}^{\circ}$ structure, where $2\sqrt{2}\geq p\geq 2.5$ [77]. The value of p in the incommensurate bromide adlayer seems to depend on the electrode potential. Figure (5-1) shows for comparison two voltammograms of Au(100) in Cl^- and Br^- containing electrolytes. The sharp peaks correspond to the ordered halide adlayers .

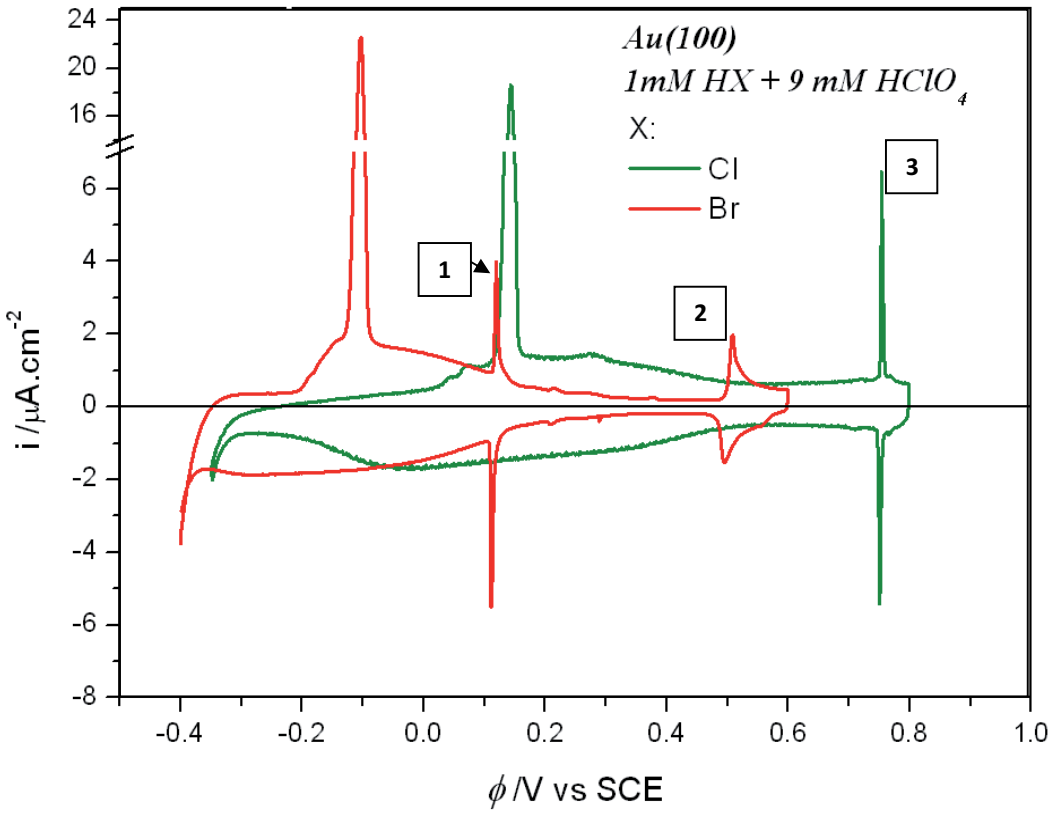

Fig.(5-1): Cyclic voltammograms of Au(100) in 9 mM $HClO_4$ + 1 mM HCl (green) and Au(100) in 9 mM $HClO_4$ + 1 mM HBr (red) .(courtesy of G. Beltramo). The numbers at the peaks correspond to: 1. Ordered bromide $c(2\sqrt{2}\times 2\sqrt{2})\mathrm{R45}^{\circ}$ layer 2. Ordered bromide $c(2\sqrt{2}\times p)\mathrm{R45}^{\circ}$ layer 3. Ordered chloride $c(\sqrt{2}\times p)\mathrm{R45}^{\circ}$ layer.

No experimental data for the influence of Br^- adsorption on the surface mass transport is available. In STM images, the rapid motion of kinks along steps cause a frizzy appearance of the step edges. Kinks move due to the attachment/detachment of adatoms from / to the step edge or

to the terrace (see section 2.3.2.2. case B) [14]. The analysis of equilibrium fluctuations of monatomic high steps on electrodes is a representative measure of the surface mobility. This thesis covers experimental analyses of the step fluctuations on Au(100) vicinal electrodes in Cl^- and Br^- containing electrolytes.

5.2. Time dependence of step fluctuations in the presence of halides

5.2.1. Time dependence of step fluctuations on Au(1 1 17) in chloride containing electrolytes

The measurements were performed on a Au(1 1 17) electrode with a nominal terrace width of 2.45 nm (table 3-1). The surface has been prepared as described in section (3.1). The sample was mounted to the electrochemical cell at ϕ = -200 mV vs. SCE. As electrolyte a 1 mM HCl + 100 $HClO_4$ solution was used. When the sample is mounted under potential control, the surface is reconstructed. In the experiments presented here, data were obtained exclusively if the sample was mounted to the electrochemical cell under potential control.

Step fluctuations were analyzed in the reconstructed and unreconstructed potential regimes of Au(1 1 17). Figure (5-2) shows time images (see section 2.3.2) of Au(1 1 17) at two different electrode potentials (a) +192 mV and (b) +500 mV vs. SCE. In order to determine the time correlation function of the fluctuating steps, the step positions in the STM images were detected using a computer code similar to that used for analyzing the step bunches. This code was established and used in our group to analyze step fluctuations since the early 1990ies [82]. The recorded step positions $x(t)$ were analyzed according to the correlation function

$$G(t,\phi_0) = \frac{1}{2}\left\langle \left(\Delta x(t,\phi_0) - \Delta x(t_0 = 0,\phi_0)\right)^2 \right\rangle \qquad (5\text{-}1)$$

Where t_0 is an individual reference time and ϕ_0 indicates the electrode potential at which the measurement was performed. The difference Δ indicates that the $G(t,\phi_0)$ was determined from a step-pair analysis, where the distance Δx between two adjacent steps at t is correlated to their

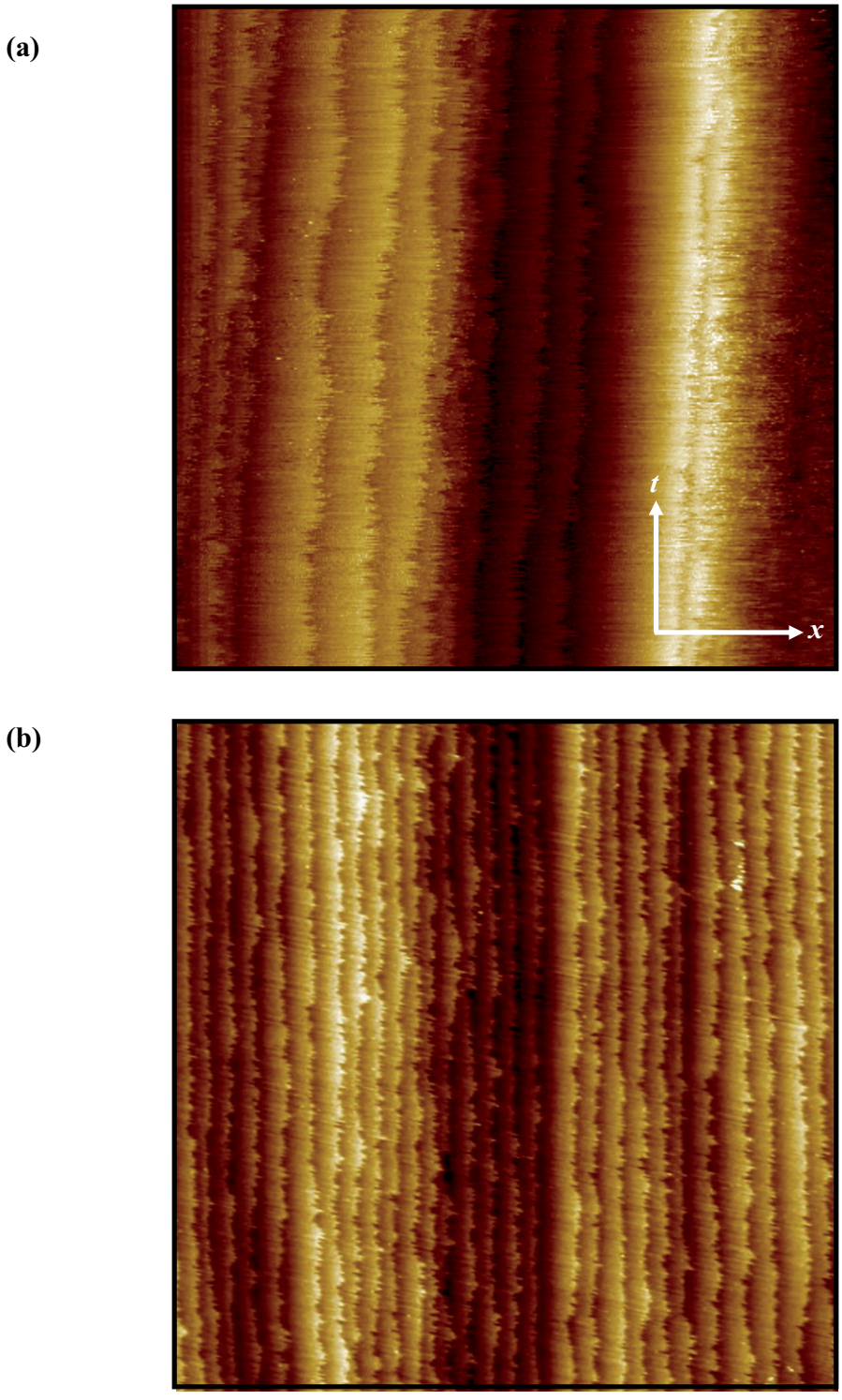

Fig.(5-2): Time images of steps on Au(1 1 17) in 100 mM $HClO_4$ + 1 mM HCl at (a) ϕ = +192 mV vs. SCE (b) ϕ = +500 mV vs. SCE. The scan width is (a) 65.8 nm and (b) 144 nm. The total time displayed on the t-axis (parallel to the steps) is (a) 26 s and (b) 59 s.

distance at $t_0 = 0$ in order to compensate partially for thermal drift. The correlation functions were fitted to a power law according to

$$G(t) = G(t = 0) + c(\phi)t^{\alpha} \tag{5-2}$$

Here, $G(t=0)$ is the correlation value at t=0 and $c(\phi)$ is a potential dependent prefactor (eq. 2-19). We observed in all data for all ϕ a large constant offset $G(t$=0) at t=0. The origin of this offset is not fully understood. It has been observed though also on Ag electrodes [44].

Figure (5-3) shows an example of the analyzed time correlation function at ϕ = -200 mV vs. SCE for Au(1 1 17) in 10 mM $HClO_4$ + 1 mM HCl with a constant offset. Figure (5-4) displays the values of $G(t$=0) versus the electrode potential. As shown in the figure, the values of $G(t$=0) remain almost constant at electrode potentials below +400 mV vs. SCE. Around +450 mV vs. SCE, a sudden increase in $G(t$=0) is observed. For higher potentials, $G(t$=0) decreases abruptly to

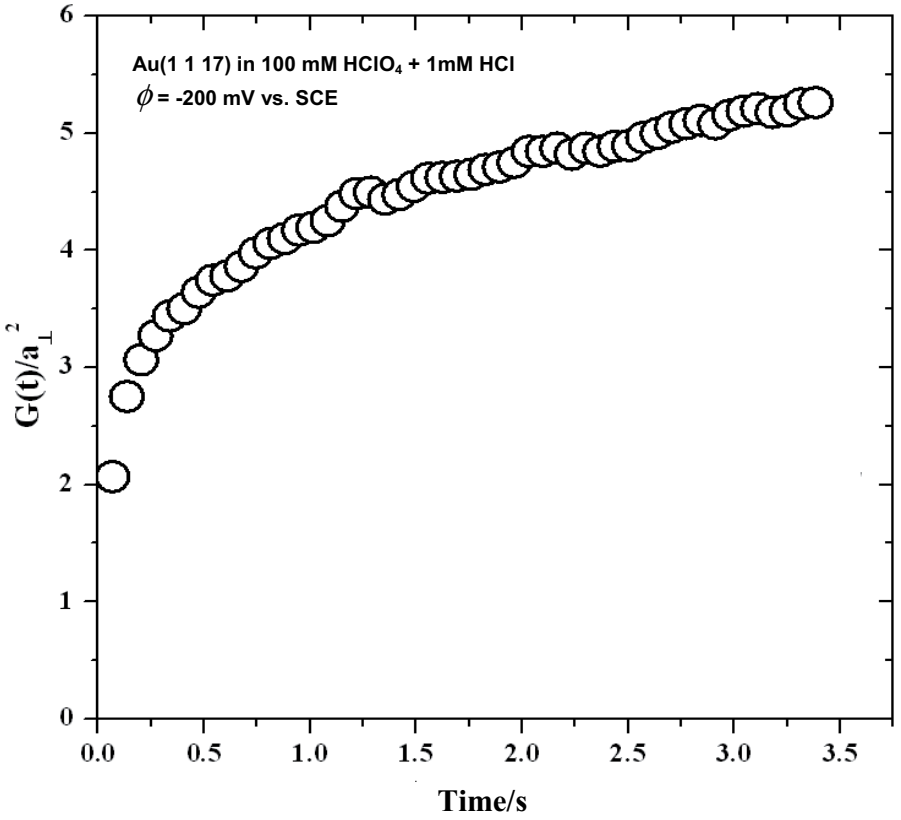

Fig.(5-3): Time correlation function for Au(1 1 17) in 10 mM $HClO_4$ + 1 mM HCl at ϕ = -200 mV vs. SCE.

the value as observed for $\phi \leq$ 400 mV vs. SCE and merely slightly increases for ϕ up to +600 mV. Close inspection shows that this slight increase at $\phi \geq$ 450 mV vs. SCE might be fitted to an exponential.

For further analysis of the time exponent of $G(t)$ the $G(t=0)$ as displayed in figure (5-4) was subtracted from $G(t)$. Figure (5-5) shows a log-log plot of the time correlation function as measured for Au(1 1 17) in 100 mM $HClO_4$ + 1mM HCl at different electrode potentials -200, -110, -10, +192, +341 mV vs. SCE with the offset subtracted. The data were obtained from surface areas with an average step-step distance of 39±7Å. According to figure (5-1) the surface is reconstructed at -200, -110 and -10 mV vs. SCE and unreconstructed at +192 and +341 mV. As shown in figure (5-5) the time correlation function is approximately linear in time t. Hence, $G(t)$ obeys a power law dependence on t. One obtains the time exponent α of the power law from the slope of a linear fit (solid line) to the data in the log-log plot. From figure (5-5) a time exponent α close to 1/2 is found.

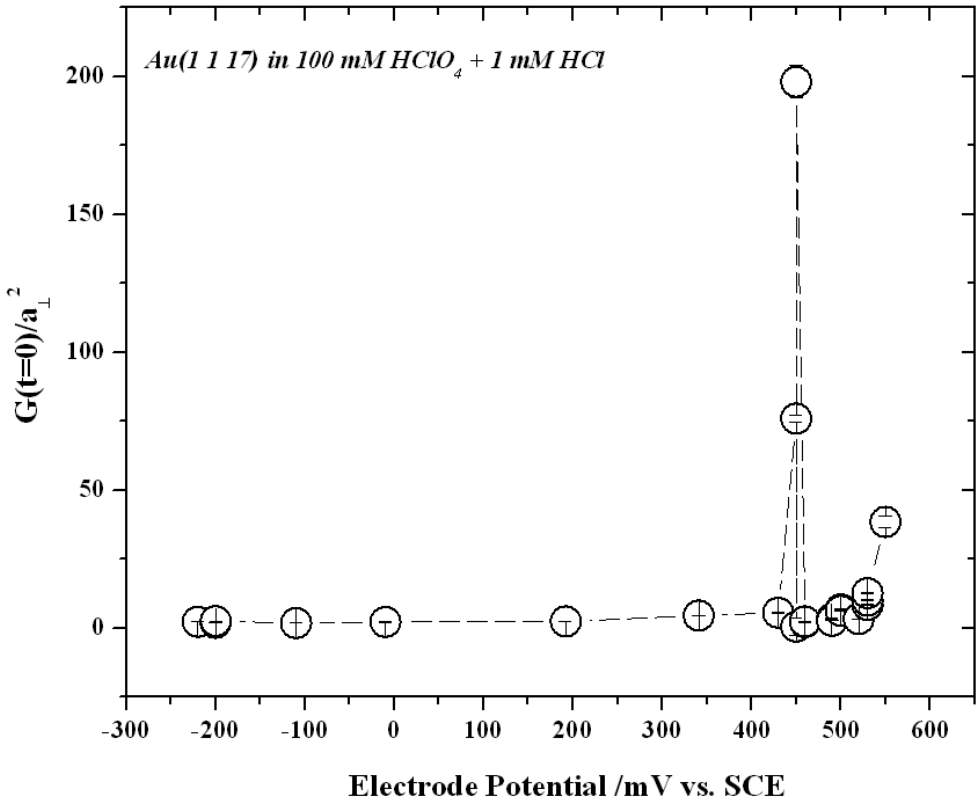

Fig.(5-4): Correlation value $G(t)$ at t=0 as a function of electrode potential. The values of $G(t=0$ s) are given in kink lengths squared.

Figure (5-6) shows the log-log plot of the time correlation function for high potentials, ϕ = +430, +460 and +490 mV vs. SCE. Again $G(t)$-$G(t=0)$ obeys a t^{α} power law, now with $\alpha \approx 0.75$ though. This is a surprisingly large time exponent. We also observed this time exponent for potentials above +490 mV vs. SCE.

As a summary, figure (5-7) shows the measured time exponents versus the electrode potential for all data obtained in this thesis. As shown in the figure, one can classify the time exponent α into two categories depending on the electrode potential regime: Below ϕ = +400 mV vs. SCE, the time exponent is close to 1/2. And above ϕ = +400 mV vs. SCE the time exponent is close to 3/4. The dotted and the solid lines in figure (5-6) correspond to the theoretical exponents for $t^{1/4}$ and $t^{1/2}$ cases, respectively. The dashed line corresponds to a theoretical exponent of $t^{0.75}$ The shaded area in the figure corresponds to the standard deviation of the mean value of all data above +400 mV vs. SCE.

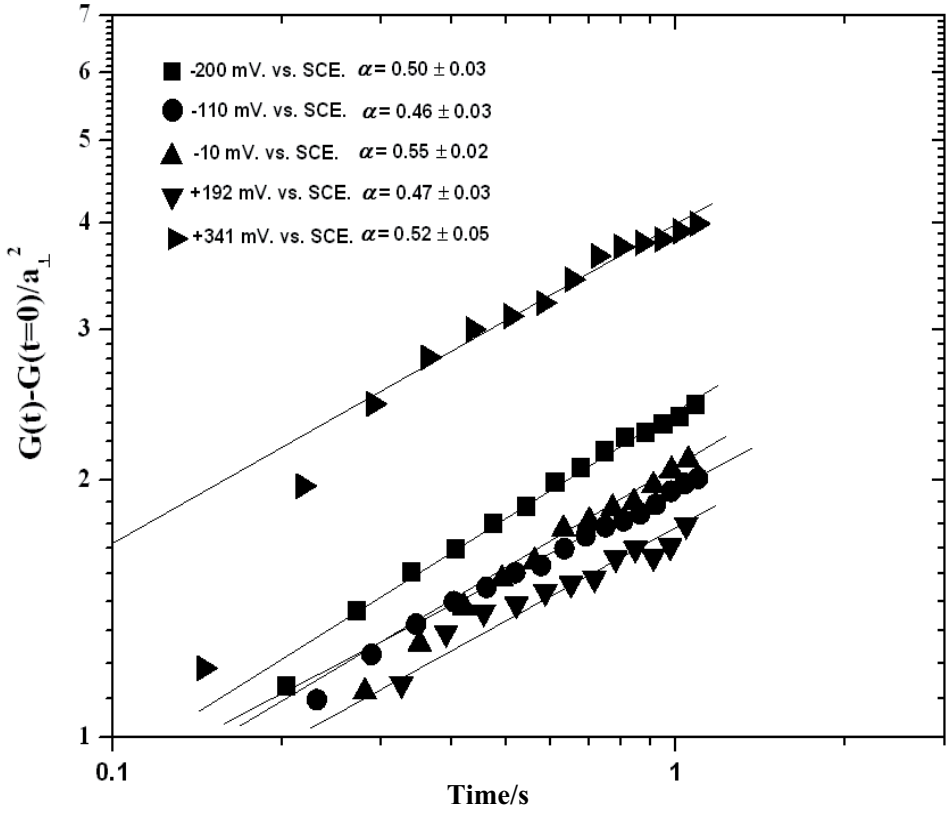

Fig.(5-5): Log-log plot of the time correlation function versus time for electrode potentials -200, 110, +192, +341 mV vs. SCE. Here, the correlation function $G(t)$ is plotted with the constant offset at t=0, $G(t=0)$, subtracted (see text for further discussion).

In order to analyze the influence of the electrode potential on the step fluctuations we studied furthermore $G(t)$ for constant time and various potentials. In figure (5-8), $G(t=2\text{ s})$-$G(t=0)$ is plotted versus ϕ. There is no obvious dependence of the correlation function on the electrode potential below +400 mV vs. SCE. Around +450 mV vs. SCE a sudden increase in the correlation function is observed similar to that one found for $G(t=0)$ at the same potential (figure (5-4)).

For even higher potentials, the correlation function decreases rapidly again and then merely slightly increases with increasing electrode potential. This is analogue to the findings for $G(t=0)$. The solid line is a fit to an exponential which will be discussed in detail in section 5.4.

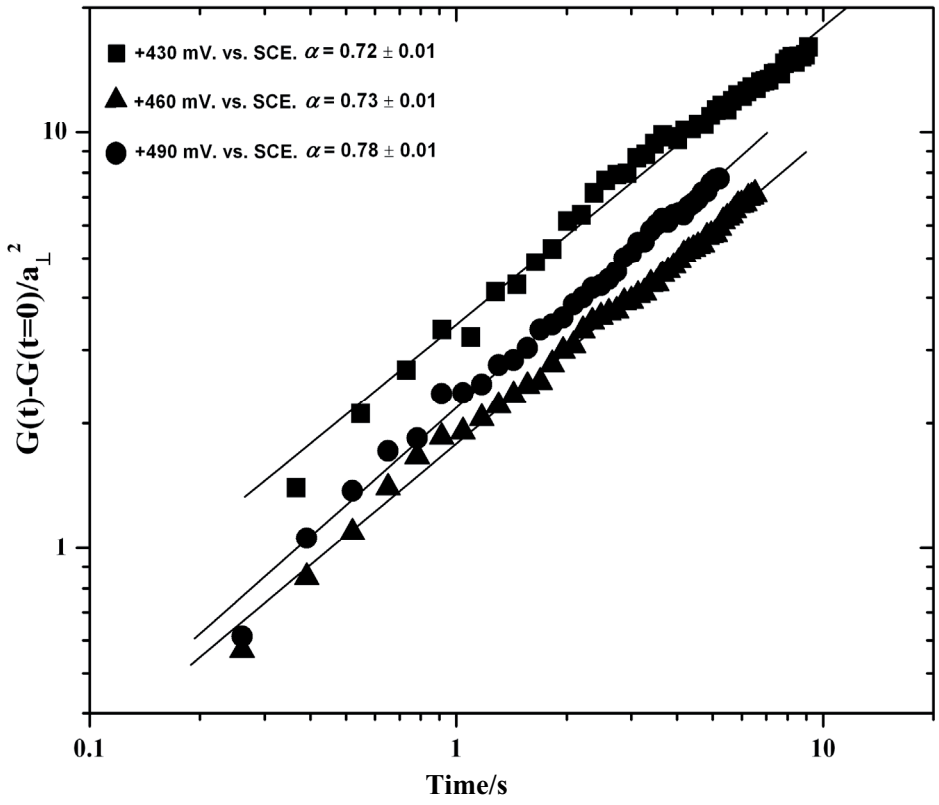

Fig.(5-6): Log-log plot of the time correlation function $G(t)$-$G(t=0)$ versus time for +430, +460 and +490 mV vs. SCE.

In order to understand the sudden increase of $G(t=2\text{ s})$-$G(t=0)$ around ϕ = +450 mV vs. SCE one may consider a possible dependence of $G(t)$ on the mean step-step distance L (e.g. eq. 2.19) and following). Therefore we analyzed the data by systematically dividing the data into

ensembles of comparable local step-step distance. Figure (5-9) shows $G(t=2\text{ s})$-$G(t=0)$ versus L for constant electrode potential ϕ for low (ϕ<400 mV) and high (ϕ> 400 mV) potentials: Triangles represent data below +341 mV vs. SCE and squares data between +430 and +530 mV vs. SCE. The values of the step-step distance L is given in kink lengths ($a_{\perp} = 0.289$ nm). As presented in chapter 2, the possible exponents of L described by theory may be ±1/2, 1/4, depending on the dominant mass transport involved in the step fluctuations.

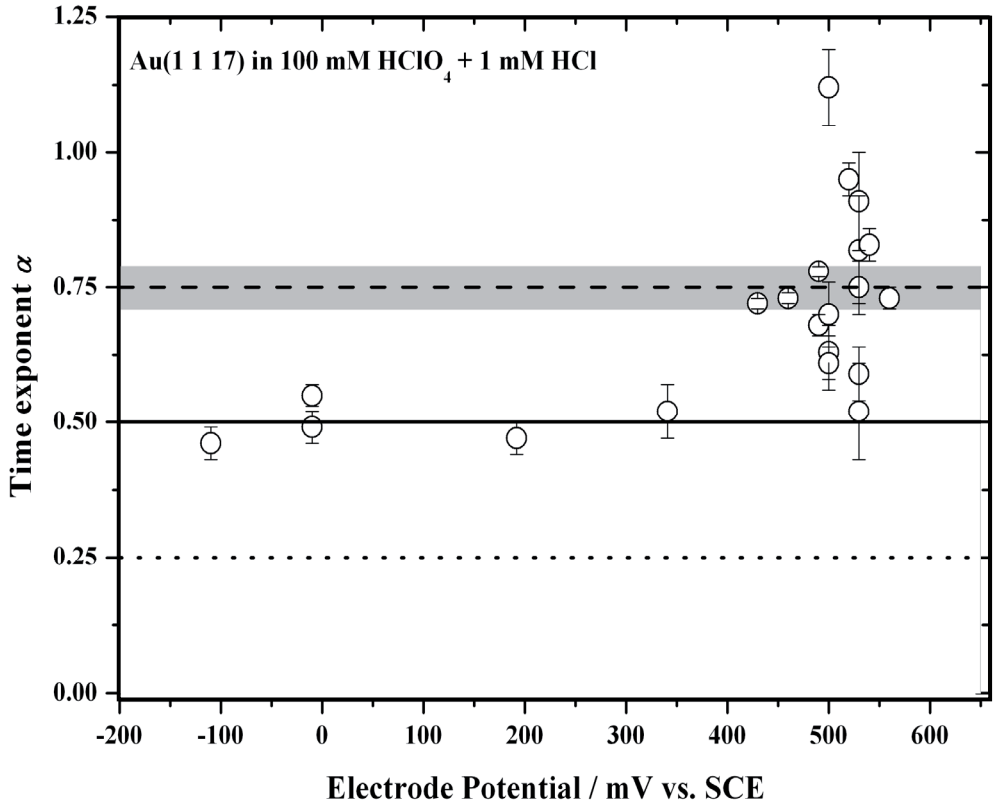

Fig.(5-7): Time exponent α versus the electrode potential for Au(1 1 17) in 100 mM $HClO_4$ + 1mM HCl. The error bars represent the standard deviation of all analyzed data at a distinct electrode potential. The dotted, solid and dashed lines correspond to the theoretical exponents for $t^{1/4}$, $t^{1/2}$ and $t^{0.75}$, respectively. The shaded area in the figure corresponds to the standard deviation of mean value of all data measured above +400 mV vs. SCE

Below +400 mV vs. SCE a time exponent α close to 1/2 was found (figure (5-5)), hence, one might expect a $L^{-1/2}$ or $L^{1/4}$-dependence (eq. 2.21, 2.22). We do not observe, however, a clear L dependence in the potential range below +400 mV vs. SCE (open triangles). The correlation function seems to be independent on the step-step distance L.

However, the range of L we were able to cover in experiment is rather small, $10\,a_\perp \le L \le 80\,a_\perp$. In such a small L-range, it is impossible to distinguish a distinct L- dependence within the scattering of the data.

For electrode potentials above +400 mV vs. SCE, a strong increase in the correlation function with increasing step-step distance is observed (solid squares). The best fit to the data is a $L^{3/2}$ - law. An exponent 3/2 is not in accordance with any mass transport situation as described theoretically for equilibrium fluctuations (see chapter 2).

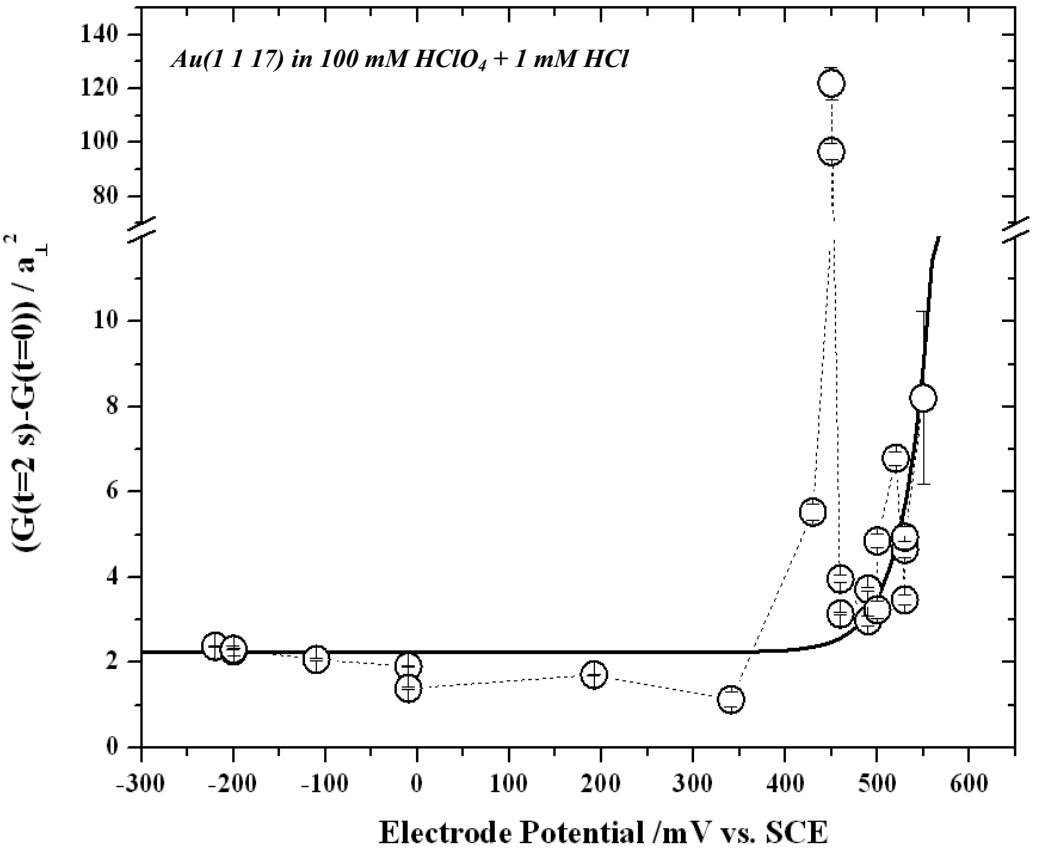

Fig.(5-8): Time correlation function at t=2 s as a function of the electrode potential. The value of the correlation function is given in kink lengths squared and is corrected for the constant offset $G(t=0)$.

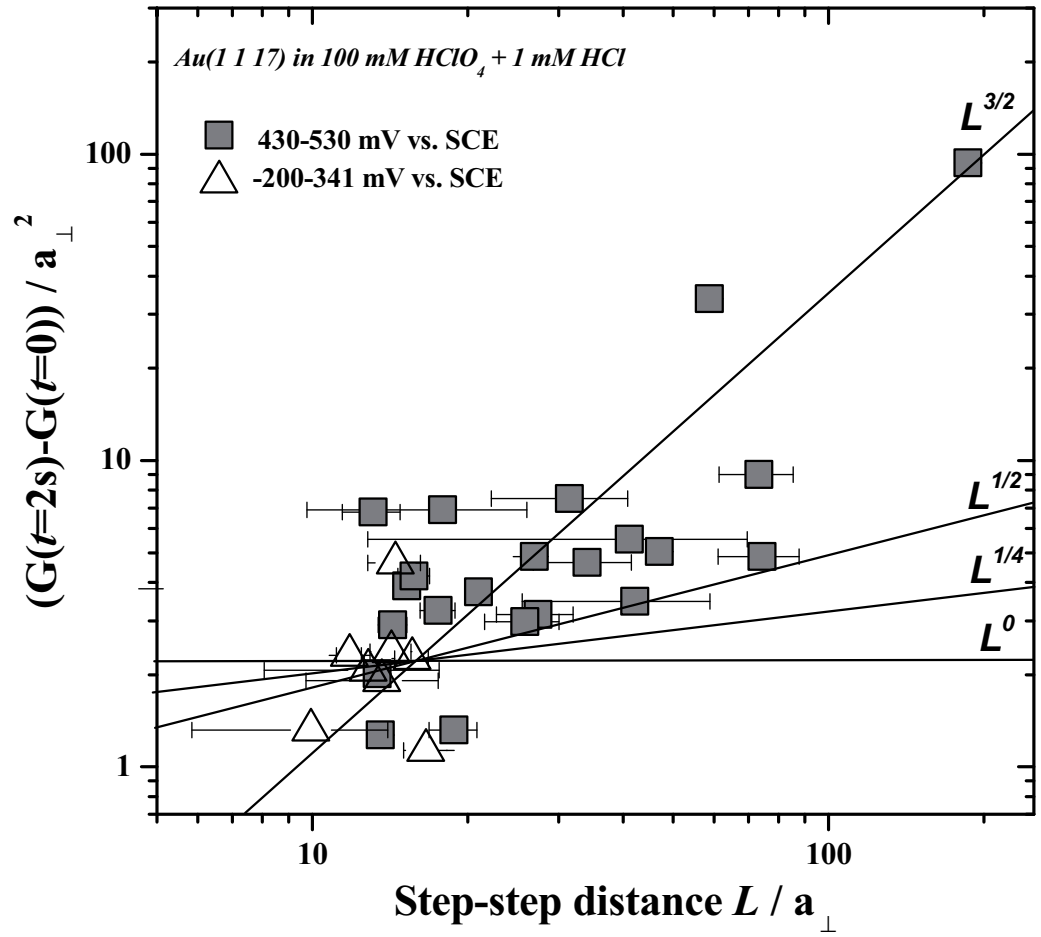

Fig.(5-9): Log-log plot of $G(t=2\ s)$-$G(t=0\ )$ vs. step-step distance L for Au(1 1 17) in 100 mM $HClO_4$ + 1mM HCl for different electrode potentials. The solid lines correspond to theoretical fits to the data with L^0, $L^{1/4}$, $L^{1/2}$ and $L^{3/2}$.

5.2.2. Time dependence step fluctuations on Au(1 1 29) in Bromide containing electrolyte

Figure (5-10) shows a time image of stepped Au(1 1 29) in 100 mM $HClO_4$ + 1mM KBr at room temperature around -170 mV vs. SCE. As for Cl^- containing electrolyte we measured the step correlation function $G(t)$ (equation (5-1)) and fitted it to a power law according to equation (5-2). Figure (5-11) shows $G(t)$ at ϕ = -150 mV vs. SCE. As for Cl^- electrolyte , $G(t)$ obeys a power law with a constant offset at t=0.

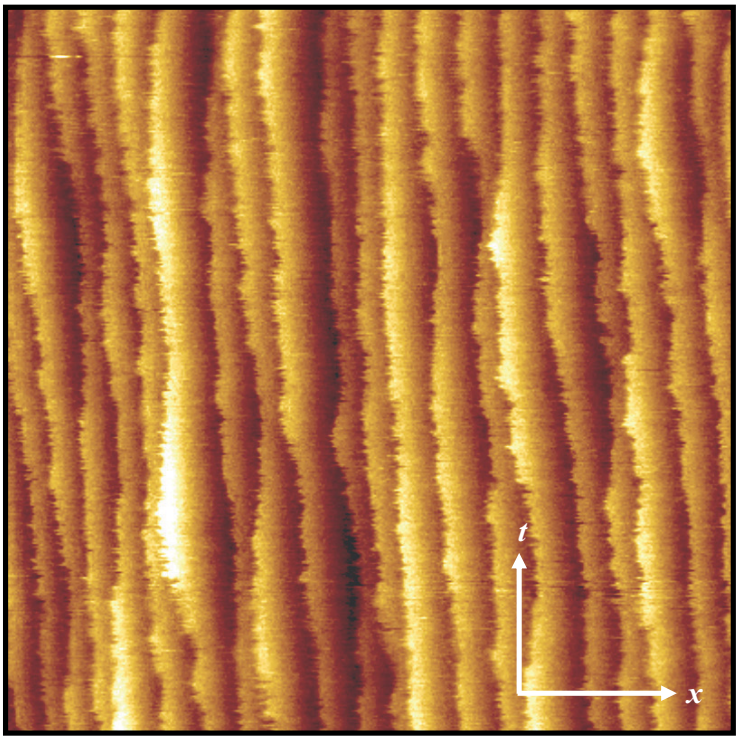

Fig.(5-10): Time image of Au (1 1 29) in 100 mM $HClO_4$ + 1 mM KBr at -170 mV vs. SCE. ***x*** and ***t*** axes are aligned perpendicular to, respectively, along the step edges. Total image time is 32.1 seconds, scan width 80 nm.

Figure (5-12) displays $G(t=0)$ versus electrode potential. As for Cl^- , $G(t=0)$ is almost constant at electrode potentials below +300 mV vs. SCE. Around +350 mV a sudden jump in $G(t=0)$ to high values is found. Then, $G(t=0)$ decreases again around +400 mV vs. SCE and remains constant, safe for some scattering.

Figure (5-13) shows the log-log plot of $G(t)$-$G(0)$ versus time for Au(1 1 29) in 100 mM $HClO_4$ + 1 mM KBr at electrode potentials -250, -220, -150 and +10 mV vs. SCE. The data were obtained from surface areas with a mean step-step distance L = 41±3.5 Å. The time exponent α as determined for the data in figure (5-13) varies between 0.32 and 0.67.

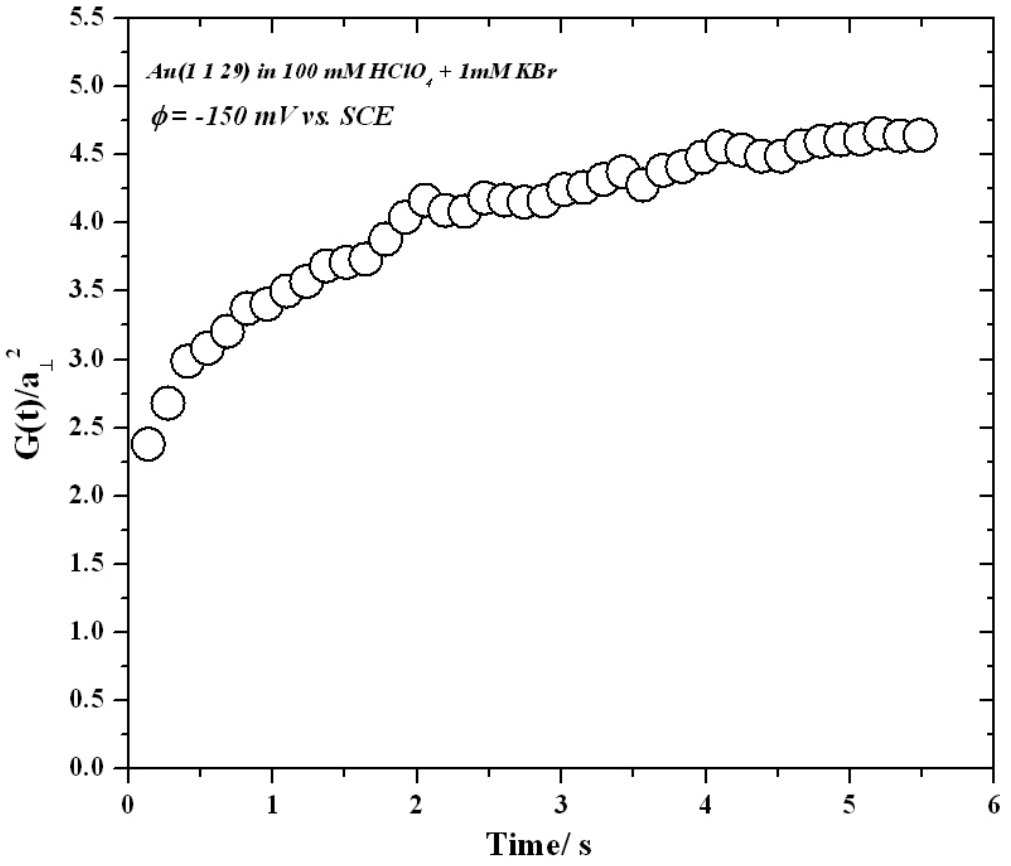

Fig.(5-11): Time correlation function for ϕ = -150 mV vs. SCE for Au(1 1 29) in 10 mM $HClO_4$ + 1 mM KBr.

In figure (5-14), $G(t)$-$G(0)$ as measured at higher potentials is displayed. In particular data obtained at +192, +260, +340 mV vs. SCE is plotted. At these potentials, the first ordered bromide adlayer is established on the surface (see figure (5-1)). In this potential range, the time exponent α is close to 3/4. Figure (5-15) summarizes the results and displays the time exponent versus electrode potentials.

$G(t$=2 s)-$G(t$=0) is plotted versus the electrode potential in figure (5-16). For electrode potentials below ~250 mV vs. SCE, the time correlation function does not depend on the potential within the experimental error. Above ~300 mV vs. SCE, however, a strong increase in the time correlation function is observed. All data may be fitted to an exponential as indicated by a solid line .

Figure (5-17) shows $G(t$=2 s)-$G(t$=0) versus L for constant electrode potential ϕ. We have classified the data into three different data sets measured in different potential ranges: One is

below pzc where the surface is reconstructed, one between +10 and +260 mV where the reconstruction is lifted, Br^- is specifically adsorbed on the surface, and the potential is close to the first ordered adlayer peak in the voltammogram (figure (5-1)). The third range is a potential range above +310 mV close to the formation of the $c(2\sqrt{2}\times p)\mathrm{R45}^\circ$ - structure. In the first two potential ranges, i.e. between -250…+260 mV vs. SCE, there is no significant dependence of the correlation function on the step-step distance *L*. For +341… +470 mV vs. SCE, a $L^{3/2}$ dependence is found.

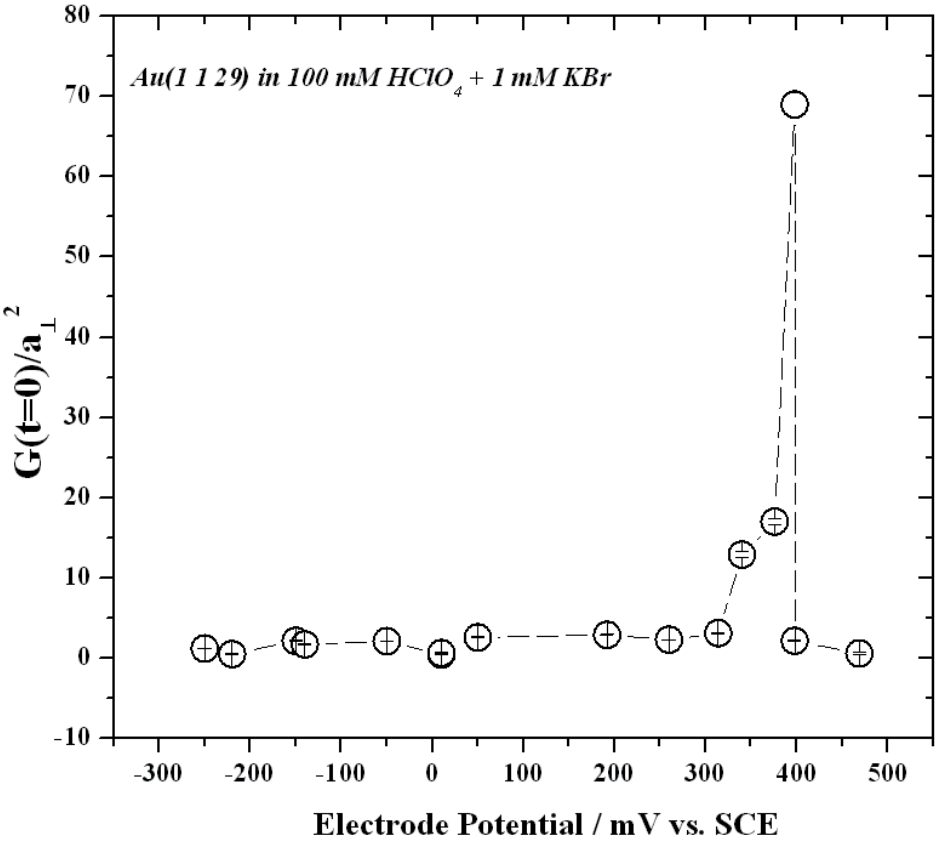

Fig.(5-12): Correlation value *G*(*t*) at *t*=0 s as a function of electrode potential. The values of *G*(*t*= 0 s) are given in kink lengths squared.

Note that at this electrode potential where $L^{3/2}$ is observed, the correlation function obeys a power law with time exponent α close to 3/4.

Finally, we looked at the appearance of step edges around +400 mV vs. SCE where the first bromide adlayer (see figure (5-1)) is established and is close to the formation of the second

adlayer peak. Figure (5-18) displays two STM images at +400 mV vs. SCE. The corrugation on the terraces between the steps corresponds to the $c(2\sqrt{2}\times 2\sqrt{2})R45^{\circ}$ Br^- adlayer.

Nevertheless, the step edges appear very frizzy, indicative of fast kink motion despite the Br^- adlayer.

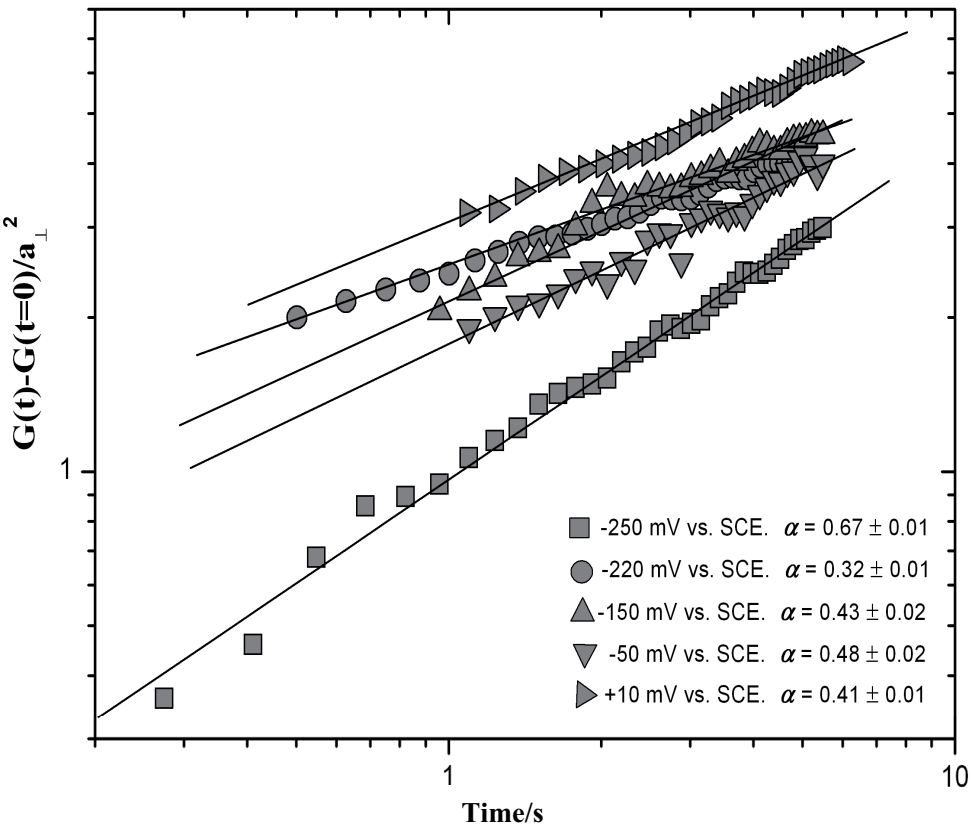

Fig.(5-13): Log-log plot of the time correlation function versus time for -250, -220, -150, -50 and +10 mV vs. SCE for Au(1 1 29) in 100 mM $HClO_4$ + 1mM KBr. The unit of the correlation function is given in kink length squared.

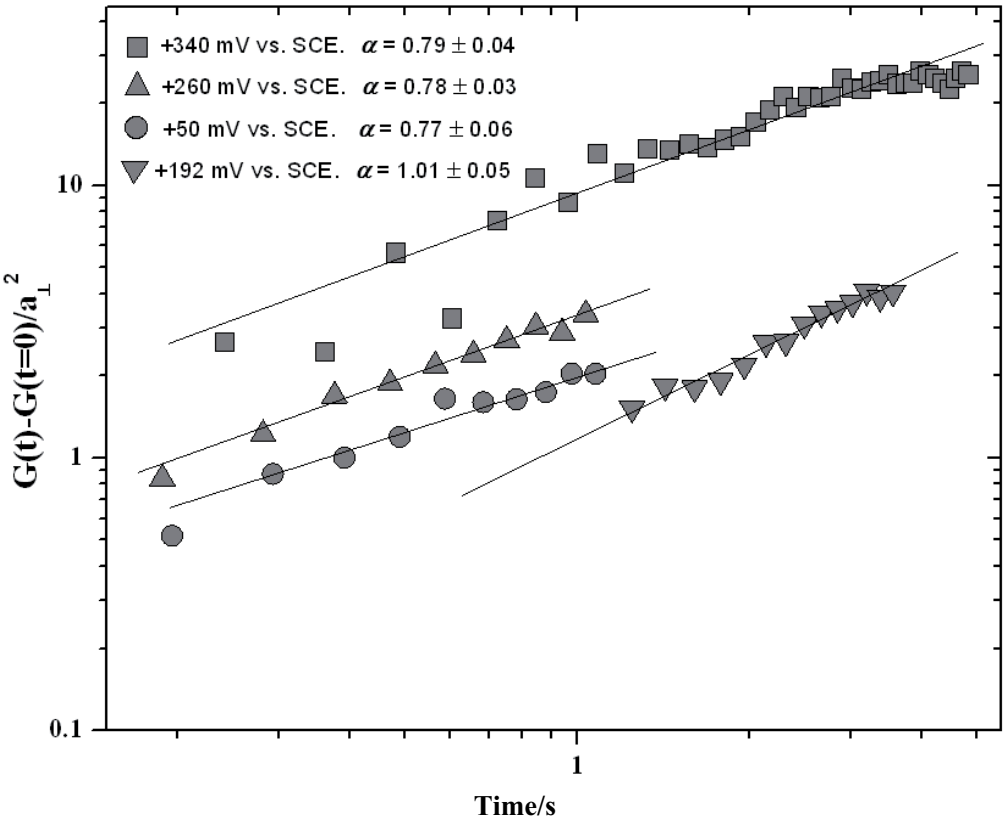

Fig.(5-14): Log-log plot of the time correlation function versus time for +50, +192, +260 and +340 mV vs. SCE for Au(1 1 29) in 100 mM $HClO_4$ + 1mM KBr. The unit of the correlation function is given in kink length squared.

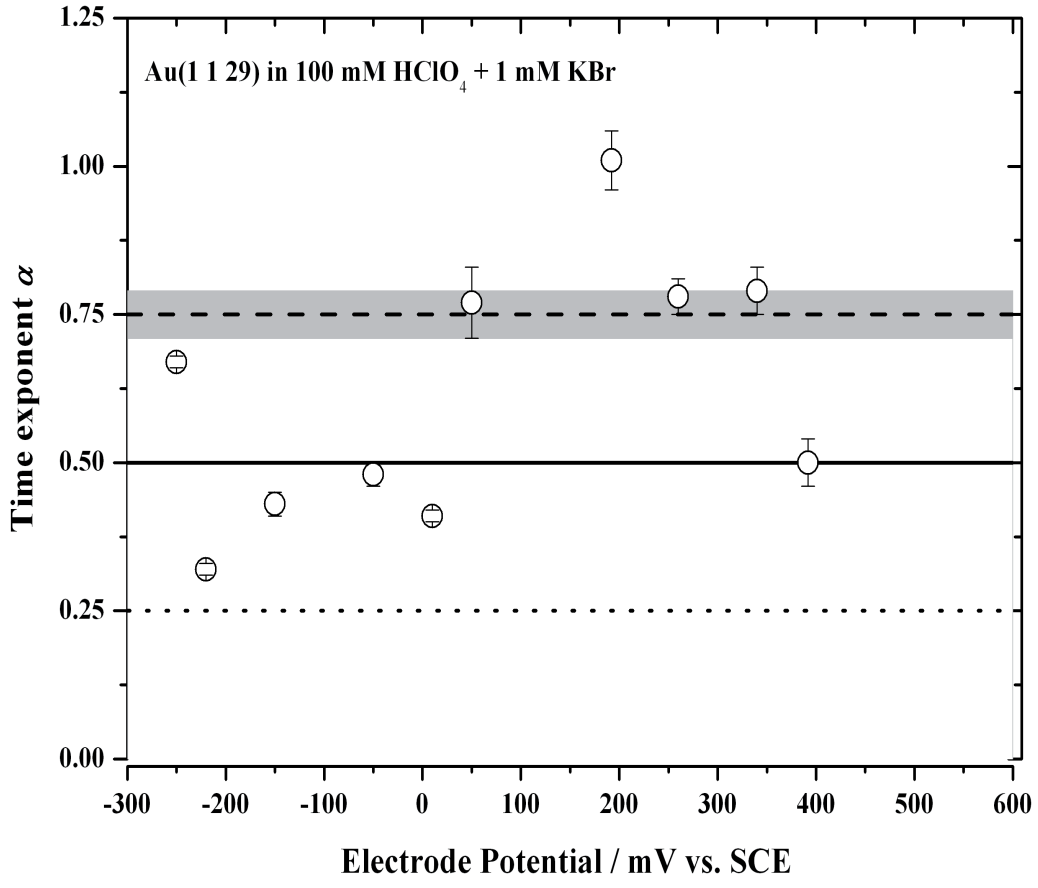

Fig.(5-15): Time exponent α versus the electrode potential for Au(1 1 29) in 100 mM $HClO_4$ + 1mM KBr . The error bars represent the standard deviation of all analyzed data at a distinct electrode potential. The dotted, solid and dashed lines correspond to the theoretical exponents for $t^{1/4}$, $t^{1/2}$ and $t^{0.75}$, respectively. The shaded area in the figure corresponds to the standard deviation of the mean value of all data above +50 mV vs. SCE

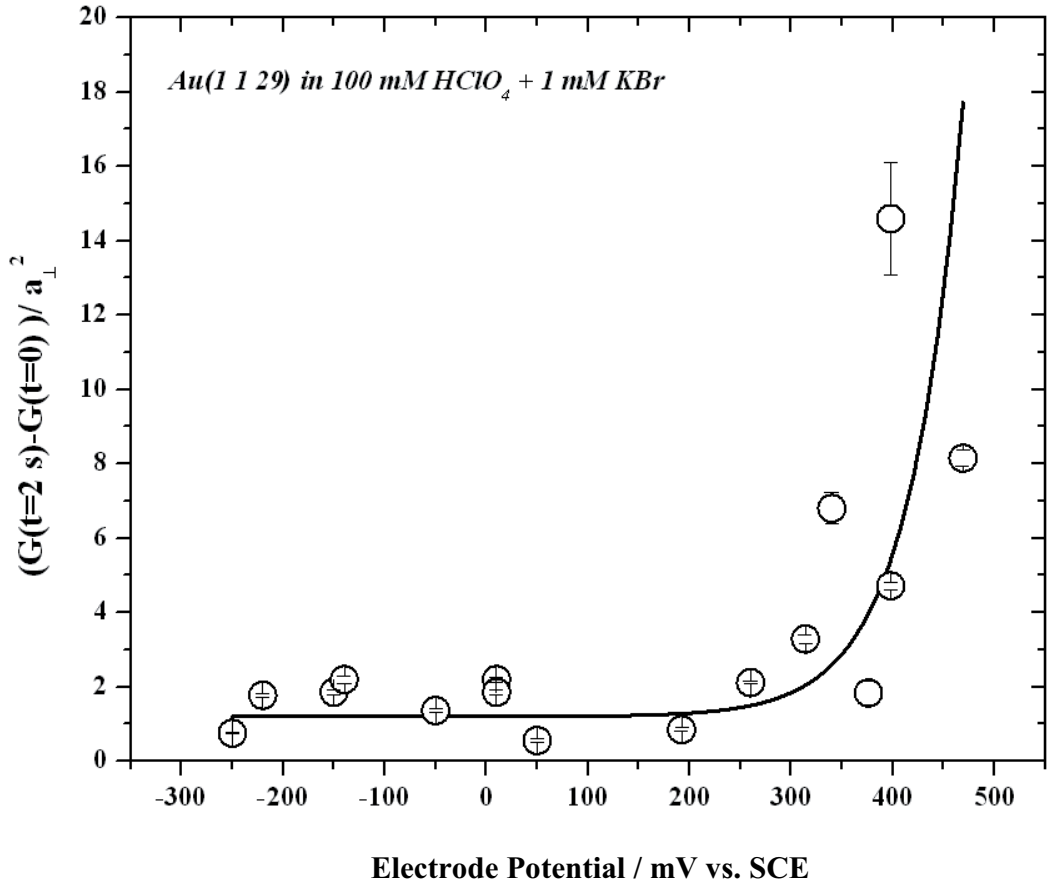

Fig.(5-16): Time correlation function at t=2 s as a function of the electrode potential. The value of the correlation function is given in kink lengths squared and is corrected for the constant offset $G(t=0)$.

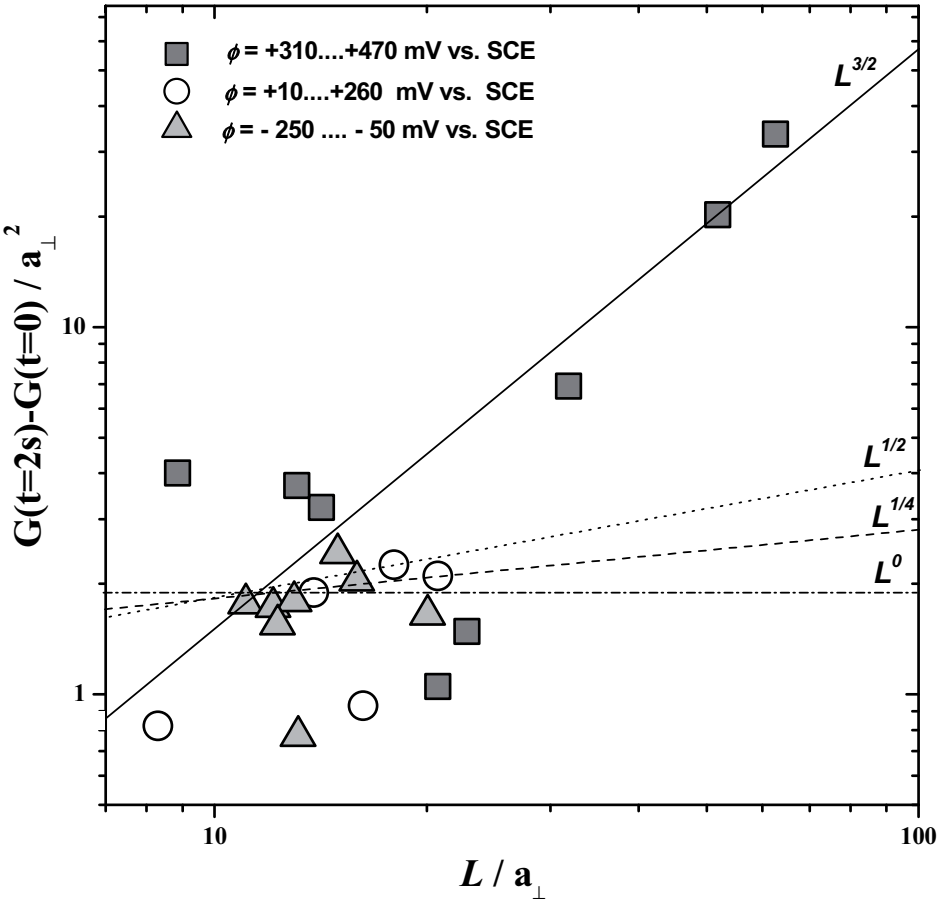

Fig.(5-17): Log-log plot of the time correlation function versus the step-step distance for Au(1 1 29) in 100 mM $HClO_4$ + 1mM KBr for different electrode potentials. The solid, dotted, dashed and dotted-dashed lines correspond to fits with $L^{3/2}$, $L^{1/2}$, $L^{1/4}$, and L^0,respectively.

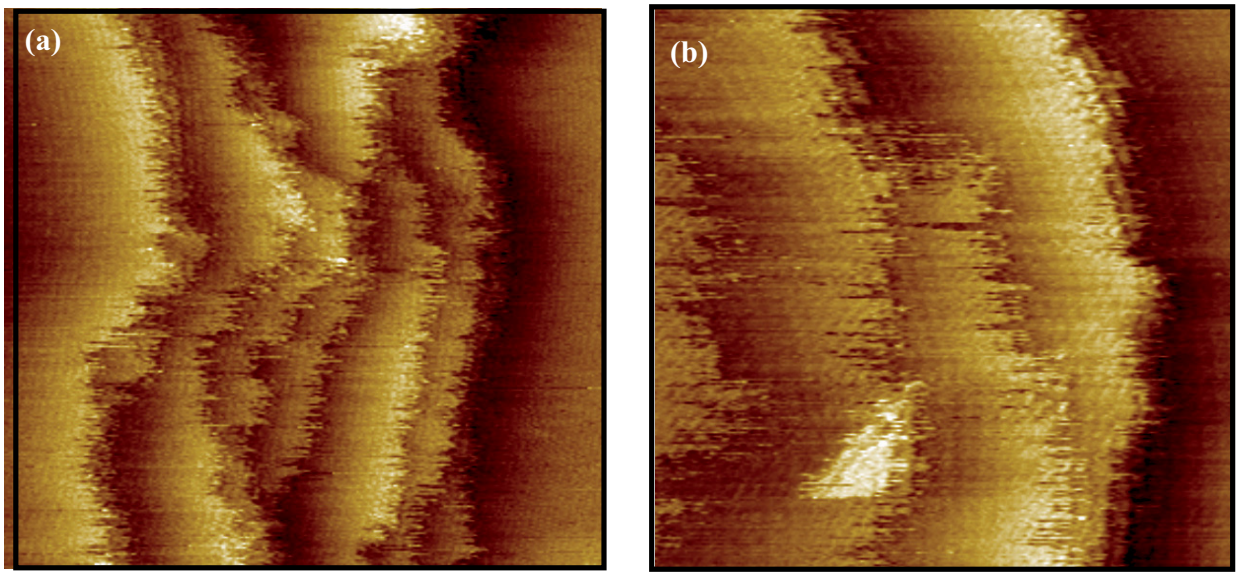

Fig.(5-18): STM images of Au(1 1 29) in 100 mM $HClO_4$+1 mM KBr at ϕ = +400 mV vs. SCE. The displayed area (a) 185x185 nm^2 and (b) 120x120 nm^2. (See text for discussion).

5.3. Spatial dependence of step fluctuations

An analysis of spatial step fluctuations can be performed, if the time contribution to the step fluctuations can be neglected, i.e. if surface diffusion is slow compared to the time required to scan an STM image. The spatial correlation function $G(y)$ is a linear function of the distance y along the step (equation (2-17), chapter 2)) and the slope is a measure for the kink energy (equation (2-13)). In this thesis, G(y) was measured for Au(1 1 17) in 100 mM $HClO_4$ + 1 mM HCl and for Au(1 1 29) in 100 mM $HClO_4$ + 1 mM KBr and from that we determine the kink energy ε and the kink dipole moment μ (see equation 5-4) for Au(1 1 n) in electrolyte.

5.3.1. Spatial step fluctuations on Au(1 1 17) in chloride containing electrolyte

In order to determine $G(y)$, the step structure is analyzed for constant time (t=0) , and normal STM images are required as described in section (2.3.2.2). The recorded step positions $x(y)$ were analyzed according to the correlation function

$$G(y,\phi_0) = \frac{1}{2}\left\langle \left(\Delta x(y,\phi_0) - \Delta x(y_0,\phi_0)\right)^2 \right\rangle \qquad (5\text{-}3)$$

Where y_0 is a reference position along the step and ϕ_0 is the electrode potential at which the measurement was performed. The difference Δ indicates that the $G(y,\phi_0)$ was determined from a step-pair analysis, where the distance Δx between two adjacent steps at y is correlated to their distance at $y_\circ$ in order to compensate partially for thermal drift.

Figure (5-19) shows a normal STM image of Au(1 1 17) in 100 mM $HClO_4$ + 1 mM HCl at -110 mV vs. SCE. As can be seen from the figure, the steps appear frizzy in the STM images. That is the assumption that kink diffusion can be neglected on the time scale of an image is not fulfilled. This becomes obvious also in the correlation function $G(y)$ as plotted in figure (5-20). Here, $G(y)$ as measured for Au(1 1 17) in Cl^- -containing electrolyte at +192 and +450 mV vs. SCE (circles and squares, respectively) is shown.

For $y < 5\ a_{||}$, $G(y)$ is not linear but obviously curved. This is indicative of the time contribution

to the STM image [14] . For $y > 5\,a_{\parallel}$, $G(y)$ becomes linear and the spatial information in the STM image prevails.

In order to determine the kink energy ε, we fitted only the linear part of the spatial correlation function $G(y)$. Table (5-1) is a summary of the results for the diffusivity and the kink energy obtained for Au(1 1 17) in 100 mM $HClO_4$ + 1 mM HCl .

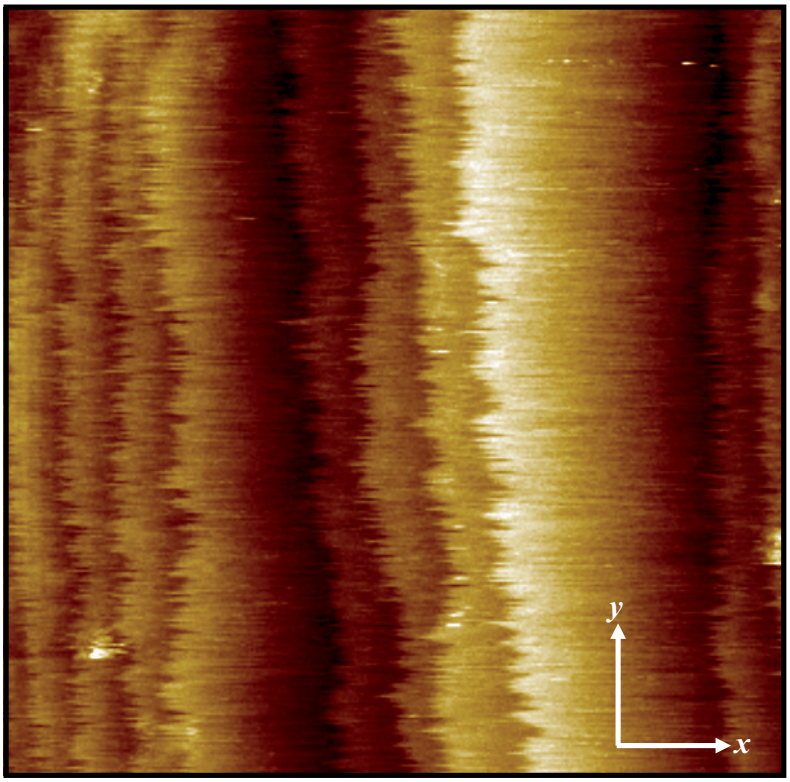

Fig.(5-19): STM image of Au(1 1 17) in 100 mM $HClO_4$+1 mM HCl at electrode potential ϕ = -110 mV vs. SCE. ***x*** and ***y*** axes represent the step position and the distance along the steps, respectively. The displayed area is 45.5x45.5 nm^2 .

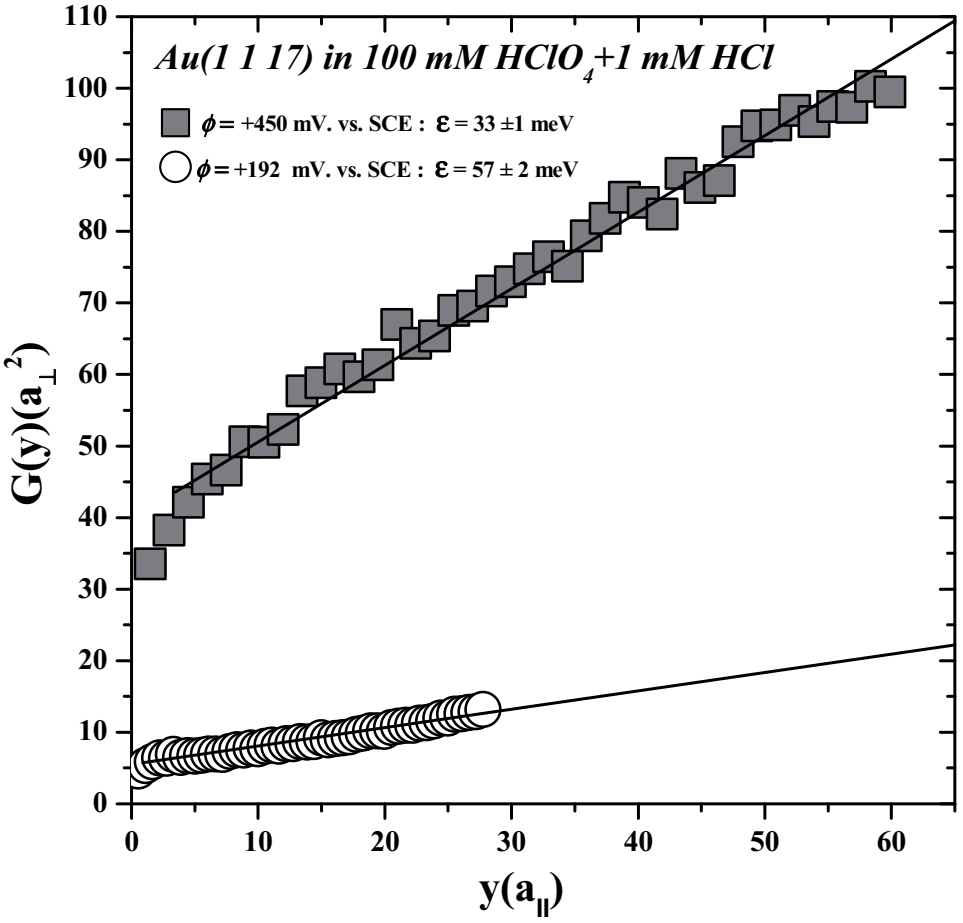

Fig.(5-20): Plot of the spatial correlation function *G*(y) at +192 mV vs. SCE (circles) and at +450 mV vs. SCE (squares) . The diffusivity b^2 respectively the kink energy ε can be determined from the slope of *G*(y) equation (2-14).

Table (5-1): Diffusivity b^2 and the kink energy ε as determined from *G*(*y*) for Au(1 1 17) in 100 mM $HClO_4$ + 1mM HCl at different electrode potentials.

ϕ /mV vs. SCE	Diffusivity $b^2/a_\perp^2$	Kink energy ε /meV
-110	0.098±0.009	78±4
-10	0.191±0.014	64±3
+192	0.267±0.011	57±2
+450	1.066±0.047	33±1
+550	1.55±0.1	27±1

5.3.2. Spatial step fluctuations on Au(1 1 29) in Bromide containing electrolyte

Fig (5-21) shows an STM image of Au(1 1 29) in 100 mM $HClO_4$ + 1mm KBr at ϕ = -250 mV vs. SCE. The spatial correlation function is analyzed in the same way as described in section (5.2.1) for Au(1 1 17) in 100 mM $HClO_4$ + 1 mM HCl .

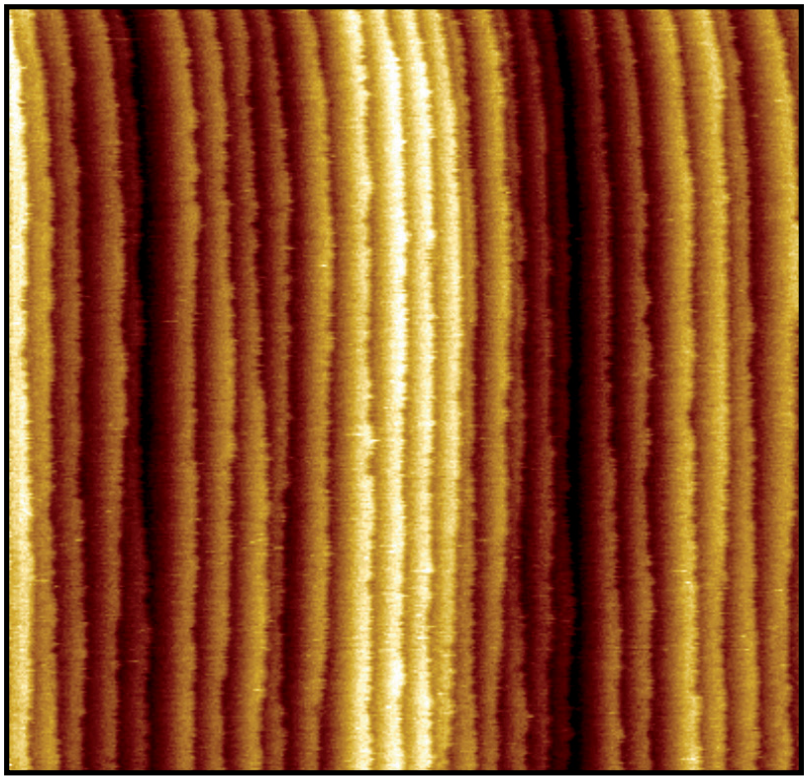

Fig.(5-21): STM image of Au(1 1 29) in 100 mM $HClO_4$+1 mM KBr at ϕ = -250 mV vs. SCE. The displayed area is 107x107 nm^2 .

Figure (5-22) shows the plot of the spatial correlation function $G(y)$ for two different electrode potentials: -250 mV vs. SCE (circles) and -70 mV vs. SCE (squares). Compared to Cl^--containing electrolyte (figure (5-20)), the steps appear less frizzy in KBr-solution at this potential. This is confirmed by the spatial correlation function. $G(y)$ is almost linear for both potentials and merely for very small y a slight curvature is observed indicative of a small time contribution.

Table (5-2) shows the results for b^2 and ε where the data for $G(y)$ is fitted linearly in the spatial

regime (y> ~ $10\,a_{\parallel}$). The diffusivity increases with increasing electrode potential. Hence, the kink energy ε decreases with increasing electrode potential. This result is analogue to the Cl^- containing electrolyte (table 5-1). Figure (5-23) shows a plot of the kink formation energy ε versus electrode potential using the data from table (5-1) and table (5-2).

Table (5-2) shows the calculated diffusivity b^2 and the kink energies ε at different electrode potentials.

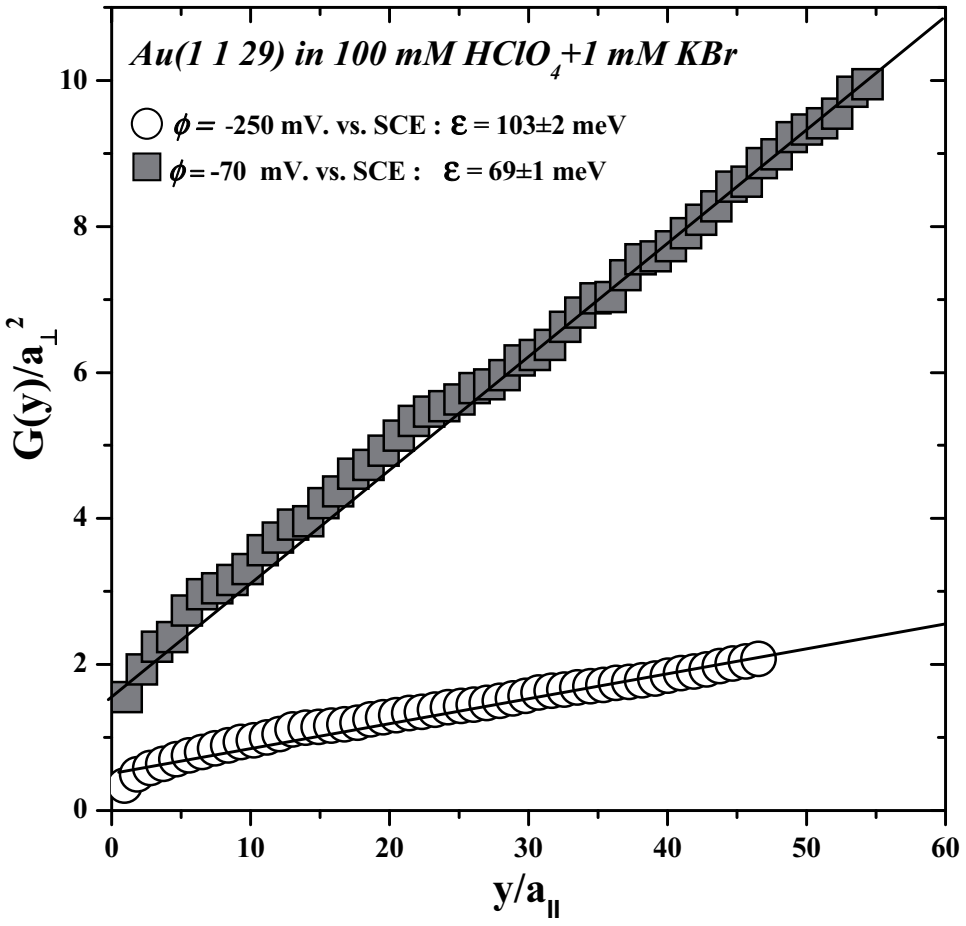

Fig.(5-22): Plot of the spatial correlation function $G(y)$ at -250 mV vs. SCE (circles) and at -70 mV vs. SCE (squares) .The diffusivity b^2 and the kink energy ε can be determined from the slope of $G(y)$.

Table (5-2): Diffusivity b^2 and kink energy ε for Au(1 1 29) in 100 mM $HClO_4$ + 1mM KBr at different electrode potentials as determined from $G(y)$ (equation (2-14)).

ϕ /mV vs. SCE	Diffusivity $b^2/a_\perp^2$	Kink energy ε /meV
-250	0.03±0.004	103±2
-70	0.15±0.002	69±1
+400	0.53±0.066	44±9

5.3.3. Determination of the kink dipole moment

As we found from the analysis of the spatial correlation function at various potentials, the kink formation energy ε depends linearly on the electrode potential (figure (5-23)). According to [83] the potential dependence of the kink formation energy can be expressed via

$$\varepsilon(\phi) = \varepsilon(0) - \frac{\mu}{\varepsilon_0}\sigma(\phi) \qquad (5\text{-}4)$$

Where $\varepsilon(0)$ is the kink formation energy at ϕ=0, μ is kink dipole moment, σ is the potential-dependent surface charge. The latter can be experimentally determined from electrochemical capacity measurements. ε_0 is the vacuum permittivity. The second term in equation (5-4) is the electrostatic energy contribution of the related dipole moment in the electric field at the interface. In order to obtain the kink dipole moment μ, one has to plot the kink formation energy ε versus the charge σ. The slope of the plot is $\frac{\mu}{\varepsilon_0}$.

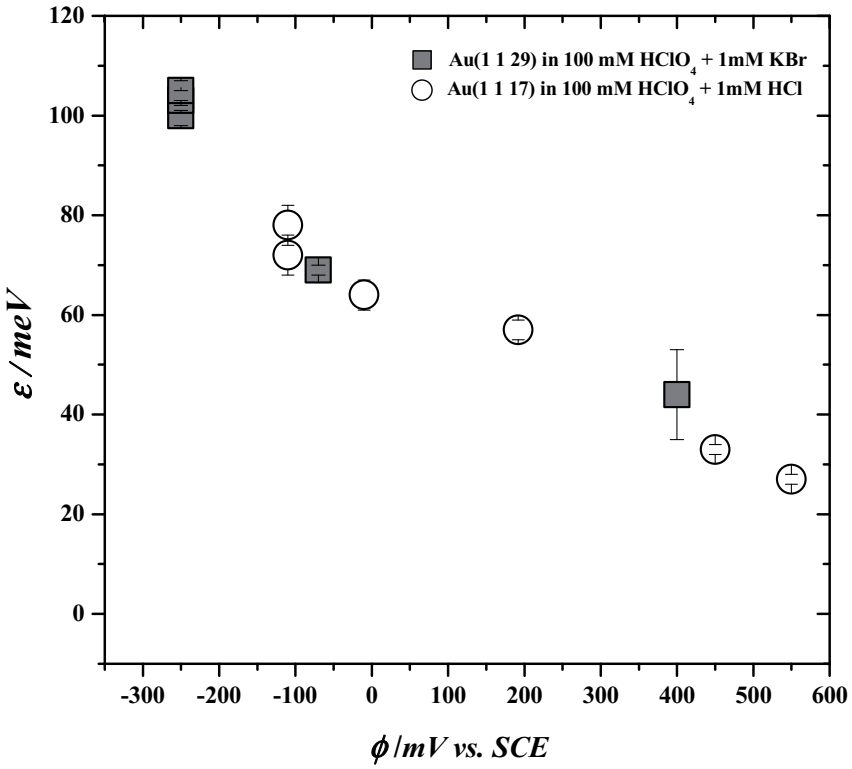

Fig.(5-23): Plot of the kink formation energy ε as a function of the electrode potential for Au(1 1 29) in 100 mM $HClO_4$ + 1mM KBr (squares), and for Au(1 1 17) in 100 mM $HClO_4$ + 1mM HCl (circles).

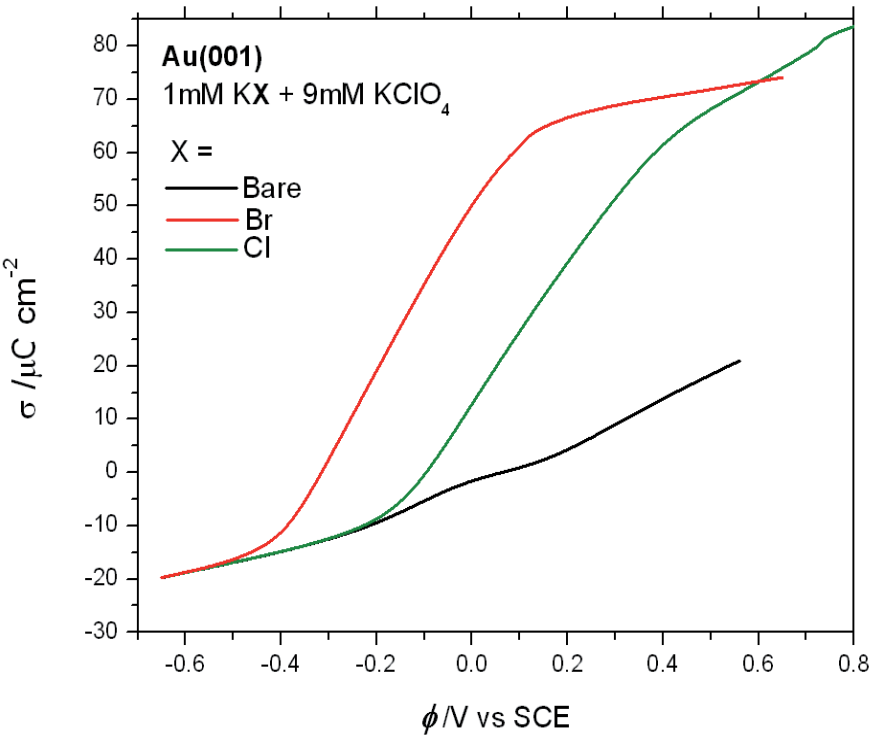

Fig.(5-24): Plot of the surface charge density as a function of the electrode potential for Au(100) in 1 mM KBr + 9 mM $KClO_4$ (red), 1 mM KCl + 9 mM $KClO_4$ (green) and without halides (black) (courtesy of G. Beltramo) .

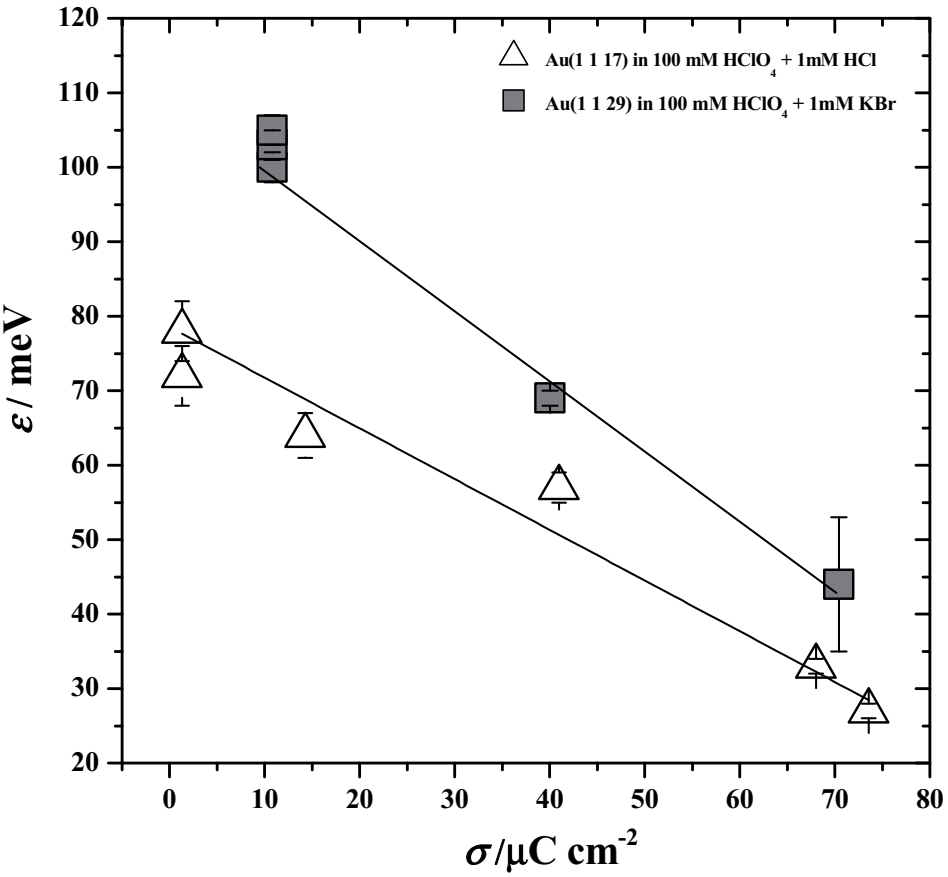

Fig.(5-25): Kink energy ε versus surface charge σ. The latter is obtained from the integral of the specific capacity C measured (negative sweep) for Au(100) in 9 mM $KClO_4$ + 1 mM KCl, and for Au(100) in 9 mM $KClO_4$ + 1 mM KCl.

In this thesis, the surface charge was obtained by integration of the specific capacity of Au(100) in 9 mM $KClO_4$ + 1mM KCl, and for Au(100) in 9 mM $KClO_4$ + 1 mM KBr. Figure (5-24) shows the plot of the charge density versus electrode potential for Au(100) surface in 1 mM KBr + 9 mM $KClO_4$ (red line), in 1 mM KCl + 9 mM $KClO_4$ (green line) and without halides (black). Figure (5-25) shows the plot of the kink formation energy ε as a function of the charge density σ. The kink dipole moment can be calculated from the linear fit of the experimental data for Cl^- and Br- containing electrolytes, and values of $\mu^{Cl} = (6.0\pm0.7)\text{x}10^{-3}$ eÅ and $\mu^{Br} = (10.1\pm0.6)\text{x}10^{-3}$ eÅ are obtained.

5.4. Discussion

As was previously demonstrated for Ag(111), Cu(100) and Au(111) surfaces in electrolyte [14,36,38,44] and theoretically considered in [96], one may determine the surface mass transport and the relevant activation barriers by analyzing the potential dependence of step fluctuations. For that purpose, the exponential increase of $G(t)$ with potential ϕ for constant time as found in most metal electrodes so far (Ag(111) [89], Au(111) [38], Cu(100) [45]) can be reduced to a linear dependence of all activation and defect formation energies [96] relevant in the surface mass transport. The observation of a potential dependent constant offset $G(t=0)$ is not new, rather it has also been observed on Cu(9 9 7) and on stepped Ag(1 1 1) in UHV [89]. In electrolyte, a constant offset was so far observed on stepped Ag(1 1 1) in Cu^{2+} containing electrolyte [45]. The physical reason for the constant offset is not understood yet. A clue to its origin may be the second finding that at a distinct potential (+400 mV vs. SCE for Cl^--electrolyte, +350 mV vs. SCE for Br^-- electrolyte) $G(t=0)$ increases dramatically, just to drop to small values at even higher potentials. The sudden increase occurs close to a potential where the adlayer-structure is nearly formed. Hence, the surface undergoes a phase transition with large fluctuations. In this case, the tip may considerably influence local diffusion processes due to tip-surface interactions and hence enlarged contributions of the tip to $G(t)$ are observed. This interpretation is corroborated by the finding for the time exponent of $G(t)$: In the case of Au(1 1 17) in 100 mM $HClO_4$ + 1 mM HCl, for low electrode potentials (below ~350 mV vs. SCE) a time exponent α close to 1/2 is found. Around and above ϕ = +400 mV vs. SCE, time exponent α assumes values close to 3/4 which is larger than any physical exponent described by theory [97]. Simultaneously, the L-dependence obeys a $L^{3/2}$, neither explained by theory. It is reasonable to assume that the critical behavior of the time exponent as well as the exponent of the L-dependence has its origin in large system fluctuations due to a phase transition of the surface structure as is expected close to the formation potential of the ordered $c(\sqrt{2}\times p)$R45° Cl^- adlayer. When the system is close to a phase transition, one may assume that locally small patches of ordered adlayers are formed which are very dynamic and unstable and which might be easily affected by the tunneling tip. This would explain a large constant offset.

Because of α=1/2 and $L^{\sim 0}$, the most probable mass transport below 350 mV is exchange of adatoms between kink sites and terraces. However, we cannot fully exclude an L-dependence

due to the lack of data for large values of L (figure (5-9)). However, we assume fast terrace diffusion to be the most likely mass transport case. In that case the step correlation function below 400 mV vs. SCE is given by

$$G(t) = \sqrt{2\nu_a \, a_\perp^3} \; e^{-\varepsilon/2k_BT} \; e^{-E_{ad}^{\neq}/2k_BT} \qquad (5\text{-}2)$$

Where $E_{ad}^{\neq}$ is the activation energy for adatom creation and ν_a the attachment/detachment frequency. Obviously, the experimental fit does not go to zero for the exponential going to zero. This is also found for Ag(111) in electrolyte [45]. In the following the potential-independent offset will be neglected.

Furthermore, all data points within the large peak will be neglected, too. We consider merely data below +400 mV, respectively above +450 mV (in case of Cl^-), and below +300 mV and above +400 mV (in case of Br^-).

The formation of a terrace adatom is accompanied with a large dipole moment. Therefore, the activation energy $E_{ad}^{\neq}$ depends on the electrode potential, and it can be expressed as [89]

$$E_{ad}^{\neq} = E_{ad}^{0} - \lambda e \phi \qquad (5\text{-}3)$$

Where λ is a factor, e the electron charge and E_{ad}^{0} is the activation energy at ϕ = 0 which serves as a reference point. By inserting (5-3) into (5-2) with t= 2 s, and from an exponential fit (solid line in figure (5-8)) one obtains:

$$G(t=2) = \sqrt{2\nu_a a_\perp^3} \; e^{-(\varepsilon + E_{ad}^{\circ})/2k_BT} \; e^{\lambda e\phi/2k_BT} \; [2\,\mathrm{s}]^{1/2} \; = \; 2.67 + \mathrm{B}e^{\phi/\mathrm{A}} \qquad (5\text{-}4)$$

With $\nu_a \sim 10^{13}\ s^{-1}$. Due to the small number of data points, we could not find exact values for B and A based on the fitting. For example, from the exponential fit we obtained A~30 meV and B~7.3 $a_\perp^2$. From equation (5-4) one estimates: $\lambda \sim 1.7$ and $(\varepsilon + E_{ad}^{\circ}) \sim 0.17$ eV. These estimates depend sensitively on the choice of A and B : For example, A~50 meV yields B~ $2\,a_\perp^2$, $\lambda \sim 1$ and

$(\varepsilon + E_{ad}^{\circ}) \sim$ 0.6 eV. These values are all in a reasonable order of magnitude if compared for example with data from Cu(100), Ag(111) and Au(111) in electrolyte [38,44,45].

For Au(1 1 29) in 100 mM $HClO_4$ + 1 mM KBr, the time exponent α is close to 1/2 for low electrode potentials (-150, -50 and +10 mV vs. SCE). We found no indications for an *L*-dependence of *G*(*t*) at electrode potentials below +260 mV vs. SCE (figure (5-17)). Hence, the most probable mass transport is exchange of adatoms between kink sites and terraces. However, we cannot fully exclude a *L*-dependence due to the lack of data for large values of *L*. From figure (5-16), one can see that there is no dependence of *G*(*t*) on electrode potential below ~260 mV vs. SCE. Above ~ 300 mV vs. SCE an increase in the values of *G*(*t*) with increasing electrode potential is observed. This increase of *G*(*t*) is associated with a $L^{3/2}$-dependence and with a time exponent α close to 3/4. This behavior is almost similar to that observed for Au(1 1 17) in 100 mM $HClO_4$ + 1 mM HCl at electrode potential above +400 mV vs. SCE. Furthermore, we observed a large frizziness of the step edges at ϕ = +400 mV vs. SCE as seen from the STM images in figure (5-18). In contrast to Cu(100) in electrolyte [81] we do not observe a freezing of the step fluctuations upon adsorption of the ordered bromide adlayer. Therefore, the ordered bromide adlayer on Au(1 1 *n*) does not hinder or stabilize the fluctuations of the steps, rather, the ordered bromide adlayer might enhance the surface mobility of the Au.

For Au(1 1 29) in Br^- containing electrolyte we cannot estimate values for activation barrier from an exponential fit as for Au(1 1 17) in Cl^- containing electrolyte. As becomes obvious from figure (5-16) there is no increase of *G*(*t*) at potentials above 400 mV. Neglecting the data in the peak would in fact lead to a total absence of a dependence of *G*(*t*) on potential.

The question remains what might be the origin of the sharp peak in the plot of *G*(*t*) versus electrode potential. Under vacuum conditions, studies of the surface diffusion near a phase transition have been performed [90] .The authors found a jump in the activation barrier at critical temperature and the diffusion constant increases by ~ 3 orders of magnitude (see figure (2) in [90]). A similar phenomena may occur on stepped Au(1 1 *n*) in electrolyte. The formation of an ordered halide adlayer gives rise to a phase transition in the surface structure. A further structure transformation is related to the step bunching as discussed in chapter (4). The higher the electrode potential, the higher is the probability for surfaces to form step bunches (figure (4-17)).

This might also give rise to large fluctuations. Step bunches are also observed on Au(1 1 *n*) in bromide containing electrolyte as shown in figure (5-26). Systems near a phase transition undergo large system fluctuations [104]. Hence, the sudden increase of $G(t=2s)$-$G(t=0)$ for Cl electrolyte (figure (5-8)), respectively $G(t=0)$ (figure (5-12)) for Br electrolyte could be explained by critical fluctuations near a phase transition. Because of this critical behavior, it is not clear though whether an analysis of the activation barriers makes sense at all.

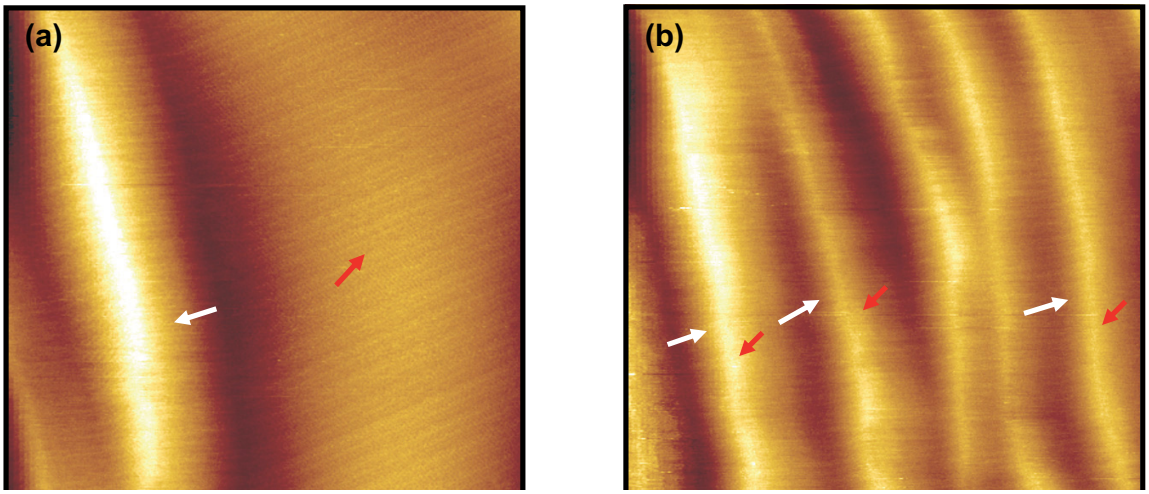

Fig.(5-26): STM images of Au(1 1 29) in 100 mM $HClO_4$ + 1mM KBr at electrode potential ϕ = +220 mV vs. SCE . The displayed area (a) 98.1x 98.1 nm^2 , and (b) 61.7 x 61.7 nm^2. The white and red arrows indicate the step bunches and the terraces, respectively.

The data for the kink energy as presented in this thesis can be compared with previous data for kink energies on Au electrodes in electrolyte. Figure (5-27) shows a summary of all data on Au(001) surfaces available so far: In [95] island studies on Au(001) in 100 mM $HClO_4$+1 mM HCl were performed from which numbers for the kink energy were obtained (light grey circles in figure (5-27)). Those data should be directly comparable to the data shown here (dark grey circles in figure (5-27)). Whereas in the previous study [95] an almost constant value of the kink energy of about 68 meV was found, within this thesis a strong potential dependence of the kink energy is obtained. Over the entire potential range considered in the experiments, kink energies from about 80 meV at low potentials down to about 30 meV around +550 mV SCE are measured. A very similar potential dependence is found for Au(1 1 *n*) in Br^- - electrolyte: Here, kink energies between above 100 meV and 44 meV are determined (dark grey triangles).

The kink energy values are in accordance with the data obtained for Au(001) in sulfate containing electrolyte [101], although, the non-monatomic potential dependence as obtained from the island studies in [95] and [101] cannot be confirmed in this thesis. A possible reason for this discrepancy of the kink energy data in this thesis compared to the previous island studies is that the determination of the kink energy from the island shape sensitively depends on the curvature analysis of the island shape in the <110>-direction. In praxis this means that one has to determine the curvature of the island shape in one particular point of the island boundary.

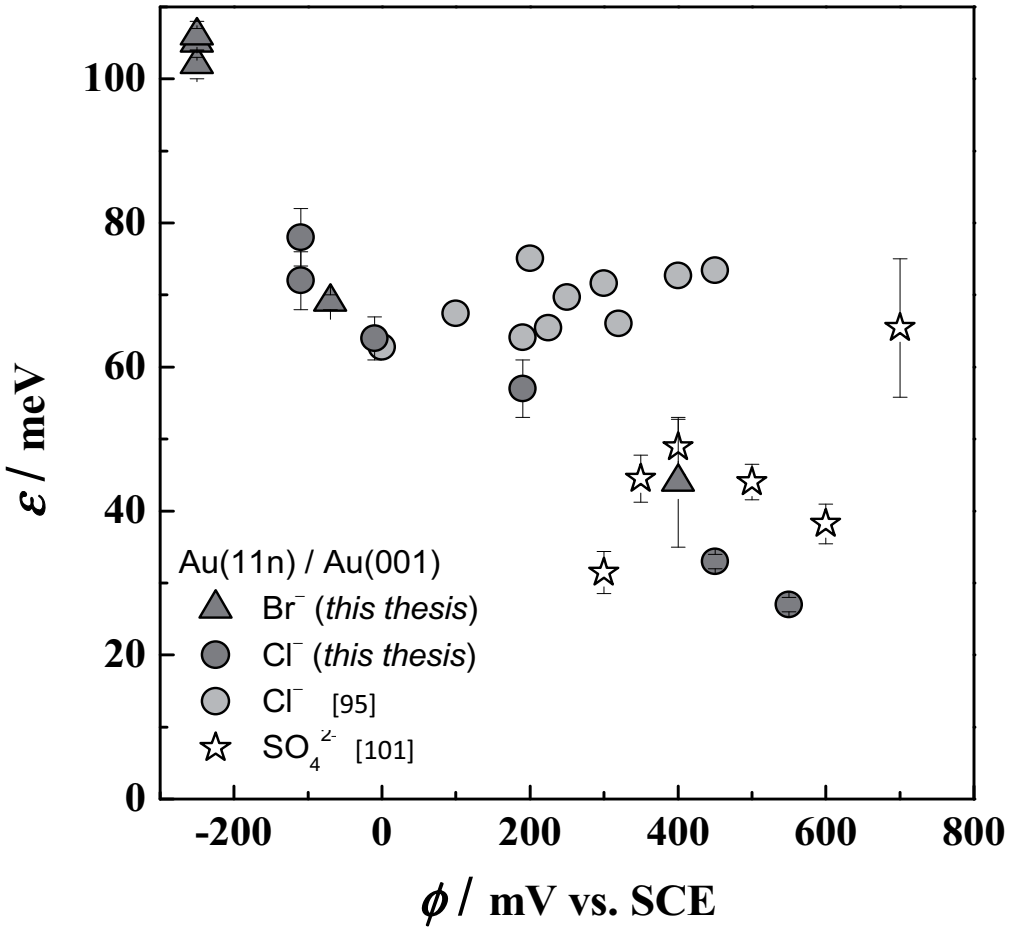

Fig.(5-27): A plot of the kink energy ε versus electrode potentials. The light grey circles and stars correspond to the kink energy ε as obtained from references [95] and [101] respectively. The Triangles and the dark grey circles correspond to the kink energy ε as obtained in this thesis. (see text for discussion).

Typically, approximations have to be made in order to determine the kink energy from the island shape which might introduce some errors. On the other hand it cannot be excluded that the determination of the kink energy as performed here in this thesis is influenced by thermal drift and misaligned steps: Due to the formation of an ordered adlayer, steps might locally reorient and misalign with respect to the atomically dense <110> direction. This misalignment leads to a high concentration of geometric rather than thermally activated kinks and might increase the spatial fluctuations substantially. Nevertheless the data available for Au(1 1 *n*), respectively. Au(100) surfaces in electrolyte seem to be in reasonable agreement and there seems to be a general trend towards smaller kink energies with increasing electrode potential.

One may also compare the data on the kink energies for Au(100) surfaces with previous data for Au(111) in chloride containing electrolyte: In reference [38] a kink energy ε=74±2 meV is found on Au(1 1 1) in 100 mM H_2SO_4 + 0.5 mM HCl at ϕ = -100 mV vs. SCE which fits nicely into the plot in figure (5-27).

From the relation between the kink energy and the surface charge (figure (5-25)), the kink dipole moments are calculated: μ^{Cl} = (6.02±0.7)x10^{-3} eÅ for Au(1 1 17) in Cl^- containing electrolyte and μ^{Br} = (10.08±0.6)x10^{-3} eÅ for Au(1 1 29) in Br^- containing electrolyte. To the best of our knowledge no other experimental data on kink dipole moment exist. Therefore, we can compare our data merely with data on step dipole moments. In reference [93], the authors studied the shift in pzc with step density on vicinal Au(100) electrodes which is proportional to the dipole moment per step atom p_z in weakly adsorbing electrolyte. The calculated step dipole moments are (6.8±0.8, 5.2±0.4, 5.8±0.5) x10^{-3} eÅ for SO_4^{2-}, ClO_4^- and F^- containing electrolytes, respectively. These values are comparable to those found for kink dipole moment here.

Chapter 6

Summary and outlook

This thesis focused on the study of the structural properties and the dynamics of vicinal Au(1 1 *n*) surfaces in electrolyte, with *n*= 7, 9, 11, 17 and 29. The first part of this work dealt with the study of the step bunching instability on Au(1 1 *n*) surfaces, with *n* =7, 9 and 11. We have analyzed a large number of STM images for all surfaces considered in this study and analyzed the height profiles and the orientation of step bunches. The analysis has been performed at negative potentials where the surfaces are considered to be reconstructed. The surfaces tend to undergo a phase separation into steep areas (step bunches) and areas almost free of steps. This observation is in agreement with previous studies.

We did not find a preferable certain orientation of the step bunches. Therefore, we have performed a systematic study on Au(1 1 9) surface to find the probability to find a certain local orientation. The probability histogram shows that the surface reveals a wide local distribution of many orientations. The study has been performed at three different electrode potentials, and the histograms look very similar. However, we observed a certain increase in the probability to find flat areas with increasing potential. We attribute the wide distribution of local surface orientations to the presence of different surface reconstructions.

Further, we studied the evolution of the step bunches with time at constant electrode potentials. The study is performed at negative electrode potential (reconstructed surface) and at positive electrode potential (unreconstructed surfaces). In both potential ranges, the orientation of the step bunches is constant in time. Although the orientation of a certain bunch is conserved in time, the individual steps within the bunch are very dynamic. A merging/demerging of steps within the bunch is observed. Therefore, we can conclude that the step bunches are an equilibrium morphology of flame annealed stepped Au(100) electrodes. An evolution in surface morphology with electrode potential is observed, some steep areas tend to flatten with increasing potential.

The surface reconstruction has been studied for Au(1 1 *n*) electrodes in electrolyte. The reconstruction reveals a different unit cell compared to that on nominal flat Au(100) electrodes. The reconstruction periodicity on Au(1 1 *n*) is ~ 1.9 nm compared to ~1.4 nm found on Au(100). The reason for this enlargement seems to be attributed to the stress field originating at the end of the step bunches adjacent to large reconstructed terraces. The wide distribution of local orientations on Au(1 1 *n*) surfaces support the formation of different surface reconstructions. They are similar to the reconstruction on flat Au(100) terraces, however, the distance between the reconstruction stripes varies. The different types of surface reconstructions can explain the complex structure of the voltammograms for Au(1 1 *n*) electrodes.

The second part of this thesis dealt with the study of equilibrium step fluctuations on Au(1 1 17) and Au(1 1 29) in Cl^- -and Br^--containing electrolyte. Time STM images are required to study the time correlation function. The time correlation function $G(t)$ obeys a time power law with a certain exponent α. For both surfaces, a constant offset $G(t=0)$ contributes to the time correlation function. This constant offset seems to depend on the electrode potential. For Au(1 1 17) in Cl^- containing electrolyte and below +400 mV , the correlation function obeys a power law with time exponent α close to 1/2. For Au(1 1 29) in Br^- containing electrolyte and below +50 mV the time exponent is also close to 1/2. For both surfaces a sudden jump in the time exponent α to 3/4 is found at high potentials. Then $G(t)$ depends also on step-step distance L with an exponent close to 3/2. Both the sudden jump in the time exponent to 3/4 and $L^{3/2}$-dependence can be explained with the close proximity of the electrode potential to a phase transition from an unordered halide adlayer to an ordered superstructure.

Furthermore, we studied the spatial correlation function $G(y)$. In this study, normal STM images are required where the time contribution to the STM image can be neglected. The $G(y)$ depends linearly on the distance along the step y. From the linear dependence, the kink energies ε can be determined. The obtained kink energies are in reasonable agreement with data obtained in previous studies. We observed that the kink energies depend linearly on the electrode potential. The kink energies depend also linearly on the surface charge. From the slope the dipole moments of kinks for Au(1 1 17) in Cl^- containing electrolyte and for Au(1 1 29) in Br^- containing electrolyte were determined for the first time: $\mu^{Cl} = (6.02\pm0.7)\text{x}10^{-3}$ eÅ and $\mu^{Br} = (10.08\pm0.6)\text{x}10^{-3}$ eÅ, respectively. The obtained kink dipole moments can be compared only with the calculated step dipole moment that exist in previous studies, due to the fact that there is

no experimental data for the kink dipole moment available. However, the obtained kink dipole moments in this thesis are comparable with data on step dipole moments obtained in previous studies.

As an outlook in collaboration with theoretical groups (W. Schmickler, T. Jacob) we perform currently theoretical calculations on the kink dipole moment. However, there are no results available yet.

In future, it would be interesting to perform similar studies on the structural properties of other metal electrodes such as vicinal Ag(1 1 *n*). Ag reveals no reconstruction in vacuum as well as in electrochemistry. Therefore, the local step-step distance distribution and the local surface evolution might be influenced only by the electrode potential rather than by the reconstruction.

We are currently studying with investigations on islands dynamics in Br^- containing electrolyte. These studies seem to be very promising, since it was demonstrated in this thesis that the ordered bromide adlayer enhances the mobility of Au surfaces dramatically is has not been studied yet with respect to island fluctuations and the corresponding island equilibrium shape.

Last but not least, it seems obviously that electrochemical STM studies of the dynamical properties of metal surfaces have proved to be a powerful method to understand and extract a lot of important information about surface stability and different atomic processes that occur on metal surfaces, which are very useful in future for the understanding of nano-structures of surfaces and, hence, for the development of new nano-technologies.

References

[1] Bohnen, K. P. and K. M. Ho. Surface Science Reports. 19 (**1993**): 99-120

[2] P. Eisenberger and L.C Feldman. Science, Vol. 214, 16 October (**1981)** 300-305

[3] Motonari Adachi and David J. Lockwood. *Self-Organized Nanoscale Materials*. Springer Science+Business Media, Inc. (**2006)**.

[4] *Frontiers in Surface and Interface* Science" edited by C.B Duke and E. W. Plummer (Elsevier Amsterdam, (**2002**), Vol. 500 of the journal Surface Science.

[5] S. Rousset , F. Pourmir , J.M. Berroir , J. Klein , J. Lecoeur , P. Hecquet , B. Salanon. Surface Science. 422 (**1999**) 33–41

[6] E.P.M. Leiva and W. Schmickler .*Theories and Simulations for Electrochemical Nanostructures. Nanostructure Science and Technology*. Springer Science Business Media, LLC (**2009)**

[7] H. Ibach and H. Lüth .*Solid- State physics. An introduction to principles of material science*. Springer (**2003)**

[8] Dietterle, M., PhD thesis, University of Ulm (**1996)**

[9] Klaus Hermann, *http://surfexp.fhi-berlin.mpg.de/SXinput.html*

[10] H. Ibach, *Physics of Surfaces and Interfaces*, Springer, Berlin, Heidelberg, New York, (**2006**)

[11] Ludwig A. Kibler. *preparation and characterization of nobel metal single crystal electrode surfaces*, Department of Electrochemistry**,** University of Ulm, International Society of Electrochemistry (**2003**)

[12] H.-C. Jeong, E.D. Williams. Surface Science Reports. 34 (**1999**) 171-194

[13] Christoph Tegenkamp. Journal of Physic: Condensed Matter. 21 (**2009**) 013002 (18pp)

[14] M. Giesen. Progress in Surface Science. 68 (**2001**) 1-153

[15] J. Lapujoulade, Surface Science Reports. 20 (**1994**) 191

[16] M.Giesen and G. Beltramo .*Dynamic and stability of surface structures*. Chapter 3. *Catalysis in electrochemistry : from fundamentals to strategies for Fuel Cell Development*, First Edition. (**2011**) John wiely & Sons, Inc.

[17] M.moiseeva et. al. Surface Science. 603 (**2009)** 670-675

[18] L.E. Shilkrot, D.J. Srolovitz, Physical Review. B 53 (**1996**) 11120

[19] W. Schmickler. *Interfacial electrochemistry*. New York, Oxford, Oxford University press (**1996**)

[20] Allen J. Bard and Larry R. Faulkner. *Electrochemical methods*, *Fundamentals and Applications.* John Wiley & Sons, Inc. Second Edition (**2001**)

[21] Kolb, D. M.; Schneeweiss, M. A., Bunsin-Magazin 8 (**2006)** 63

[22] D.M. Kolb, Electrochemica Acta. 45 (**2000**) 2387-2402

[23] Japan Nanonet Bulletin-October 26, (**2006)** 82nd Issue

[24] H. Ibach, W. Schmichkler. Physical Review Letters. 91 (**2003**) 016106

[25] A.Y. Lozovoi, A. Alavi. Physical Review Letters. B 68 (**2003**) 245416

[26] G.L. Beltramo et al. Surface Science. 601 (**2007**) 1876-1885

[27] A. Hamelin, L. Stoicoveciu, L. Doubova, S. Trasatti. Surface Science. 201 (**1988**) L498

[28] H. Ibach, M. Giesen, W. Schmickler. Journal of Electroanalytical Chemistry. 544 (**2003**) 13-23

[29] H. Ibach, W. Schmickler. Surface Science. 573 (**2004**) 24-31

[30] T. L. Einstein and S. V. Khare. *Dynamic of crystal surfaces and interfaces*, Edited by Duxbury and Pence, Plenum Press, New York, (**1997)**

[31] E. Ising. Zeitschrift für Physik. 31 (**1925**) 253

[32] W. W. Mullins, Journal of Applied Physics. 30 (**1959**) 77

[33] W. W. Mullins. Journal of Applied Physics. 28 (**1957**) 333
[34] W. W. Mullins, in N.A. Gjostein, R. W. Roberts. *Metal Surafces: Structure, Energetics and Kinetics*, American Society of Metals, Metals Park, Ohio, (**1963**)
[35] N.C. Bartelt, T.L. Einstein and E.D. Williams. Surface Science. 240 (**1990**) L591
[36] M. Poensgen et al. Surface Science. 274 (**1992**) 430-440
[37] M. Giesen et al. Surface Science. 366 (**1996**) 229-238
[38] M. Giesen, D.M. Kolb, Surface Science. 468 (**2000**) 149-164
[39] N. C. Bartelt, J.L. Goldberg, T.L. Einstein, E. D. Williams. Surface Science. 273 (**1992**) 252
[40] M.Giesen-Seibert, F. Schmitz, R. Jentjens, H. Ibach. Surface Science. 329 (**1995**) 47
[41] M. Giesen et al. Surface science. 384 (**1997**) 168-178
[42] G. Ehrlich, F.g. Hudda. Journal of Chemical Physics. 44 (**1966**) 1039
[43] R.L. Schwoebel, E.J. Shipsey. Journal of Applied Physics. 37 (**1966**) 3682
[44] M. Giesen, S. Baier. Journal of Physics: Condensed Matter. 13 (**2001**) 5009-5026
[45] M. Giesen et al. Electrochimicia Acta. 45 (**1999**) 527-536
[46] M. Alshakran et. al. Surface Science. 605 (**2011**) 232-239
[47] G. Binning and D. P. E. Smith. Review of Scientific Instruments. 57 (**1986**) 1688
[48] G. Binning, H. Rohrer, Ch. Gerber, and E. Weibel. Physical Review Letters. 49 (**1982**) 57-60.
[49] Jennifer E. Hoffman, PhD thesis. University of California, Berkeley (**2003**)
[50] J. Halbritter, G. Repphung, S. Vinzelberg, G. Staikov, and W. J. Lorentz. Electrochemica Acta, Vol. 40, No. 10, app. (**1995**) 1385-1394
[51] E. Abelev, N. Sezin, and Y. Ein-Eli. Review of Scientific Instruments. 76 (**2005**) 106105
[52] Ellen D. Williams. Surface Science. 299/300 (**1994**) 502-524
[53] H. Minoda *et al.* Physical Review B. 61. (**2000**) 5672-5678
[54] K Sudoh and H Iwasaki. Journal of Physics: Condensed Matter 15(**2003**) S3241-S3253
[55] Hroo Omi, Yoshikazu Homma, Vesselin Tonchev, Alberto Pimpinelli. Physical Review Letters. PRL 95 (**2005**) 216101
[56] S. Stoyanov and V. Tonchev. Physical Review B 58 (**1998**) 1590-1600
[57] Masahide Sato, Makio Uwaha. Surface Science 493 (**2001**) 494-498
[58] J. Chang, O. Pierre-Louis, and C. Miesbach. Physical Review Letters. PRL 96, (**2006**) 195901
[59] A. Pimpinelli, V. Tonchev, A. Videcoq, and M. Vladimirova. Physical Review Letters. 88 (**2002**) 206103
[60] S. Baier, H. Ibach, M.Giesen. Surface Science. 573 (**2004**) 17-23
[61] G. M. Watson et.al. Surface Science. 407 (**1998**) 59-72
[62] M. Sotto, J. C Boulliard. Surface Science. 214 (**1989**) 97-110
[63] M. Kardar. Turkish Journal of Physics. 18 (**1994**) 221
[64] S. V. Khare. T. L. Einstein, Physical Review B. 57 (**1998**) 4782.
[65] B. Blagojevic. P. M. Duxbury, Physical Review B. 60 (**1999**) 1279.
[66] O.K. Binning, H. Rohrer, C. Gerber, E. Stoll. Surface Science. 144 (**1984**) 321
[67] S.G.J. Mochrie, D.M. Zehner, B.M. Ocko, D. Gibbs. Physical Review Letters. 64 (**1990**)2925
[68] B.M. Ocko, D. Gibbs, K.G. Huang, D.M. Zehner, S.G.J. Mochrie. Physical Review B. 44 (**1991**) 6429 LP.
[69] M.A. Van Hove, R.J. Koestner, P.C. Stair, J.P. Biberian, L.L. Kesmodel, I. Bartos, G.A. Somorjai. Surface Science. 103 (**1981**)189.
[70] D.M. Kolb, G. Lehmpfuhl. M.S. Zei. Journal of Electroanalytical Chemistry. 179 (**1984**) 289
[71] D.M. Kolb. Progress in Surface Science. 51 (**1996**) 109
[72] X. Gao, A. Hamelin, M.J. Weaver. Physical Review Letters. 67 (**1991**) 618
[73] Ch. Bombis, H. Ibach. Surface Science. 564 (**2004**) 201.
[74] P. Skoluda, D.M. Kolb. Surface Science. 260 (**1992**) 229
[75] A. Bartolini, F. Ercolessi, E. Tosati. Physical Review Letters. 63 (**1989**) 872.
[76] E. Santos, W. Schmickler. Chemical Physics Letters. 400 (**2004**) 26.
[77] Y.J. Feng, K.P. Bohnen, C.T. Chan. Physical Review B. 72 (**2005**) 125401.

[78] A. Cuesta, D.M. Kolb. Surface Science 465 (**2000**) 310-316
[79] S.-L. Yau, C.M. Vitus, B.C. Schardt. Journal of American Chemistry.112 (**1990**) 3677

[80] M. Kruft, B. Wohlman, C. Stuhlman, K. Wandelt. Surface Science. (**1997**) 601-604
[81] P. Broekmann et al. Journal of Electroanalytical Chemistry 500 (**2001**) 241-254
[82] M. Giesen et al. Surface Science. 366 (**1996**) 229-238
[83] Pichardo-Pedrero et al. Applied Physics A. 87 (**2007**) 461-467
[84] M .Giesen, G.S. Icking- Konert. Surface Science. 645 (**1998**) 412-413
[85] L. Kuipers, M.S. Hoogeman, J.W.M. Frenken. Physical Review Letters. 71 (**1993**) 3517
[86] W.W. Pai, N.C Bartelt, J.E. Reutt-Robey. Physical Review B. 53 (**1996**) 15991
[87] P. Broekmann, M. Wilms, M. Kruft, C. Stuhlmann and K. Wandelt. Journal of Electroanalytical Chemisty. 467 (**1999**) 307
[88] S. Baier, S. Dieluweit and M. Giesen. Surface Science. 502-503 (**2002**) 463
[89] M. Giesen, M. Dietterle, D. Stapel, H. Ibach and D.M. Kolb. Surface Science. 384 (**1997**) 168-178
[90] I. Vattulainen, J. Merikoski,T. Ala-Nissila, and S. C. Ying. Physical Review Letters. V.79, No.2. (**1997**) 257-260
[91] X. Zhang, D. Dabiri, and M. Gharib. Review of Scientific Instruments. Vol. 67, No. 5, May (**1996**) 1858-1868
[92] U. Tartaglino, E. Tosati, D. Passerone, F. Ercolessi. Physical Review B. 65 (**2002**) 241406.
[93] G.L. Beltramo et al. Surface Science. 601 (**2007**) 1876–1885
[94] M. Giesen. Private communication
[95] E. Pichardo-Pedrero, M. Giesen. Electrochimica Acta. 52 (**2007**) 5659-5668
[96] M. Giesen et al. Surface Science. 595 (**2005**) 127-137
[97] A. Pimpinelli, J. Villian, D.E. Wolf, J.J. Metois, J.C. Heyraud, I. Elkinari, G. Uimin. Surface Science. 295 (**1993**) 143
[98] M. Giesen-Seibert, R. Jentjens, M. Poensgen and H. Ibach. Physical Review Letters. 71 (**1993**) 3521.
[99] M. Giesen-Seibert and H. Ibach. Surface Science. 316 (**1994**) 205.
[100] M. Giesen, C. Steimer and H. Ibach. Surface Science. 471 (**2001**) 80.
[101] S. Dieluweit, M. Giesen. Journal of Electroanalytical Chemistry 524–525 (**2002**) 194–200
[102] Sabine Dieluweit, Harald Ibach and Margret Giesen. Faraday Discuss. 121 (**2002**) 27–42
[103] A. Biedermann et al. Physical Review Letters. Vol. 76. No.22. May (**1996**) 4179-4182
[104] L.D. Landau and E.M. Lifschitz, *Lehrbuch der Theoretischen Physik* , Band S "Statistische Physik". Akademie, Berlin (1980).

Acknowledgments

First of all, I would like to say so much thanks to my Doctor advisor *Mrs. Dr. Margret Giesen,* who gave me the opportunity to do my PhD thesis in her group. I thank her for the great guidance and powerful talent explaining me the surface science principles. I have learned a lot of things from her. I would also like to thank her for spending a lot of time explaining me the atomic diffusion processes at surfaces, her kind encouragement(*don't worry, be happy ☺…*), valuable help, and exciting ideas during my hard time working in the institute. I remember how much I was happy when she surprised me with a very kind gift on the occasion of my daughter Alma´s birth and sharing with us any special events (*I enjoyed so much when she played Guitar last Christmas 2010…*). I appreciate her so much.

I would also like to thank *Prof. Dr. Harald Ibach* for his kind support and helpful discussion during my thesis work. He spent a lot of time explaining to me the program code for analyzing the correlation function. His brilliant ideas and exciting discussions were very precious for me. I had a very fruitful collaboration with him. I am very proud to have worked with him.

I am especially grateful to *Prof. Dr. Klaus Shierbaum* for his support and helpful discussion during my thesis work. Also I would like to thank *Prof. Dr. Rudolf Merkel* for giving me the opportunity to work in his institute. Many thanks also to our collaborators *Prof. Dr. W. Schmickler* and *Dr. T. Jacob*.

Many thanks to *Dr. Guillermo Beltramo*, my kind friend I ever seen. I would like to thank him for all his scientific support during my thesis. All the high quality voltammograms have been done by him. I was so pleased to share with him the same office. I also want to thank him for the useful and kind discussions we had together in the office. Many thanks also for his kind family, *Carina*, *Larisa* and *Augistin*.

I am much obliged to *Mr. Udo Linke* for the excellently prepared Au crystal and for his valuable technical advice. I would like to thank *Prof. Joachim Krüg* for his interest in my thesis work and for his helpful discussion.

It has been a tragedy when we lost one of the most kind and helpful worker in our group, *Mr. Karl Hieble*, his death was a strong shock for us. I would like to thank him for all his experimental advices.

Special gratitude also to our kind secretary *Mrs. Claudia Klamandt*, and for our great foreigner advisor *Mrs. R. Bley* for her nice support. Many thanks also to my friend *Mrs. Claudia Steufmehl*. For all members in ICS-7 I say thank you.

Last but not least special gratitude to my lovely wife *Eman* who stood by me all the time and supported me when I needed it. My little lovely daughter *Alma*, is also gratituted for her patience (*when I was absence from home ☺)*. Many thanks to my great parents for creating an academic atmosphere and continuous encouragement during my study in Germany.

aus dem Institut für
der Heinrich-Heine Universität Düsseldorf

Gedruckt mit der Genehmigung der
Mathematisch-Naturwissenschaftlichen Fakultät der
Heinrich-Heine-Universität Düsseldorf

Referent: Prof. Dr. Klaus Schierbaum
Koreferent: Priv. Doz. Dr. Margret Giesen

Tag der mündlichen Prüfung:

23.05.2011